NON-DESTRUCTIVELY MAPPING THE IN-SITU HYDROLOGIC PROPERTIES OF SNOW, FIRN, AND GLACIAL ICE WITH GEORADAR

by

Joel Matthew Brown

A dissertation
submitted in partial fulfillment
of the requirements for the degree of
Doctor of Philosophy in Geophysics
Boise State University

May 2012

BOISE STATE UNIVERSITY GRADUATE COLLEGE

DEFENSE COMMITTEE AND FINAL READING APPROVALS

of the dissertation submitted by

Joel Matthew Brown

Dissertation Title: Non-Destructively Mapping the In-Situ Hydrologic Properties of Snow, Firn, and Glacial Ice with Georadar

Date of Final Oral Examination: 18 January 2012

The following individuals read and discussed the dissertation submitted by student Joel Matthew Brown, and they evaluated his presentation and response to questions during the final oral examination. They found that the student passed the final oral examination.

John Bradford, Ph.D.	Chair, Supervisory Committee
Hans-Peter Marshall, Ph.D.	Member, Supervisory Committee
James McNamara, Ph.D.	Member, Supervisory Committee
Joel Harper, Ph.D.	Member, Supervisory Committee
Colin Zelt, Ph.D.	External Examiner

The final reading approval of the dissertation was granted by John Bradford, Ph.D., Chair of the Supervisory Committee. The dissertation was approved for the Graduate College by John R. Pelton, Ph.D., Dean of the Graduate College.

DEDICATION

I dedicate this dissertation to my wife, Leah Versteegen.

Leah and I were married in the summer of 2005. Two years later, I had the opportunity to conduct research on the Greenland Ice Sheet. Five weeks in the field ending 3 weeks before the expected arrival of our son Odin. I cannot overstate the bravery she showed during those 5 weeks. However, it was nothing compared to the bravery and patience she showed the next summer when I left for another field season on the Ice Sheet, leaving her to take care of our 7 month old baby by herself. I am in awe of the support and understanding that was graciously and enthusiastically given to me by Leah. During my tenure as a doctoral student she accepted the time commitment needed in this undertaking with full understanding. My two field seasons were certainly trying on her but so were the long days and late nights working on my research.

Thank you, Leah, for all you are and for all you give to me.

AUTOBIOGRAPHICAL SKETCH OF AUTHOR

Education:

M.S., Geology, University of Montana, 2006; Thesis: “Spatiotemporal variations of englacial scattering of radar within Bench Glacier, a temperate glacier in coastal Alaska.”

B.A., Physics/Astronomy, University of Montana, 2003

Peer reviewed publications:

Brown, J., J. Bradford, J. Harper, W. T. Pfeffer, N. Humphrey, and E. Mosley-Thompson (2012), Georadar-derived estimates of firn density in the percolation zone, western Greenland Ice Sheet, *Journal of Geophysical Research*, *117*, F01011, doi:10.1029/2011JF002089.

Brown, J., J. Harper, W.T. Pfeffer, N. Humphrey, and J. Bradford (2011), High resolution study of layering within the percolation and soaked facies of the Greenland Ice Sheet, *Annals of Glaciology*, *52*(59).

Brown, J.M., Harper, J.T., and Humphrey, N. (2010), Cirque Glacier Sensitivity to 21st Century Warming: Sperry Glacier, Rocky Mountains, U.S.A., *Global planetary Change*, *74*, 91-98, doi:10.1016/j.gloplacha.2010.09.001.

Bradford, J. H., J. T. Harper, and **J. Brown** (2009), Complex dielectric permittivity measurements from ground-penetrating radar data to estimate snow liquid water content in the pendular regime, *Water Resour. Res.*, *45*, W08403, doi:10.1029/2008WR007341.

Brown, J.M., Harper, J.T., and Bradford, J.H. (2009), A radar transparent layer in a temperate valley glacier: Bench Glacier, Alaska. *Earth Surface Processes and Landforms*, *34*(11), 1497-1506.

Brown, J., J. Nichols, L. Steinbronn, J. Bradford (2009), Improved GPR interpretation through resolution of lateral velocity heterogeneity: example from an archaeological site investigation, *Journal of Applied Geophysics*, *68*, 3–8.

ACKNOWLEDGEMENTS

It is a gross understatement to say that I would have not been able to complete this dissertation or the research it details without the help of many people and organizations.

Any perceived understandings of geophysical principles that may be in this dissertation are a direct result of tutelage I received from my advisor, Dr. John Bradford. In many ways, I am not an ideal student as I am sure I demonstrated to John on numerous occasions. I am lucky to have had an advisor with such an understanding of geophysics, the patience to deal with a student as difficult as myself, and the understanding that graduate school was only one part of my life, and not always my highest priority. Thank you, John, for the opportunity to work with you on what I think are very interesting topics.

I am greatly indebted to Dr. Joel Harper whom has guided me in the study of snow and glaciers and has frequently employed me in the study of the cryosphere. Without your help and guidance I would certainly not have produced the papers that make up this dissertation. Thank you, Joel, for making me a better scientist as well as for all of the guidance in writing and preparing the manuscripts published herein.

I would also like to thank Dr. Neil Humphrey and Dr. W. Tad Pfeffer for their help and guidance in Greenland. Thank you to Dr. Ellen Mosley-Thompson for taking the time to be a part of one of the papers that makes up this dissertation. My gratitude goes to

Dr. Hans-Peter Marshall, Dr. Jim McNamara, and Dr. Colin Zelt for taking the time to read this dissertation and be on my committee. I would not have been able to work without the financial support from fellowships through the Inland Northwest Research Alliance and the Boise State Geosciences department.

The second chapter of this dissertation was reprinted from the *Annals of Glaciology* with permission of the International Glaciological Society. The third chapter of this dissertation was originally published in *Journal of Geophysical Research, Earth Surface*; it has been reproduced/modified by permission of American Geophysical Union. The fifth paper in this dissertation was reprinted from *Global and Planetary Change* with permission from Elsevier. Thank you.

Lastly, I would like to thank my family; my parents for all of their support, for teaching me the value of a solid work ethic, and for instilling a healthy amount of curiosity in me; my brother and sisters for feigning interest in my studies and making me leave my work at work; my children for making this experience more interesting; and my wife for all of the reasons described in the dedication. Thank you.

ABSTRACT

Ground penetrating radar (GPR) is a useful tool for studying the in-situ properties of glacial ice, firn, and snowpacks. The main focus of this dissertation is improving and expanding methods employed when collecting, processing, and understanding GPR data collected in the Cryosphere, or the snow and ice covered areas of the earth. The data used herein were collected on the Greenland Ice Sheet (GrIS) and on seasonal snowpacks of Western Montana, USA. This document has three sub-topics.

The first sub-topic is comparing the spatial variability of GPR data to the spatial variability of core data collected in two locations within the percolation zone of the GrIS that receive consistently different amounts of melt. At the location with less melt, I collected common offset GPR data over a 20 m x 20 m grid with tightly spaced data (0.2 m x 0.1 m), and then collected 8 cores within the grid. The cores reveal a high degree of spatial variability over short distances with no obvious correlation of layers between cores whereas the radar data reveal many spatially continuous horizons with discontinuities from 0.1 m^2 – 1.0 m^2. At the site with a higher melt rate, I collected common offset GPR data over a 15 m x 50 m grid with tightly spaced data (0.2 m x 0.1 m), and then collected 2 cores within the grid. The cores revealed some degree of lateral continuity of layers that corresponded well with spatially continuous GPR horizons.

The second sub-topic of this dissertation is using Common Midpoint (CMP) GPR data to calculate the density vs. depth profiles at 13 locations within the percolation zone of the GrIS. Here, I constructed a set of rules to constrain an inversion of the data to solve for the EM propagation velocity of the firn column which is dependent on the density of dry snow and firn. The calculated density profiles indicate that firn densification is not greatly affected by melt in the highest elevation areas of the percolation zone whereas firn densification is primarily driven by melt/refreeze processes in the lower elevation areas of the percolation zone. The transition zone between these areas with different primary drivers of densification is 8 km wide and spans 60 m of elevation suggesting that the balance between dry firn densification processes and melt induced densification processes is sensitive to minor changes in melt, and therefore minor changes in annual temperature.

The final sub-topic is using common offset GPR data to calculate the dielectric permittivity structure of 3 snowpacks with varying depths and internal structure. Here, common offset GPR data is deconvolved using a waveform constructed from a reflection off of a ‘perfectly’ reflecting surface. The calculated deconvolution solution follows the dielectric profile measured in snowpits at 5 locations along the 3 profiles. The technique used here has the potential to map the depth and density of snow over large regions, resulting in more accurate estimates of total snowpack in mountainous terrain, and is important for constraining retrievals from airborne and space-borne microwave radar.

TABLE OF CONTENTS

LIST OF TABLES

LIST OF FIGURES

CHAPTER ONE: INTRODUCTION

1.1 Motivation and Research Objectives

The use of ground penetrating radar (GPR) in snow and ice has evolved from simple radio-echo sounding of glaciers and ice sheets [e.g., *Robin et al*., 1969] to determine depth of ice, to 3D multi-fold data sets revealing englacial fractures in small mountain glaciers [e.g., *Harper et al*., 2010]. Although this evolution has led to a greater understanding of the cryosphere, there exists significant room to improve data acquisition techniques, data processing methods, and an overall understanding of the limits of interpretation of GPR in the cryosphere. Thus, the motivation behind the work included in this dissertation is to progress the use of GPR as an instrument of measurement in the Cryosphere and to use these improved methods to elucidate the variable affects that melt and compaction have on the internal structure and hydrology of firn and seasonal snowpacks over large spatial areas. This work involved geophysical investigation and interpretation of data, as well as glaciological interpretation of the data. To this end, I collected near-surface georadar data in the percolation area of the Greenland Ice Sheet as well as in mountainous snowpacks of Western Montana.

1.2 The Greenland Ice Sheet

In the dry snow facies of the Greenland Ice Sheet (GrIS) as in Antarctica, radar derived internal reflecting horizons in the firn are primarily associated with density contrasts across yearly summer surfaces where high-density, wind-scoured surfaces overly a layer of faceted grains [*e.g.*, *Arcone et al.*, 2004]. Density variations that are present in the surface layer are preserved in deeper layers because overburden drives densification through the entire annual layer. Internal reflection horizons in firn are generally accepted to be isochrones [*e.g.*, *Vaughan et al.*, 1999; *Helm et al.*, 2007]. In regions where surface melt occurs, however, the processes of infiltration and refreezing heterogeneously changes the internal density structure of the firn column. These changes in the intra-layer density structure affect the internal reflections recorded with georadar and also affect the isochronal nature of layering in the firn column.

The percolation facies "is subjected to localized percolation of melt water from the surface without becoming wet throughout" and the soaked facies "becomes wet throughout during the melting season" [*Benson*, 1960]. These two facies span the area between the dry snow line and the firn line. Thus, both the percolation and soaked facies of the GrIS are regions with net positive annual accumulation and some amount of surface melt. The percolation facies covers more than 1/3 of the total area of the GrIS [*Nghiem et al.*, 2005], the soaked facies is less extensive, covering less than 10% of the area of the percolation facies [estimated from Figure 48, *Benson*, 1960]. Because of yearly variations in total accumulation and extent of melt, the size and distribution of both the percolation and soaked facies are annually transient. The percolation and soaked facies, however, always represent a substantial area of the ice sheet. Throughout most of the year, there is no surface expression for the boundary between the percolation facies and the soaked facies, thus we refer to both facies together as the 'percolation zone.' In the percolation zone of the GrIS, infiltration of surface melt affects how seasonal snow layers transform into ice, therefore, the thickness, densification rate, and densification processes of the firn column differ from the rest of the accumulation area (the dry facies).

Past studies of the percolation zone show that meltwater is generated at the surface, infiltrates into the snow layer, and refreezes. This process forms ice layers, ice lenses, and ice pipes [e.g., *Benson*, 1960; *Pfeffer et al.*, 1991]. Georadar surveys within the percolation zone reveal a layered, uneven subsurface with laterally continuous high reflectivity layers that are often interpreted as previous summer surfaces [e.g., *Dunse et al., 2008*; *Legarsky and Gao*, 2006]. Detailed snow-pit surveys of the upper few meters of firn within the percolation zone [e.g., *Benson*, 1960; *Fischer et al.*, 1995; *Parry et al.*, 2007; *Dunse et al.*, 2008] reveal firn layers separated by seasonal high-density boundaries. Within this layered structure there are ice lenses and ice pipes that form when infiltrating water refreezes in the cold firn. Shallow cores also reveal a layered subsurface with ice pipes and ice lenses [*Parry et al.*, 2007]. All of these observation techniques show increased meltwater retention with a decrease in elevation until complete saturation of the surface layer is eventually reached [*Braithwaite et al.*, 1994].

Firn cores spanning the full depth of the firn column from the annual snow layer to the theoretical pore close-off density of ~830 kg/m^3 [*Paterson*, 2002] have been collected in the upper regions of the percolation facies [e.g., *Mosley-Thompson et al.*, 2001]. These cores are used to calculate accumulation rates, to measure density vs. depth relationships ($d\rho/dz$), and to calculate densification rates ($d\rho/dt$). The ability to determine accumulation and densification rates is dependent on the ability to identify an annual signal in the core. This is difficult in regions with melt that have more vertical dispersion of possible seasonal indicators (dust, δ^{18}O, δD, etc.) within the seasonally accumulated layer [*Hou and Qin*, 2002] than in regions of no melt. Because the quality of the information preserved in cores that are acquired in the percolation zone is limited, the cores that have been drilled in that region are often short and usually in the upper elevations of the percolation zone where the effects of melt infiltration are limited. Thus, the effect of increased surface melt on firn densification through the entire firn column is largely unknown. This is especially true at lower elevations of the percolation zone.

Chapter Two of this dissertation is a manuscript published in *Annals of Glaciology* [*Brown et al.*, 2011] wherein I compared horizons identified in gridded georadar data to cores at two locations within the percolation zone of the GrIS. Chapter Three is a manuscript submitted to *Journal of Geophysical Research – Earth Surface* [*Brown et al.*, 2012] wherein I calculate the depth vs. density profile of the firn column at 13 locations along a transect that spans much of the percolation zone from areas with less than an average of 13 days of melt per year to areas with an average of 53 melt days per year [*Abdalati*, 2007]. These chapters contribute to an understanding of the complexities of the firn structure in the percolation zone. I developed a method to invert for the depth vs. density profile of the firn column. This method employs a consistent set of rules to constrain the inversion of common midpoint GPR data for the electromagnetic velocity structure of the firn column. This method can be used to calculate the density profile of the firn column without coring. I use this method to calculate the firn density profile at 13 locations within the percolation zone spanning ~600 m of elevation. The calculated density profiles indicate that firn densification is not greatly affected by melt in the highest elevation areas of the percolation zone. However, firn densification is primarily driven by melt/refreeze processes at the lower elevation areas of the percolation zone. The transition zone between these areas is 8 km wide and spans 60 m of elevation suggesting that the balance between dry firn densification processes and melt induced densification processes is sensitive to minor changes in melt. The melt/refreeze processes also greatly affect formation of laterally consistent ice layers within the firn, this includes initially forming and increasing the size of ice layers. In Chapter Two, comparisons between gridded radar data and firn cores at two sites separated by ~320 m of elevation reveal a large disparity in potential sources of GPR reflection horizons. This result has implications for tying GPR data to cores in the attempt to interpolate the age/depth structure of the firn column between cores.

1.3 Seasonal Snowpack in the Western United States

In the Western United States, most of the water available for irrigation and power generation during the summer months precipitates as snow during the winter months [*Serreze et al.*, 1999]. As the population of the West increases, it becomes more important that predictions of water storage based on snow water equivalent (SWE) are more accurate. More than 1/6th of the global population, or over 1 billion people worldwide depend on seasonal snow for water, and 50-80% of the water supply in the West comes from seasonal snow. Current predictions of summer water levels are based on point source SWE measurements obtained either remotely from SNOTEL (SNOwpack TELemetry) sites, or manually at snow course locations. These point measurements of SWE are used to predict stream flow based on statistical regressions of past comparisons of these point measurements to stream flow. Due to the large variability of snowpack depth and density, the point measurements of SWE may not be representative of SWE over larger, watershed scales [*Bales et al.*, 2009].

Ground penetrating radar has been used to measure the inherent spatial variability of snow in mountainous terrain [*e.g.*, *Lundberg et al.*, 2000], on glacier surfaces [e.g., *Machguth et al.*, 2006], and on ice sheets [e.g., *Dunse et al.,* 2008]. In most of these studies, reflection horizons apparent in GPR images are correlated with surfaces either within the snowpack, at the snow/ground interface, or at the snow/firn boundary. These correlations between two-way traveltime and depth are often based on point measurements of GPR signal propagation velocity with depth, physical depth measurements, or both. The extrapolation of the depth or velocity measurements away from the measurement points leads to spurious results in regions with lateral variation in snow density or wetness. Measuring lateral variations in snowpack properties is possible through multiple physical measurements (i.e., multiple snow pit or depth measurements) or multifold GPR surveys. However, multiple radar or physical measurements over the same line are less efficient than a single common offset radar profile. Chapter Four of this dissertation is a manuscript wherein I use a wavelet constructed from GPR measurements collected with antenna suspended 0.7 m above a metal plate, which approximates a ‘perfect’ reflector to deconvolve data collected the same height above the snow surface to solve for the dielectric permittivity of 3 seasonal snowpacks in western Montana. This technique can be used to map the depth/density variations over large areas where terrain creates large variations in snow density and depth with single offset GPR.

1.4 Sperry Glacier, Glacier National Park, MT

The appendix is a paper I published in *Global and Planetary Change* titled "*Cirque glacier sensitivity to 21*st *century warming: Sperry Glacier, Rocky Mountains, U.S.A.*" This paper is the product of a glacier modeling project wherein I employed a modified simple 3-D glacier flow model to investigate the sensitivity of a small mountain glacier to rising average temperatures. By analyzing the resultant outputs for 11 different theoretical warming scenarios, I concluded that the sensitivity to small changes in climate is dependent on the total change that occurs. This work highlights the importance of flow and local terrain in the mass balance of Sperry glacier. The implications of this work include quantifying the unlikeliness of total glacial collapse in Glacier National Park within the commonly projected timeframe of 20-30 years. This work was the culmination of a breadth project that was completed as part of my PhD studies.

CHAPTER TWO: HIGH RESOLUTION STUDY OF LAYERING WITHIN THE PERCOLATION AND SOAKED FACIES OF THE GREENLAND ICE SHEET*

This chapter is published by the International Glaciological Society in *Annals of Glaciology* and should be referenced appropriately.

Reference:

Brown, J., J. Harper, W.T. Pfeffer, N. Humphrey, and J. Bradford (2011), High resolution study of layering within the percolation and soaked facies of the Greenland Ice Sheet, *Annals of Glaciology*, *52*(59).

Reproduced/modified by permission of International Glaciological Society.

*This chapter includes modifications from the originally published version.

High Resolution Study of Layering within the Percolation and Soaked Facies of the Greenland Ice Sheet

Joel Brown [a,b]

Joel Harper [a]

W. Tad Pfeffer [c]

Neil Humphrey [d]

John Bradford [b]

[a] *Department of Geosciences, University of Montana, 32 Campus Dr., Missoula, MT 59812, USA*

[b] *Center for Geophysical Investigation of the Shallow Subsurface, Boise State University, 1910 University Dr., Boise, ID 83725, USA*

[c] *Institute of Arctic and Alpine Research and Department of Geological Sciences, University of Colorado, Boulder, CO 80303-0450, US.A.*

[d] *Geology and Geophysics Dept. 3006, University of Wyoming, Laramie, Wyoming 82071, USA*

Published in:

Annals of Glaciology 52(59) 2011

Abstract

Within the percolation and soaked facies of the Greenland Ice Sheet, the relationship between radar derived internal reflection horizons and the layered structure of the firn column is unclear. We conducted two small-scale ground penetrating radar surveys in conjunction with 10 m firn cores that we collected within the percolation and soaked facies of the Greenland Ice Sheet. The two surveys were separated by a distance of ~50 km and ~340 m of elevation leading to ~40 days difference in the duration of average annual melt. At the higher site (~1997 m a.s.l.), which receives less melt, we found that internal reflection horizons identified in ground penetrating radar data were largely laterally continuous over the grid; however, stratigraphic layers identified in cores could not be traced between cores over any distance from 1.5 m to 14 m. Thus, we found no correlation between directly observed firn core stratigraphy and radar-derived internal reflection horizons. At the lower site (~1660 m a.s.l.), which receives more melt, we found massive ice layers greater than 0.5 m thick and stratigraphic boundaries that span more than 15 m horizontally. Some ice layers and stratigraphic boundaries correlate well with internal reflection horizons that are laterally continuous over the area of the radar grid. Internal reflection horizons identified at ~1997 m a.s.l. are likely annual isochrones but the reflection horizons identified at ~1660 m a.s.l. are likely multi-annual features. Because 1) there is no stratigraphic correlation between firn cores at the 1997 m location and 2) the reflection horizons at the 1660 m location are multi-annual features, we find that mapping accumulation rates over long distances by tying core stratigraphy to radar horizons in the percolation zone may lead to ambiguous results.

2.1 Introduction

In the dry snow facies of the Greenland Ice Sheet (GrIS), radar derived internal reflecting horizons in the firn are primarily associated with density contrasts across yearly summer surfaces where high-density, wind-scoured surfaces overlay a layer of faceted grains [*e.g.*, *Arcone et al.*, 2004]. The dry snow facies of the GrIS is the region above the dry snow line where melt is negligible [*Benson*, 1960]. Because melt is negligible and overburden is the primary driver of densification through the firn column in the dry snow facies, density variations that are present in the annually accumulated snow surface layer are preserved in the firn column. Internal reflection horizons imaged with Ground Penetrating Radar (GPR) in firn are generally accepted to be isochrones [e.g., *Vaughan et al.*, 1999; *Helm et al.*, 2007]. The apparent depth to these reflection horizons has been successfully used to map variations in accumulation rates between firn cores in Antarctica [e.g., *Spikes et al.*, 2004; *Arcone et al.*, 2004]. In regions where surface melt is not negligible, however, the processes of infiltration and refreezing heterogeneously changes the internal density structure of the firn column. These changes in the intra-layer density structure affect the internal reflections recorded with GPR and may also affect the isochronal nature of layering in the firn column.

Within the accumulation zone of the GrIS, the percolation facies (by definition) covers all areas where melt occurs, yet the wetting front does not reach the previous summer surface [*Benson*, 1960]. Regions of the accumulation area where wetting fronts do reach the previous summer surface, thus soaking the seasonal snow layer, are within the soaked facies. The percolation facies covers more than 1/3 of the total area of the

GrIS [*Nghiem et al.*, 2005], the soaked facies is less extensive, covering less than 10% of the area of the percolation facies [estimated from Figure 48, *Benson*, 1960]. Both facies are annually transient; the boundary between them is also transient and has no explicit surface expression, thus we do not distinguish between them herein, instead, we use the term ‘percolation zone’ to encompass both facies. Within the percolation zone, infiltration of surface melt redistributes mass vertically and horizontally. The result of this redistribution of mass varies with the amount of melt, the cold content of the firn, and the accumulation rate at the location.

Past studies have shown that at ~1940 m elevation upstream of Jakobshavn in the percolation zone of western Greenland (Figure 1), summer melt greatly modifies the surface snow layer [*Pfeffer and Humphrey*, 1998; *Scott et al.*, 2006a; *Parry et al.*, 2007]. In early spring, before the onset of melt, dry, low density snow with small density variations (due to buried wind scoured surfaces) overlies a heterogeneous layer of firn with ice pipes and ice layers [*Dunse et al.*, 2008; *Parry et al.*, 2007; *Scott et al.*, 2008a,b; *Helm et al.*, 2007]. At the end of the summer melt season, the snow layer is more complex with ice pipes and ice layers distributed non-uniformly [*Jezek et al.*, 1994; *Pfeffer and Humphrey,* 1998; *Parry et al.,* 2007]. At lower elevations (~1800 m to ~1450 m), water from increased melting saturates yearly accumulated snow, penetrates the previous summer surface, and reaches depths of 2 m – 4 m [*Braithwaite et al.*, 1994; *Pfeffer and Humphrey,* 1998].

Because percolation of surface melt can change the physical characteristics of annual layering and internal reflection horizons in many different ways through the percolation zone, studies combining GPR data and layer stratigraphy in the percolation zone yield a wide range of results. Along a short 5 m profile recorded to ~10 m depth at ~1940 m elevation, *Scott et al.* [2006a] did not resolve any continuous internal reflection horizons. However, on a longer profile (1500 m), they found a semi-continuous reflection horizon at ~2 m depth. It is likely that laterally continuous reflection horizons were missed in the 5 m profile because they used 0.5 m to 1.5 m trace spacing with 13 GHz radar, where the Nyquist sampling distance is less than 0.01 m for this frequency [*Nyquist*, 1928; *Dunse et al.*, 2008]. In the 1500 m survey, the horizon was likely identified because a 5 trace running mean was applied to the data during acquisition, effectively increasing the footprint of each recorded trace. In a later survey, *Scott et al.* [2006b] interpreted high levels of radar backscatter as previous summer surfaces; between ~2350 m and ~1940 m elevation the number of identifiable backscatter peaks diminished from 5 annual layers to a single reflection representing the last summer surface. Also at ~1940 m, *Dunse et al.* [2008] used GPR to identify 6 internal reflection horizons within the upper 10 m of firn. It is likely that *Dunse et al.* [2008] were able to identify more layers at ~1940 m elevation because they used lower frequency radar (500 MHz) than the 2-18 GHz radar used by *Scott et al.* [2006b]. *Dunse et al.* [2008] correlated the reflection horizons to ice layers or previous summer surfaces identified in firn cores by *Scott et al.* [2006b] and *Parry et al.* [2007]. Further, they interpreted summer melt conditions that potentially result in each identified layer. However, because melt induced diagenic features in the percolation zone of the GrIS are rarely laterally continuous even over short distances [*Parry et al.*, 2007], it is unclear if internal reflection horizons can be correlated to stratigraphic layers or sequences of stratigraphic layers identified in firn cores. Further, it is unclear where (or if) internal reflection horizons identify spatially continuous impermeable ice layers, which may indicate the potential for runoff to occur.

Here we investigate the continuity of layer stratigraphy in the firn column of the percolation zone, the relationship between layer stratigraphy and internal reflection horizons, and the information that internal reflecting horizons reveal about the firn column. We present and analyze 3D GPR grid surveys with high spatial resolution collected in conjunction with multiple ~10 m firn cores. Data were collected at two sites, one near the top of the percolation zone, and one near the transition between percolation facies and soaked facies.

2.2 Methods

2.2.1 Study Sites

We collected data at two sites in the percolation zone of the GrIS near the Expedition Glaciologique au Groenland (EGIG) line (Figure 2.1). Our sites span the region studied by *Braithwaite et al.* [1994], *Pfeffer and Humphrey* [1998], and others [*e.g., Dunse et al.*, 2008; *Parry et al.*, 2007; *Scott et al.*, 2006a, b; *Helm et al.*, 2007]. At Crawford Point, near the top of the percolation zone at 1997 m a.s.l., there were an average of 12.79 melt days per year with a range of 0 to 48 melt days per year between 1979 and 2007 [*Abdalati*, 2007]. At H1 (~1660 m), there were an average of 53.03 melt days per year with a range of 16 to 85 melt days per year over the same period (Figure

2.2). The sites are upstream from Jakobsavn Isbrae and are separated ~50 km horizontally and ~ 300 m in elevation.

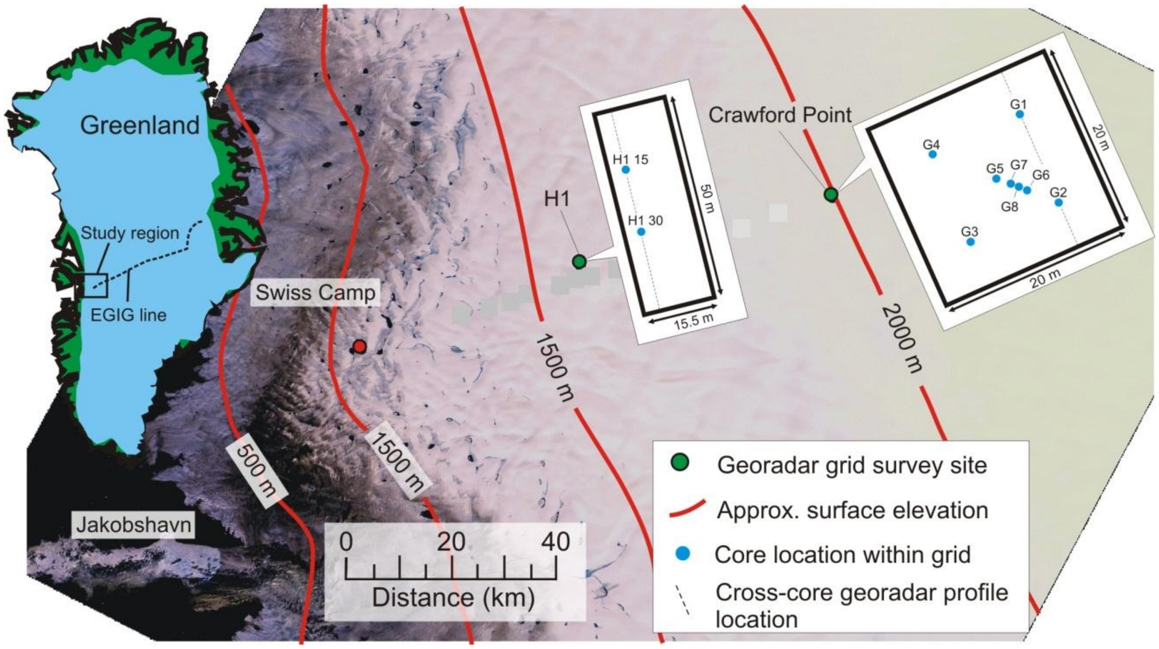

Figure 2.1 ASTER (Advanced Spaceborne Thermal Emission and Reflection Radiometer) image with locations of Crawford Point and H1 shown. GPR grid size and orientation along with core locations are shown for both study sites. Red lines are approximate elevation contours (*Bamber et al.*, 2001). Black dashed lines show locations of GPR profiles shown in Figures 2.3 and 2.5, all GPR data were collected parallel to these lines.

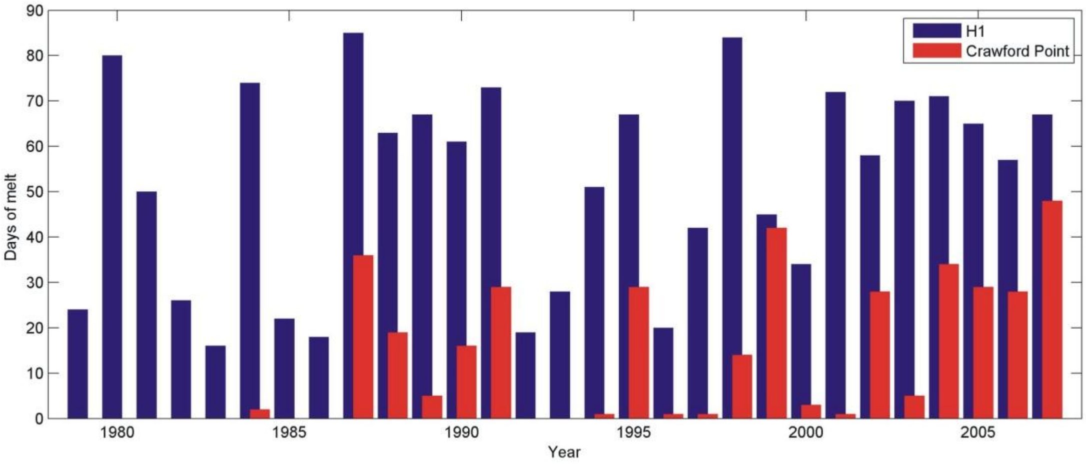

Figure 2.2 Total number of melt days for Crawford Point (red) and H1 (blue) from 1979-2007 (Abdalati, 2007).

2.2.2 3D Common Offset GPR Surveys

In late June 2007, we used a Sensors and Software Pulse Ekko Pro GPR system with 500 MHz antennae to collect data in a 20 m x 20 m grid at Crawford Point. We collected 104 transects with ~0.20 m horizontal line spacing. For each transect, we recorded a trace (consisting of 16 stacked traces) every 0.1 s while walking at a constant pace. This resulted in an average trace spacing of 0.13 m, a maximum trace spacing of 0.165 m, a minimum trace spacing of 0.096 m, and a standard deviation of 0.014 m. Because triggering for trace sampling was based on time and not distance, trace spacing was determined for each line by dividing the total distance traveled by the number of traces recorded along that distance. The 500 MHz radar used at Crawford Point had a vertical resolution of ~0.1 m (1/4 wavelength resolution for 2.0 m/ns velocity) and a horizontal resolution (first Fresnel zone) of ~0.5 m to ~1.5 m at ~1 m and ~10 m depth, respectively.

In May 2008, we used a Sensors and Software Pulse Ekko Pro GPR system with 200 MHz antennae to collect data in a 50 m x 15.5 m grid at H1 (~1650 m.a.s.l.). We used the 200 MHz antennae at this site because the 500 MHz signal did not penetrate to the desired ~10 m firn depth. We collected 35 transects with 0.5 m horizontal line spacing. We used an odometer wheel to record a trace (consisting of 8 stacked traces) every 0.1 m. Because of slipping, build up of snow, and the uneven snow surface the actual trace spacing was between 0.12 m and 0.10 m with a calculated average of 0.115 m and a standard deviation of 0.002 m. The 200 MHz radar used at H1 had a vertical resolution of ~0.25 m and a horizontal resolution of ~0.7 m to ~2.2 m at 1 m and 10 m depth, respectively.

For both sets of data, we applied a low pass filter with a cut off frequency of ½ the peak frequency to reduce very low frequency noise, flattened all traces so that the first arrival is at time zero, and used a time$^{1.2}$ gain function to account for spherical spreading and attenuation of the signal. We linearly interpolated along our transects to create an even grid spacing, then linearly interpolated across transects to create a 3 dimensional data grid with a directional spatial sampling ratio of approximately 4:3 at Crawford point and 5:1 at H1. Further, line spacing was approximately one half wavelength for each survey. The low spatial sampling ratios and small line spacing allows us to interpolate between transects without directionally aliasing our grid.

2.2.3 Core Stratigraphy

We collected a total of 10 cores to ~10 m depth within the two GPR grids, eight at Crawford Point, and 2 at H1 (Figure 2.1). Cores were drilled using a Kovacs coring drill with a power head and ~9 cm inside diameter. Core depths are measured from the surface, which was loose snow at both locations, thus depths are not exact (± 5 cm). We logged the cores in the field recording density, grain size, firn type, and estimated percent ice content. Density measurements were made approximately every 0.15 m to 0.4 m. Firn type, grain size, and estimated ice percent were recorded layer-by-layer. Herein we distinguish between seven metamorphic firn types with varying diagenesis: 1) dry snow – layer above most recent melt surface with no noticeable amount of liquid water content, 2) wet snow – layer infiltrated by current season's melt with a noticeable amount of liquid water content, 3) faceted crystals – buried layer of dry faceted ice crystals, 4) wetted facets – faceted crystals with signs of previous wetting (i.e., slight rounding of facets, partially necked), 5) wetted firn – either firn with evidence of previous wetting (i.e., rounded grains, heavily necked) or frozen slush (same characteristics), 6) unwetted firn – firn with no evidence of previous wetting (i.e. angular ice grains, open pore space), and 7) ice layer or ice pipe – any layer that is pure ice. For layers that had inclusions of ice lenses or ice pipes, we visually estimated the percent pure ice for that layer.

2.2.4 Core/GPR Comparisons

At both locations we collected GPR data prior to collecting cores. We converted GPR two-way travel time (TWT) to depth using average radar propagation velocities (2.10 m/ns for Crawford point, 1.96 m/ns for H1) calculated using a two-phase mixing equation [*Harper and Bradford*, 2003]. For each site, we used the mean core density from all of the cores to calculate the average propagation velocity for that location. Average propagation velocities varied among cores by 0.07 m/ns at Crawford Point and by less than 0.01 m/ns at H1. At Crawford Point, where core data span multiple transects (~50 transects) we picked high amplitude internal reflection horizons in 82 transects of the GPR data, converted core depths to TWT, and plotted the picks with core data that includes ice layers and different diagenic firn types. At H1, both cores are located along a single transect, thus 3D mapping of internal refection horizons is not needed to trace layers between cores. Since the wavelengths of radar used in this study are much greater than firn grain size, it is likely that density variations within the firn column are the main source of radar reflections [*Tiuri et al.*, 1984]. Because density measurements were conducted on each extracted core segment and most core segments consisted of multiple stratigraphic layers, the measured density vs. depth profiles do not accurately reflect density variations of each stratigraphic layer in the firn column. We therefore restrict our radar/core analysis to stratigraphic layers and layer boundaries (boundaries between the seven metamorphic firn types listed in the previous section herein).

2.3 Results

2.3.1 Firn Cores

At Crawford Point, we collected eight firn cores early in the melt season on three days in early July 2007: the first (G1-G5), sixth (G6 and G7), and tenth (G8). New infiltration and refreezing were seen in the top snow layer. In limited cases, we observed infiltration into the firn as a consequence of piping. The cores revealed a large degree of variability in stratigraphic layering over short distances (Figure 2.3). Unwetted firn comprised the largest portion of the cores, layers of wetted firn or frozen slush up to ~1.5 m thick were found in every core. Ice layers, ice pipes, and clusters of ice pipes were present within both wetted and unwetted firn and at some boundaries between wetted and unwetted firn. We identified faceted grains in 6 out of the 8 cores, and dry snow layers in 6 of the 8 cores. Within the upper layer of G5, G1, and G3 we also observed wet snow.

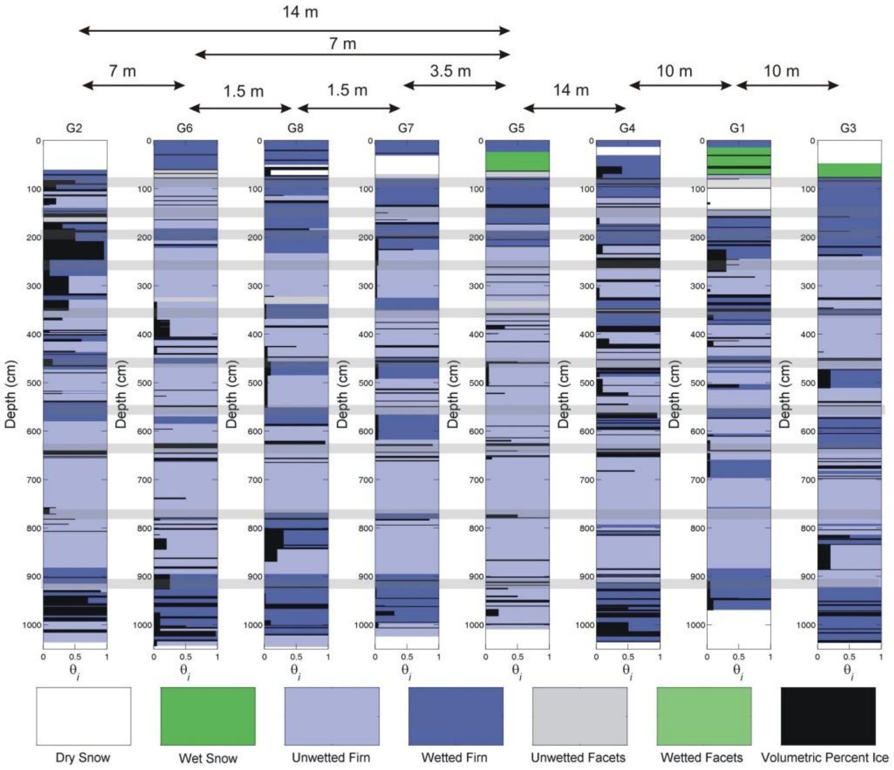

Figure 2.3 Core data from eight cores drilled at Crawford Point. Distances between cores are shown at top of figure, the colors corresponding to firn types are shown in the legend at the bottom of the figure. Light gray lines show the approximate depths of semi-continuous GPR internal reflection horizons. Black bars show approximate volumetric percent of ice at depth.

The H1 cores (H1-15 and H1-30) were collected on the 27th of May 2008 after the first onset of melt, but following an interval of cold temperatures and new snow accumulation, so the surface layer was the winter accumulation layer with no melt related diagenic changes. This surface layer consisted of a wind-scoured surface underlain by

~0.8 m of dry snow with faceted grains below the dry snow to ~1 m (Figure 2.4). Under the faceted grains was a thin ice layer ~0.1 m thick, with a layer of wetted facets below the ice layer. A layer of wetted firn ~2 m thick was below this surface. There was a massive ice layer 0.55 m to 0.60 m thick located at ~3.5 m depth in both cores. The cores had another massive ice layer more than 0.6 m thick that extended from ~7.5 m to ~8.1 m depth. Other massive ice layers within the cores were 0.3 m to 0.5 m thick, but they did not appear in both cores. Nine thinner ice layers appeared to be continuous across the cores between 1.2 m and 9 m depth. Near the end of both cores (at ~10 m depth), there was a layer of unwetted firn that extended to the end of the core at 10.45 m and 10.33 m or core H1-15 and H1-30, respectively. Overall, the cores at H1 had a greater percentage of wetted firn and ice (more than 80%) than at Crawford point (less than 45%).

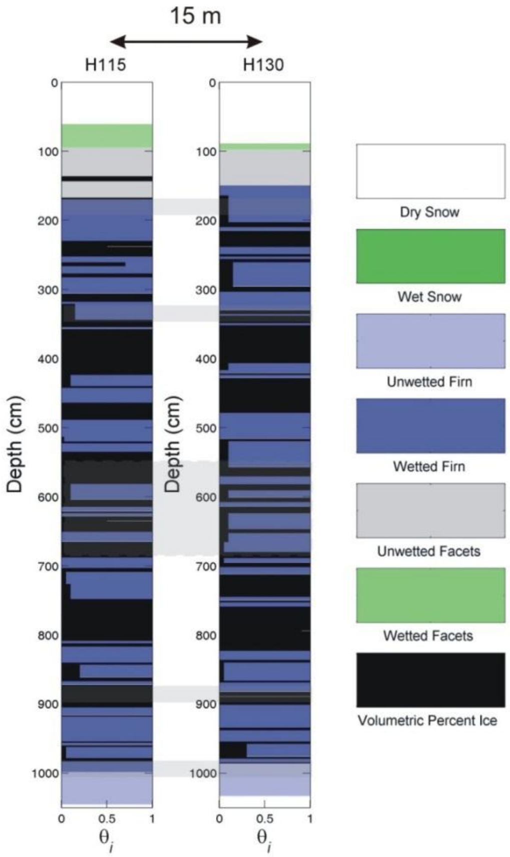

Figure 2.4 Core data from both cores at H1. The distance between the cores is 15 m. The colors corresponding to firn types are shown in the legend at the right of the figure. Black bars show approximate volumetric percent of ice at depth.

2.3.2 3D GPR

At Crawford Point, our 500 MHz common offset profiles show laterally continuous internal reflecting horizons at 9 times between 8 ns and 95 ns (Figure 2.5a). Identification of all of these layers from any single transect is highly problematic due to inconsistency in reflection amplitude and apparent ‘holes’ in each reflection horizon. We therefore identified laterally continuous reflection horizons by combining layer picks from 82 individual transects (Figure 2.5b). Due to a recording error, the other 22 recorded transects lost data below ~8 m depth and were not used to pick layers. Above 8 ns, as well as between 48 ns and 65 ns, there are several discontinuous layers. Between 35 ns and 48 ns was a region of high reflectivity with no obvious internal structure. The region between 25 ns and 35 ns had very few reflections. Although there were laterally continuous horizons throughout the grid, all of the horizons had holes (regions where reflections were not identifiable in either in-line or cross-line directions) and all of the horizons had lateral variations in amplitude. Even so, we use the term ‘laterally continuous’ herein to refer to these mostly continuous internal reflection horizons. Figure 2.6 shows an interpolated surface (light blue) picked from the horizon with the highest level of continuity (at ~15 ns or ~1.5 m). This surface is well defined through 82 separate transects (Figure 2.5b), and reveals small-scale undulations in the surface as well as gaps in the reflection horizon. Some of the gaps in the reflecting horizon are more than 2 meters across. At H1, 200 MHz common offset radar revealed laterally continuous internal reflection horizons at 6 depths between 15 ns and 120 ns (Figure 2.7). There is a region of high reflectivity between ~40 ns and ~80 ns where internal reflection horizons are continuous across 5-50 m in some GPR profiles, but are completely absent from profiles separated by as little as 2 to 5 meters.

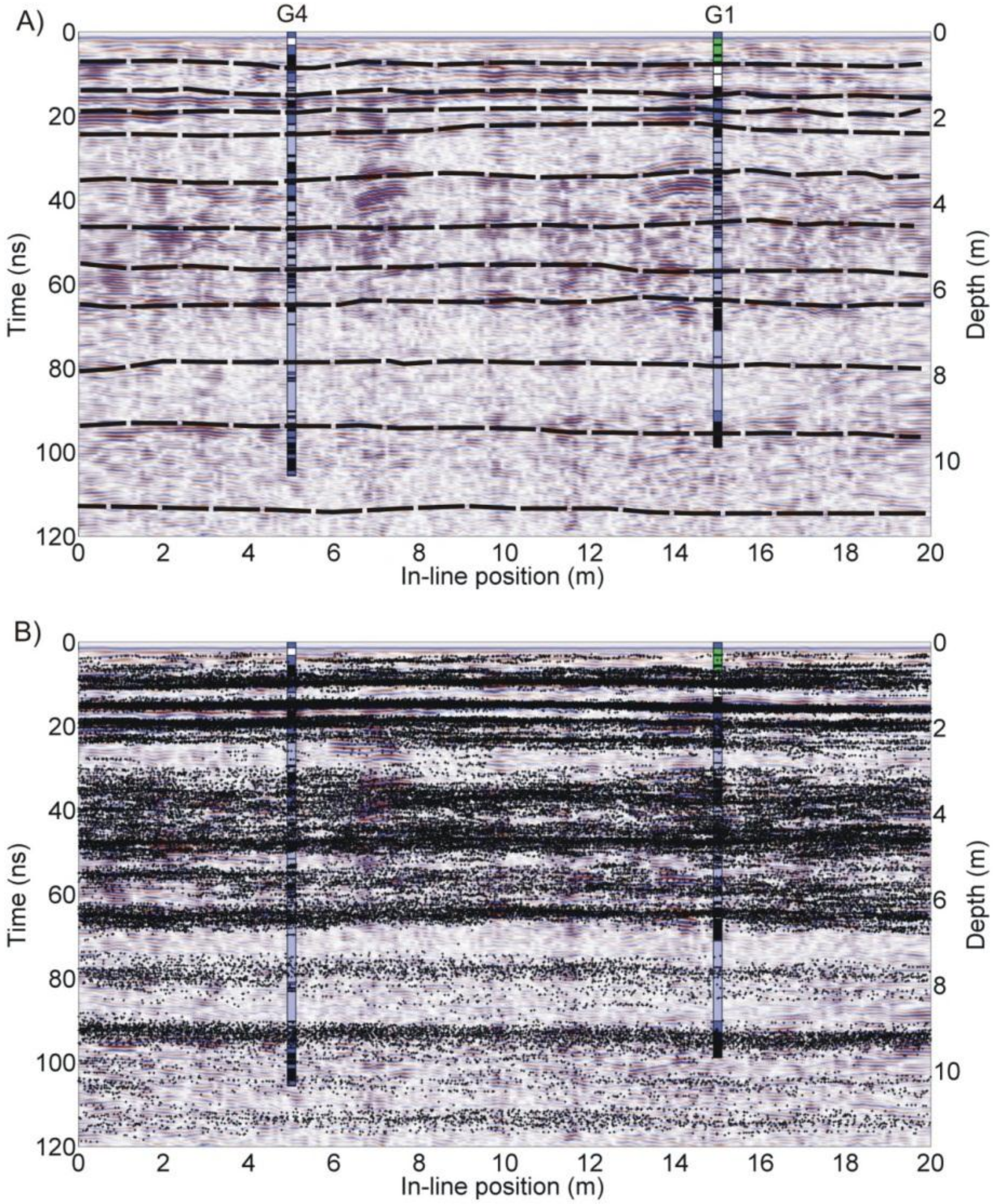

Figure 2.5 (a) GPR profile from Crawford Point (500 MHz) with 2 core intersections shown. Colors in the cores represent firn/snow types: black is ice, dark blue is wetted firn, light blue is dry firn, green is wet snow, and white is dry snow. Black dashed lines show locations of semi-continuous internal reflection horizons. (b) All of the laterally coherent high reflectivity picks made on 82 transects within the Crawford Point GPR grid overlain on the radar profile in a. Because internal reflection horizons are not completely laterally continuous, these picks form the basis of our interpretation of internal reflection horizons.

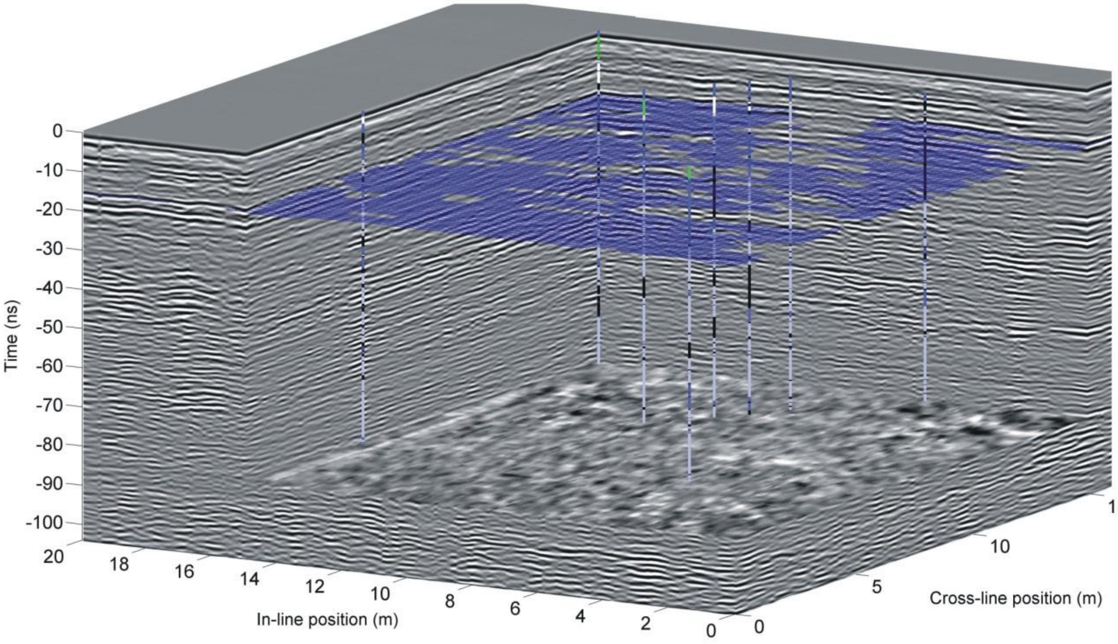

Figure 2.6 GPR 3D grid from Crawford Point with all core locations shown. Colors in the cores represent firn/snow types: black is ice, dark blue is wetted firn, light blue is dry firn, dark green is wet snow, white is dry snow, and light green is faceted grains. We show a mapped layer with holes (light blue) at ~1.5 m depth. This figure shows the overall lateral continuity of the internal reflection horizons and the lack of continuity across cores.

2.4 Discussion

At Crawford Point, we found no stratigraphic correlation between 8 firn cores over any distance between 1.5 m and14 m. However, within the 3D GPR grid data, we identified 9 internal reflection horizons in the top ~9.8 m. Although none of the horizons were completely laterally continuous, they each constitute an easily identifiable surface in both in-line and cross-line directions. By comparing identified reflection horizons with core data (Figures 2-3 and 2-6), it is apparent that internal reflection horizons do not correlate with any single stratigraphic layer or sequence of layers identified in the cores.

For example, there are no laterally continuous ice layers, no common transitions from wetted to unwetted firn, or any other stratigraphic features that can be interpreted as the source of laterally continuous reflection horizons. The variations in amplitude observed in the reflection horizons may be due to lateral variations in density contrasts, layer thickness, or configuration of thin layer packages.

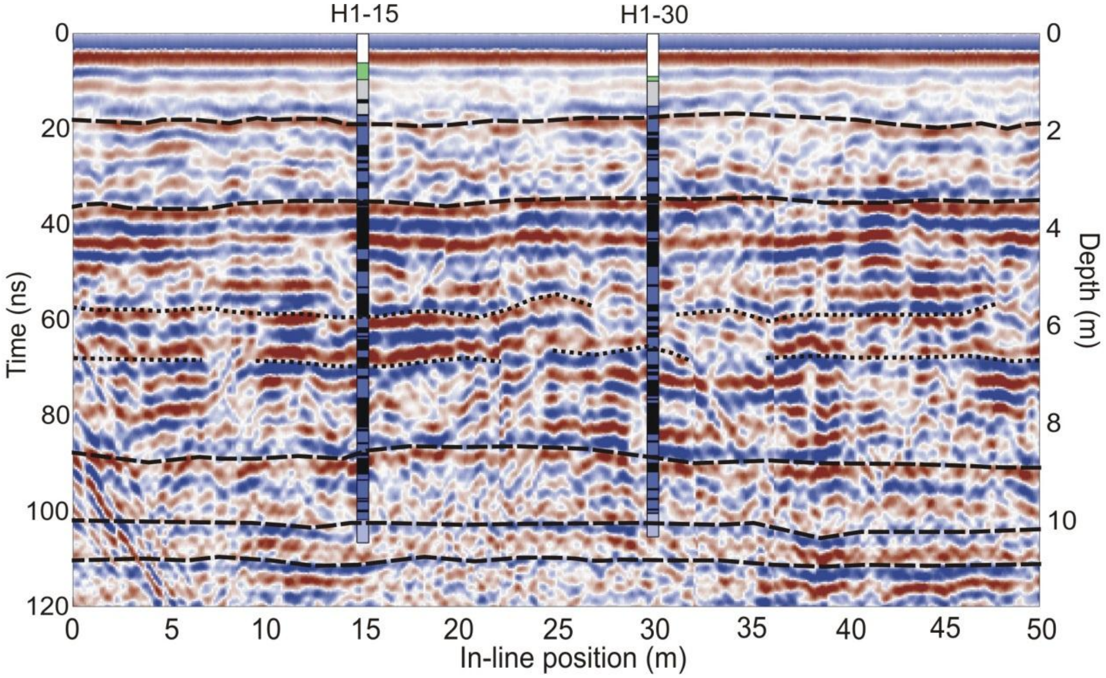

Figure 2.7 GPR profile from H1 (200 MHz) with both core intersections shown. Colors in the cores represent firn/snow types: black is ice, dark blue is wetted firn, light blue is dry firn, dark green is wetted facets, gray is dry facets, and white is dry snow. Black dashed lines show locations of continuous internal reflection horizons. Black dotted lines show locations of horizons from massive regions of high reflectance; these horizons are not laterally continuous over the area of the grid.

Our results at Crawford Point are consistent with previous studies that show that, although ice lenses and ice pipes are heterogeneously distributed throughout the near-surface snow and firn [*Parry et al.*, 2007], internal reflection horizons are usually related to vertically bounded sequences of ice layer clusters [*Dunse et al.*, 2008] at ~1875 m elevation along the EGIG line. Our cores showed that the distribution of ice layers and ice pipes are laterally and vertically heterogeneous when measured over the cross-sectional area of a typical core (~$6\text{x}10^{-3}$ m^2). However, since the internal reflection horizons were laterally continuous over tens of meters, we believe that there is preferential vertical distribution of ice layers and ice pipes as measured over the footprint of the GPR (~0.65 m^2 at the surface, ~4.25 m^2 at 1 m depth, calculated using: $A = {}^{\lambda}\!/_{4} - {}^{d}\!/_{\sqrt{(\varepsilon_r - 1)}}$ [Figure 14, *Annan and Cosway*, 1992] where A is ½ of the aperture of the signal along the primary axis of an elliptically spreading footprint, d is depth, and ε_r is the relative dielectric permittivity of the propagating medium). It is well established that previous windblown surfaces restrict vertical flow and enhance lateral flow of meltwater [*Bøggild*, 2000; *Parry et al.*, 2007]. It is also established that grain size differences can create boundaries that inhibit the vertical flow of small amounts of water. Both windblown surfaces as well as grain size boundaries are present throughout annular layers [*Benson*, 1960; *Parry et al.*, 2007]; however, within ~20 km and 50 m elevation of Crawford Point, 18% of identified ice layers are associated with fine-to-coarse grain boundaries [*Parry et al.*, 2007]. *Benson* [1960] describes how these grain size boundaries are often associated with fine grained winter snow accumulation overlying a coarser grained, less dense layer that accumulates in the short fall season. He further states that in regions of melt, this discontinuity is often slightly above the summer melt surface. Because these discontinuities, which are associated with previous summer surfaces, can act as aquitards, we suggest that diagenic features such as ice layers, ice pipes, faceted grains, and wetted firn preferentially occur near density boundaries delineated by previous summer surfaces at Crawford Point. Further, we contend that this preferential distribution is not apparent over the area sampled by a single core, whereas over the footprint of the radar (which is approximately four orders of magnitude greater area than the core), the preferential distribution of melt induced diagenic features is apparent.

Although the vertical resolution of the radar used at Crawford Point was ~0.1 m and the vertical resolution of the radar used at H1 was ~0.25 m, there is a stronger correlation between laterally continuous internal reflection horizons and core stratigraphy at H1 than at Crawford Point. This is probably because total annual melt is greater at H1 than at Crawford Point. In years where melt occurs at both H1 and Crawford Point (Figure 2.2), there is an average of ~14.5 times as many melt days at H1 than at Crawford Point [*Abdalati*, 2007]. The relatively large amount of melt and infiltration creates massive ice layers ~0.5 m thick and a firn stratigraphy that is composed mostly of wetted firn and ice layers [*Braithwaite et al.*, 1994; *Pfeffer and Humphrey*, 1998].

At H1, we can correlate three laterally continuous internal reflection horizons to significant transitions in firn stratigraphy: 1) the transition from faceted grains to wetted firn at ~1.5 m, 2) the massive ice layer at ~3.5 m – 4 m, and 3) the transition from wetted firn to non-wetted firn at ~ 10 m. These are all likely sources of internal reflection horizons. The corresponding reflection horizons are also the most laterally consistent through the data. The volume between the massive ice layer (2) and the non-wetted firn (3) contains many stratigraphic layers that could be laterally continuous across the cores, including the massive ice layer observed in each core at ~7.5 m depth. However, between the reflection horizons at ~4.1 m and ~11.6 m, there are only two reflection horizons, both of which are laterally discontinuous across the grid, although they do appear in most transects. Because the reflection horizons found at this depth are laterally discontinuous, it is likely that the firn stratigraphy between 4 m and 10 m is highly laterally heterogeneous and that the apparent stratigraphic correlations between 4 m and 10 m across the cores at H1 are due to 1) the simple layer stratigraphy (only wetted firn and ice) found in the cores as well as 2) the limited number of cores logged in the grid region. However, it is possible that the vertical resolution of the 200 MHz radar (~0.25 m) is too coarse to identify individual layers in this region unless the layers are massive.

If we assume that the 2007/2008 winter accumulation at H1 (~0.328 m water equivalent, defined by the non-wetted snow layer) is roughly average and we assume that the summer accumulation increases the total accumulation by 55%, as *Parry et al.* [2007] observed at ~1875 m.a.s.l. along the EGIG line, then the total yearly accumulation is roughly 0.51 m water equivalent. Below the last melt surface (~1 m depth), we measured an average firn density of ~635 kg/m^3. Using this average firn density, we calculated that the thickness between surfaces that we identified in the GPR are roughly equivalent to 1.7 to 3.8 years of accumulation (similar calculations for Crawford Point give a range of 0.94 to 1.14 years of accumulation for each internal reflection horizon). This estimate assumes that no melt water leaves the area as runoff or infiltrates past the maximum core depth, thus it should be considered a lower bound. Under these conditions, it is unlikely that the reflecting horizons at H1 occur at previous summer surfaces but instead they likely occur at density boundaries that are formed by multiyear variations in melt (variations in overall melt that occur slowly over 2-10 years as opposed to single melt events that occur in a single season).

Arcone et al. [2004], among others, have successfully traced identifiable internal reflecting horizons across long distances (90+ km), tying firn core depth/age relationships to each other in Antarctica, implying that this would also work in the dry snow facies of the GrIS. The ability to tie distant cores together with GPR data is important for understanding spatial variations in accumulation rates and determining accumulation rates in regions where no cores exist [*Bales et al.*, 2009]. In the percolation zone, however, we find potential problems with determining accumulation rates by tying cores to GPR data. In high elevation portions of the percolation zone like Crawford Point (~1997 m a.s.l.), firn stratigraphy is complex and laterally heterogeneous, but reflection horizons are probably isochrones and seasonally variable signals are identifiable. However, the load vs. depth (calculated from core density profiles) varies by an average of 20% (1.5 m to 14 m), and affects radar velocities by ~3% to 7% over short distances (1.5 m to 14 m). Thus, the apparent depth of layers is affected to the same degree. Because we use a constant velocity to convert radar travel time to depth, correlation between cores and radar reflection horizons across the grid at Crawford Point should only be considered approximate. However, because there was no cross-core stratigraphic correlation at Crawford Point, detailed correlation between reflection horizons and core stratigraphy would not be possible even with totally accurate depth conversions. The effects of the velocity variation on the average depth of reflection horizons may be limited by spatially smoothing the recorded signal and accurately determining the average velocity vs. depth over the corresponding distance. At H1 (~1660 m a.s.l.), internal reflection horizons likely represent multiple years of accumulation and stratigraphic features (such as massive ice layers) may form over multiple years. This is probably because total annual melt is greater at H1 than at Crawford Point. In years where melt occurs at both H1 and Crawford Point (Figure 2-2), there is an average of ~14.5 times as many melt days at H1 than at Crawford Point [*Abdalati*, 2007]. The relatively large amount of melt and infiltration creates massive ice layers ~0.5 m thick and a firn stratigraphy that is composed mostly of wetted firn and ice layers [*Braithwaite et al.*, 1994; *Pfeffer and Humphrey*, 1998]. This uncertainty of the age of identified reflection horizons may limit the usefulness of common offset GPR data in mapping variations in accumulation.

Our results show that at H1 a massive ice layer ~0.5 m thick extends over the grid area (20 m x 50 m) at approximately 4 m depth. This ice layer may satisfy the conditions for runoff in the percolation zone as they are described by *Pfeffer et al.* [1991]. Further, the extent of the ice layer can be easily mapped with GPR. At Crawford Point, however, firn cores showed that there was no laterally extensive ice layer over the grid area (20 m x 20 m). GPR profiles also showed large holes in internal reflection horizons. This suggests that firn conditions near Crawford Point would not support lateral flow of water over distances greater than tens of meters.

2.5 Conclusions

The melt/infiltration near Crawford Point creates a complex firn column with lateral heterogeneity over length scales of at least 1.5 m to 14 m. This complex stratigraphy makes visual identification of annual layering ambiguous. However, the presence of internal reflection horizons within the GPR grid shows that over the footprint of the radar, lateral homogeneity does exist. This may be due to preferential ice layer formation at previous summer surfaces [*Dunse et al.*, 2008]. Thus, near Crawford Point, although internal reflection horizons are likely isochrones, they do not correlate well with stratigraphic boundaries identified in cores. Further, firn stratigraphy recorded in a single core at Crawford Point is not representative of the firn stratigraphy of the surrounding area (1 km^2 - 5 km^2).

The intermittent wetted firn and ice layers observed throughout more than 80% of the core length at H1 show that wetting fronts propagate through the seasonal snowpack and likely into the underlying firn where they freeze to form ice pipes and ice layers, some of which are greater than 0.5 m thick. Here, continuous internal reflection horizons correlate with massive ice layers or stratigraphic boundaries between wetted firn and dry firn. Each internal reflection horizon identified at H1 is separated from other reflection horizons by multiple years of accumulation, thus previous summer surfaces are not likely sources for the reflection horizons.

Using common-offset GPR surveys in conjunction with firn or ice cores to map variations in accumulation rates is more difficult in the percolation zone than in the dry-snow facies. Near Crawford Point, radar propagation velocities vary over short distances.

Therefore, to more accurately measure the average depth to the isochronal internal reflection horizons, spatial smoothing of traces and multiple velocity estimates are needed. Near H1, a single core is likely representative of the surrounding area (1 km^2 - 5 km^2). Internal reflection horizons are likely from multi-annual horizons, therefore dating of the firn cores is needed to determine age to the reflecting horizons. Where annual signals in the firn are obscured by melting, accurate mapping of variations in accumulation will be ambiguous.

2.6 Acknowledgements

This work was funded by U.S. National Science Foundation grant OPP-ANS #0612506. We would like to thank two anonymous reviewers for their insightful comments, which greatly improved this manuscript.

CHAPTER THREE: GEORADAR DERIVED ESTIMATES OF FIRN DENSITY IN THE PERCOLATION ZONE, WESTERN GREENLAND ICE SHEET*

This chapter is published by the American Geophysical Union in *The Journal of Geophysical Research* and should be referenced appropriately.

Brown, J., J. Bradford, J. Harper, W. T. Pfeffer, N. Humphrey, and E. Mosley-Thompson (2012), Georadar-derived estimates of firn density in the percolation zone, western Greenland Ice Sheet, *J. Geophys. Res.*, 117, F01011, doi:10.1029/2011JF002089.

*This chapter includes modifications from the originally published version.

GEORADAR DERIVED ESTIMATES OF FIRN DENSITY IN THE PERCOLATION ZONE, WESTERN GREENLAND ICE SHEET

Joel Brown [1,2]

John Bradford [1]

Joel Harper [2]

W. Tad Pfeffer [3]

Neil Humphrey [4]

Ellen Mosley-Thompson [5]

Accepted for publication in:

Journal of Geophysical Research – Earth Surface

November, 2011

[1] *Center for Geophysical Investigation of the Shallow Subsurface, Boise State University*

[2] *Department of Geosciences, University of Montana*

[3] *Institute of Arctic and Alpine Research, University of Colorado, Boulder*

[4] *Department of Geology and Geophysics, University of Wyoming*

[5] *Byrd Polar Research Center, The Ohio State University*

Abstract

Greater understanding of variations in firn densification is needed to distinguish between dynamic and melt driven elevation changes on the Greenland Ice Sheet. This is especially true in Greenland's percolation zone where firn density profiles are poorly documented because few ice cores are extracted in regions with surface melt. We used georadar to investigate firn density variations with depth along a ~70 km transect through a portion of the accumulation area in western Greenland that partially melts. We estimated electromagnetic wave velocity by inverting reflection traveltimes picked from common midpoint gathers. We followed a procedure designed to find the simplest velocity vs. depth model that describes the data within estimated uncertainty. Based on the velocities, we estimated 13 depth/density profiles of the upper 80 m using a petrophysical model based on the complex refractive index method equation. At the highest elevation site, our density profile is consistent with nearby core data acquired in the same year. Our profiles at the six highest elevation sites match an empirically based densification model for dry firn, indicating relatively minor amounts of water infiltration and densification by melt/refreeze in this higher region of the percolation zone. At the four lowest elevation sites, our profiles reach ice density at substantially shallower depths, implying considerable melt water infiltration and ice layer development in this lower region of the percolation zone. The separation between these two regions is 8 km and spans 60 m of elevation, which suggests that the balance between dry-firn and melt-induced densification processes is sensitive to minor changes in melt.

3.1 Introduction

Temporal variations in firn density can partially explain observed changes in ice sheet surface elevation [*Holland et al.*, 2011] and can substantially influence mass balance calculations based on surface elevation observations [*Zwally et al.*, 2005; *Helsen et al.*, 2008]. Firn densification rates are related to mean annual air temperature [e.g., *Herron and Langway*, 1980], which varies both temporally and spatially over the Greenland Ice Sheet (GrIS). Thus, a solid understanding of spatial variations in current firn density with depth profiles on the GrIS can help elucidate changes in firn density under a changing climate. Process-based firn densification models have increased our understanding of compaction rates in areas with little or no surface melt [e.g., *Zwally and Li*, 2002], but current observational constraints on firn density with depth are very poor in regions of the accumulation area receiving more than negligible amounts of melt.

Densification of firn in regions of the GrIS accumulation area that do not melt is primarily driven by overburden, with spatial variations in densification rates linked to temperature and accumulation rate [*Herron and Langway*, 1980]. Theoretically, the dominant densification processes with increasing depth result in order, from 1) settling (physical rounding and packing, as well as sublimation and diffusion); 2) recrystallization and deformation; 3) deformation with maximum crystal surface contact (this ‘creep’ pushes air out of the firn); and finally, 4) compression of closed-off air bubbles within the ice (also due to creep) [*Paterson*, 1994; *Maeno and Ebinuma*, 1983]. The densities at which the transitions between these processes occur are typically given as 550 kg/m^3, 730 kg/m^3, and 830 kg/m^3 [*Paterson*, 1994; *Maeno and Ebinuma*, 1983]. More recent studies reveal that these transition densities vary spatially and are not always identifiable in cores [*Hörhold et al.*, 2011].

However, more than 1/3 of the GrIS has net positive accumulation and receives some amount of surface melt annually [*Nghiem et al.*, 2005]. Although this area includes both the percolation and soaked facies, as described by *Benson* [1960], there is no surface expression for the boundary between them; thus, we refer to this area as the 'percolation zone.' The size and distribution of the percolation zone is annually transient because of yearly variations in total accumulation and extent of melt. Within the percolation zone, surface meltwater infiltrates the snow layer and refreezes to form ice layers, ice lenses, and ice pipes [e.g., *Benson*, 1960; *Pfeffer et al.*, 1991]. This process of melt and refreeze results in densification processes that deviate from the typical densification model for dry firn. Georadar surveys within the percolation zone reveal a layered subsurface with laterally continuous high reflectivity horizons that are often interpreted as previous summer surfaces [e.g., *Dunse et al., 2008*; *Legarsky and Gao*, 2006]. Detailed shallow core and snow-pit studies of the upper few meters of firn within the percolation zone [e.g., *Benson*, 1960; *Fischer et al.*, 1995; *Parry et al.*, 2007; *Dunse et al.*, 2008] reveal seasonal high-density layer boundaries. Throughout this layered structure are ice lenses and ice pipes. All of these observation techniques show increased meltwater retention with a decrease in elevation until complete saturation of the surface layer is eventually reached by the end of the melt season [*Braithwaite et al.*, 1994].

Cores collected in the upper regions of the percolation zone [e.g., *Mosley-Thompson et al.*, 2001] span the full depth of the firn column from the annual snow layer to the theoretical firn close-off density of ~830 kg/m^3 [*Paterson*, 2002]. These cores have been used to calculate long term average accumulation rates, density vs. depth relationships (dρ/dz), and densification rates (changes in density with time (dρ/dt)). The ability to determine these rates depends on the identification of annual signals in the core. This is difficult in regions with melt because they have more vertical dispersion of possible seasonal indicators (dust, δ^{18}O, δD, etc.) [*Hou and Qin*, 2002] than do regions without melt. Thus, the quality of information preserved in cores is limited where melt is substantial and therefore, cores acquired in the percolation zone are usually short and from regions with very little melt. Therefore, the effect of increased surface melt on firn densification through the entire firn column is largely unknown. This is especially true at lower elevations of the percolation zone.

Common midpoint (CMP) georadar surveys have been used to estimate the average electromagnetic (EM) propagation velocity as a function of depth for the firn column in the dry snow zone of the GrIS [e.g., *Hempel et al.*, 2000]. Where the focus of these surveys is to match common offset radar reflection horizons with contemporaneous features in ice cores [e.g., *Hempel et al.*, 2000], it is common to treat the firn column as a single layer and determine the normal moveout (NMO) stacking velocity (v_{NMO}) of the firn column, which closely approximates the root mean square (RMS) velocity (v_{RMS}) in a horizontally layered homogeneous medium [*Yilmaz*, 2001]. There are many methods for calculating v_{NMO}. The most precise method is to pick traveltime vs. offset curves along the first break of a coherent reflection and linearly fit the resultant curve in the time squared vs. distance squared domain; however, semblance analysis is most often used to determine v_{NMO}. In a multi-layered system, there are also many methods for calculating the average velocity of each layer, or interval velocity. The Dix inversion, which solves for layer velocities using only stacking velocities and zero-offset traveltimes [*Dix*, 1955], is the most common method of calculating interval velocities.

Here we use CMP georadar surveys to calculate how firn column density varies with depth at 13 locations along the EGIG (Expédition Glaciologique Internationale au Groenland) line within the percolation zone of the GrIS. We collected our data in the summers of 2007 and 2008; they span ~70 km laterally and 600 m of elevation (1997 m to 1401 m) from Crawford Point toward Swiss Camp (Figure 3.1). We avoid the NMO analysis/Dix inversion method for two reasons: (1) Dix inversion is subject to assumptions of NMO, which include small offset-to-depth ratio and small velocity gradients over reflection boundaries [*Bradford*, 2002], and (2) Dix inversion is sensitive to small errors in NMO velocity and near-offset traveltime picks. Instead, we employ the traveltime inversion method of *Zelt and Smith* [1992], which is not subject to the assumptions of NMO. We follow a set of explicit rules to solve for the electromagnetic (EM) velocity structure of the firn column. We create and follow an inversion flow (Figure 3.2) to find the simplest velocity vs. depth model that describes the data within estimated uncertainty, reduce sensitivity to small errors in velocity, limit user bias, and to give a basis for evaluating how well our results fit the data in the context of physically realistic firn density models. Our method has four steps: (1) picking time vs. offset moveout curves from georadar data, (2) using a traveltime inversion to invert for a 1-D depth-velocity model, (3) checking the solution with forward modeling for quality control

(QC), and (4) solving for layer density from radar velocity. Our method allows us to calculate the density profile for the entire depth of the firn column at all locations in this survey. We include comparisons to a firn compaction model that neglects the influence of melt [*Herron and Langway*, 1980] at every location, and to core data at Crawford Point.

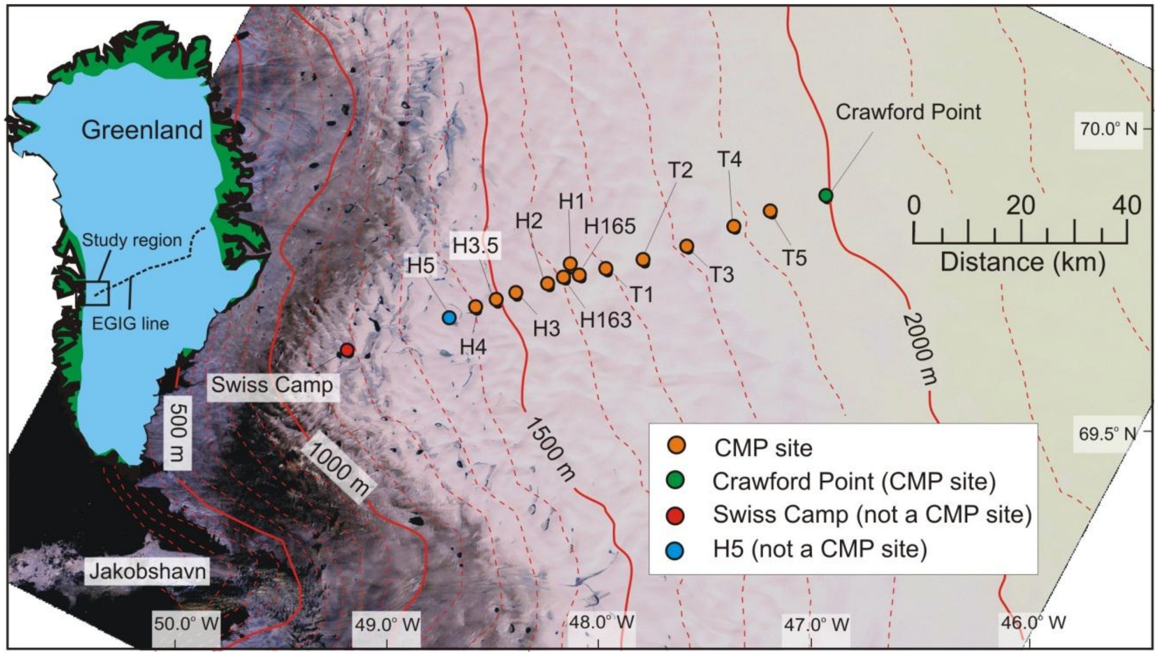

Figure 3.1 ASTER (Advanced Spaceborne Thermal Emission and Reflection Radiometer) image with CMP radar sites marked. The EGIG line and the approximate location of the ASTER image are marked on the map of Greenland. Red elevation contours are approximated from 5 km gridded elevation data [*Bamber*, 2001].

Radar propagation velocity in dry snow primarily depends on snow density [*Tiuri et al.*, 1984]. However, radar velocity in the presence of liquid water is a function of both density and volumetric water content [e.g., *Bradford et al.*, 2009]. Temperature data during the nine days of data collection indicate that surface melt likely occurred at some sites during data collection during the 2007 field season (Table 3.1). Indeed, surface snow was noticeably wet at T1, T2, and T3; small amounts of liquid water may also have been present near the surface at T4, T5, and Crawford Point when we collected data. We drilled firn cores to ~10 m depth at the midpoint of each CMP. Each core had evidence of past melt and refreeze such as ice lenses and ice pipes throughout the core. However, these cores did not show evidence of liquid water. Furthermore, measured 10 m depth firn temperatures were between -16 °C and -3 ºC. Thus, we assume that the amount of deeply infiltrating liquid water at any given time in any given location is negligible.

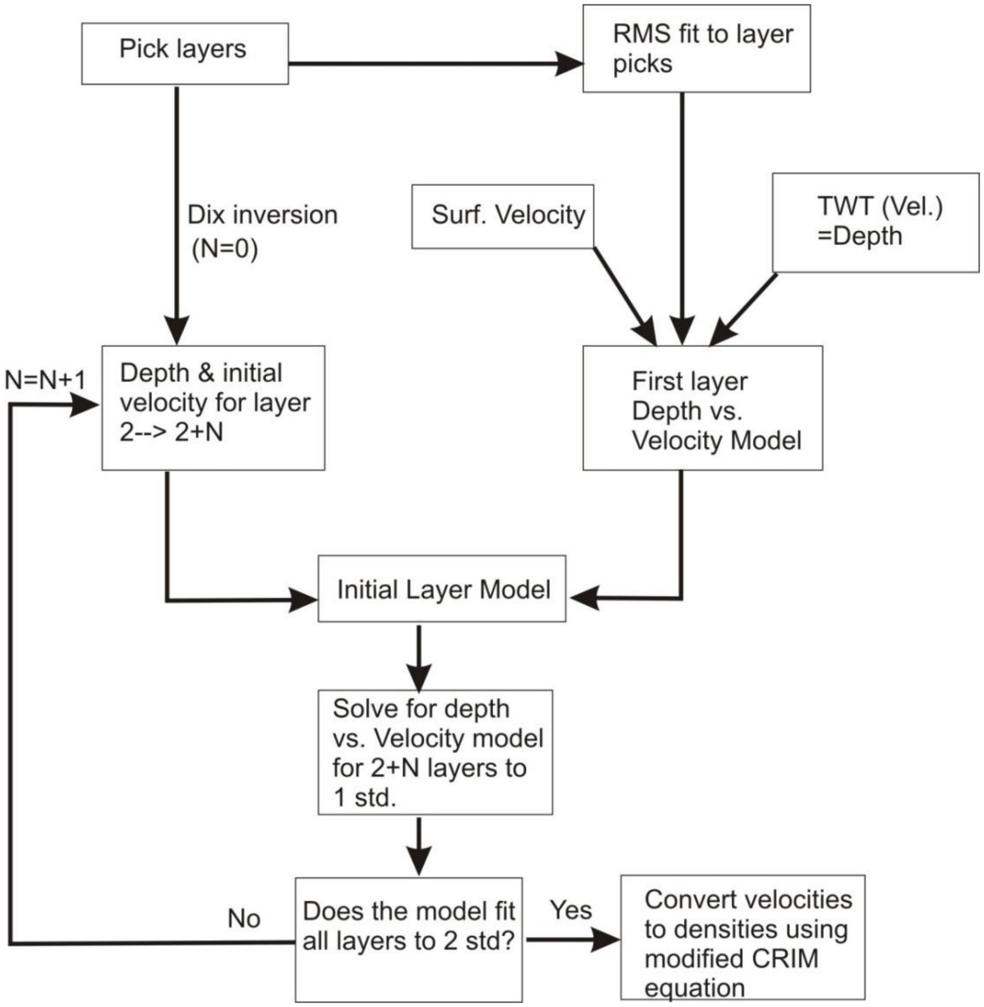

Figure 3.2 Flow chart for the inversion process.

3.2 Methods

3.2.1 Data Acquisition

We used a Sensors and Software pulseEKKO PRO georadar system with 100 MHz antennas. Our offset range was 1 m to 80 m with a moveout interval of 0.8 m in 2007 and 0.5 m in 2008. We recorded for 1820 ns per trace but coherent reflections were not apparent below 1500 ns. For processing, we assumed that firn layers were laterally homogeneous and parallel over the length scale of the moveout profiles at each site. However, shallow core (10 m) and common-offset data revealed that layering is not laterally homogeneous and density varied by an average of 20% over the depth of the cores at Crawford Point (~1997 m a.s.l.) and by 2% at H1 (~1680 m a.s.l.) [*Brown et al.*, 2011]. Fortunately, lateral density variations decreased with depth. Furthermore, the length scale of lateral density variations is small (<5 m), and therefore average out over the width of the CMP. The amplitude of surface roughness from sastrugi was less than ~0.2 m over the 80 m offset. This roughness causes a waviness in the direct subsurface wave, either through variation in the propagation velocity or scattering that interferes with the direct wave (Figure 3.3b). However, linear fits to the direct subsurface wave produced surface velocity estimates with standard deviations of less than ±0.003 m/ns at most locations. Because dip slopes and the slopes of the sastrugi were small, residual moveout errors are negligible.

3.2.2 CMP Surveys

Figure 3.3a shows a common midpoint radar profile with handpicked moveout curves superimposed. Data processing included a time-zero shift to correct for trace start time delay and traveltime drift with temperature in the electronics, a 25-50-200-400 MHz Ormsby bandpass filter to reduce low and high frequency noise, and a time-variable gain function of $t^{1.2}$ to compensate for attenuation due to absorption and spherical spreading. We picked moveout curves using a semi-automatic picking routine in ProMAX (seismic processing software from Halliburton) that identifies the peak in the wavelet closest to a handpicked point. We then adjusted our picks to that of the first break of the wavelet to account for the finite bandwidth of the signal. Because shallow moveout curves are dominated by direct subsurface waves at long offsets, we limited our picks to offsets smaller than that at which the reflections merge with the direct subsurface wave. For each location, we picked traveltime vs. offset data for as many coherent (constant relative phase of waveform) reflections as were present in the data up to a total of eleven. The shape of the traveltime curves is a function of the depth to the boundary causing the reflection and the velocity of all overlying material.

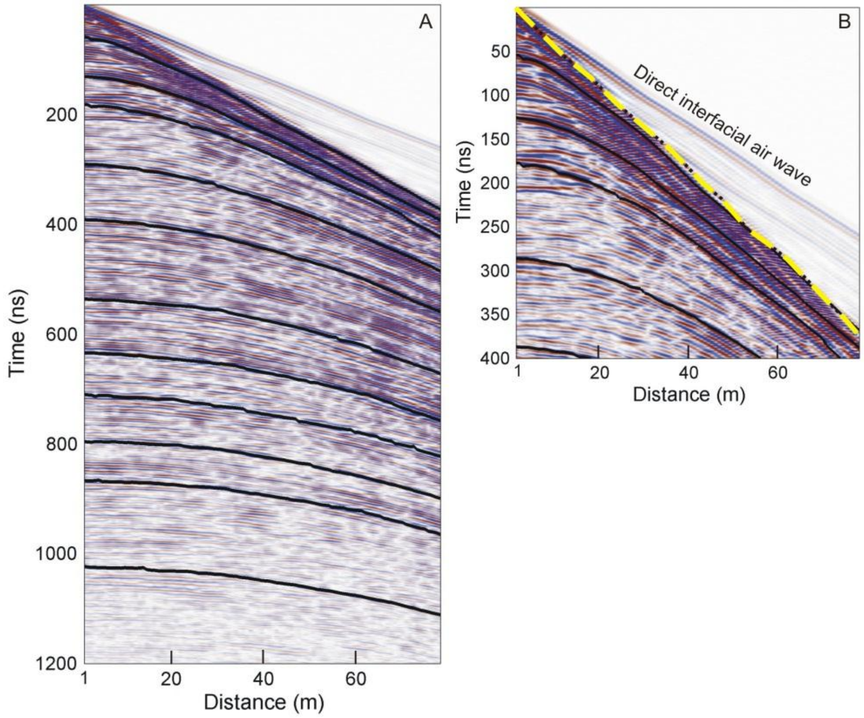

Figure 3.3 Example of georadar CMP data (A) with picks (black lines) from T5. A magnified view of the upper 400 ns (B) reveals the waviness of the direct subsurface wave (yellow and black dashed line).

3.2.3 Velocity vs. Depth

We employ the method of *Zelt and Smith* [1992] to solve for the velocity vs. depth structure of the firn column. The method utilizes a ray-based forward model to compute traveltimes coupled with a damped least-squares inversion algorithm to find the layered velocity model that produces the best fit to traveltime picks within the CMP data. As with all velocity estimation methods, traveltime inversion is non-unique. Therefore, we developed rules to assure that the inversion procedure was consistent across all sites with an end objective of comparing relative variations in the final density vs. depth models.

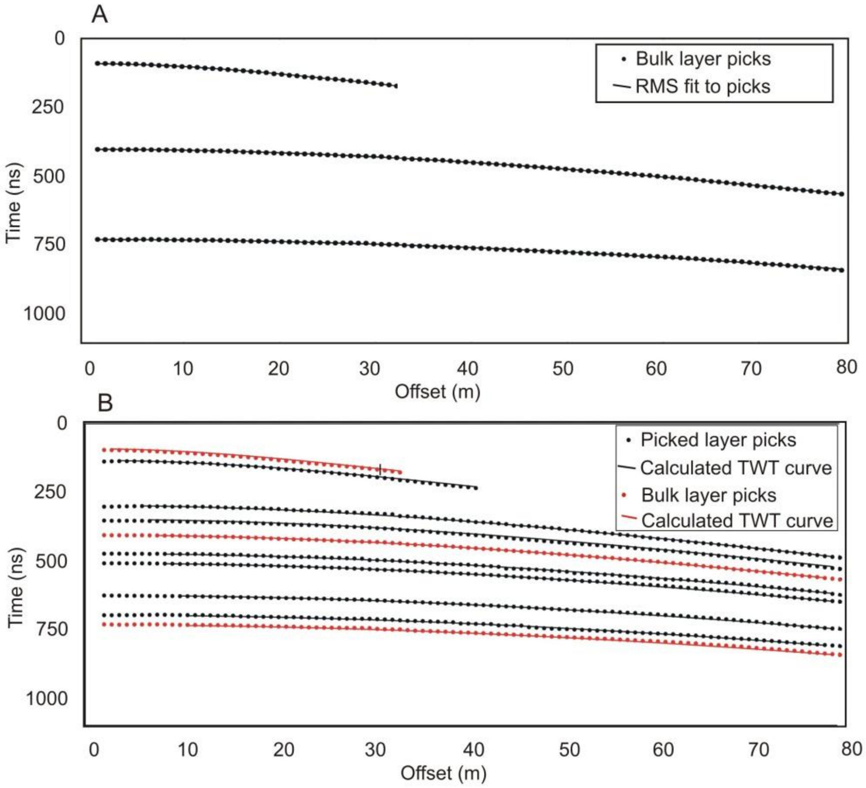

Figure 3.4 (A) Bulk layer picks from Crawford Point CMP data with RMS fit. (B) Modeled TWT fit to all picked layers (both black and red) at Crawford Point. Bulk layers used for the inversion are shown in red.

The rules constrain variability in the inversion by iteratively solving for the depth and propagation velocity rather than solving for both simultaneously. Further, instability of the inversion increases as the number of layers increases and as the thicknesses of the layers decrease; therefore, we chose to solve for the simplest model (least number of layers) that describes all of the traveltime picks to within a specified uncertainty threshold (Figure 3.4).

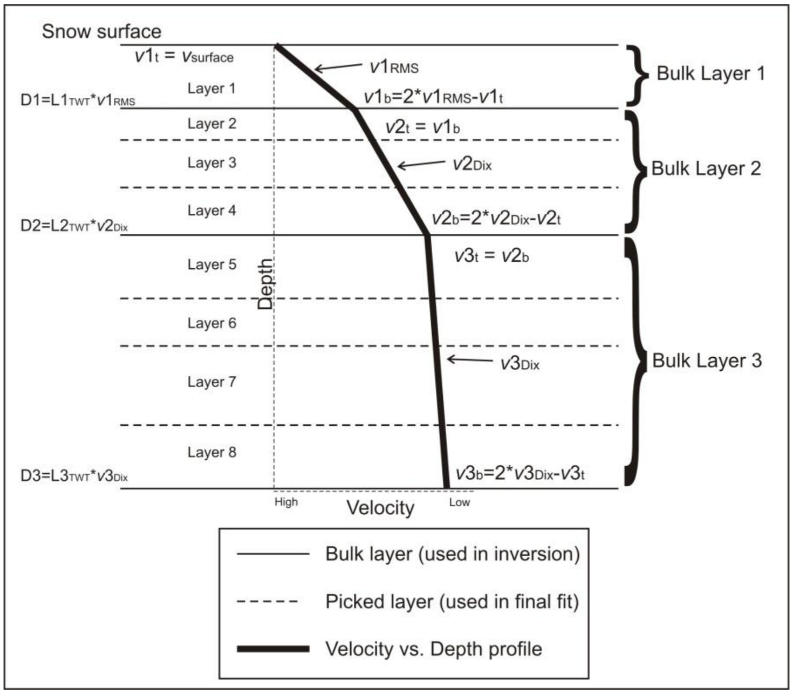

Figure 3.5 Schematic showing the model velocity vs. depth curve for the linear gradient inversion. The model includes multiple picked layers for each bulk velocity layer. How velocity and depths are determined is described in the appendix.

Here we define two categories of model layers: 1) ‘picked layers,’ for which we use models that include a layer for each picked moveout curve, and 2) ‘bulk layers’ for which we use models that combine picked layers into groups. We use the term ‘layers’ to describe generalities that apply to both picked layers and bulk layers. We ran our inversion on bulk layers, which combine multiple picked layers into a single layer. We then checked the quality of our fit to all of the picked layers (Figure 3.4).

We ran our inversion twice for each site, assuming different velocity profiles with depth. One set of inversions was run assuming EM propagation velocity decreases linearly with depth through a single bulk layer and that inflections in the velocity vs. depth curve occur at boundaries between bulk layers (Figure 3.5). Hereafter, we refer to this method as the ‘linear gradient inversion.’ A single linear velocity gradient across many picked layers is based on the assumption that the dominant densification processes follow the typical dry firn densification processes described in the Introduction. However, the relationship between radar propagation velocity and firn density (described in Section 2.4) is not linear. The error in calculated density values due to this non-linearity increases with depth to ~8% at 80 m. Because of this systematic error, we applied a second inversion in which we assumed that the subsurface can be modeled as a stack of constant velocity bulk layers (Figure 3.6). This inversion (hereafter called the ‘stepped velocity inversion’) assumed stepwise linear changes in density where the estimate is the mean density for the entire bulk layer.

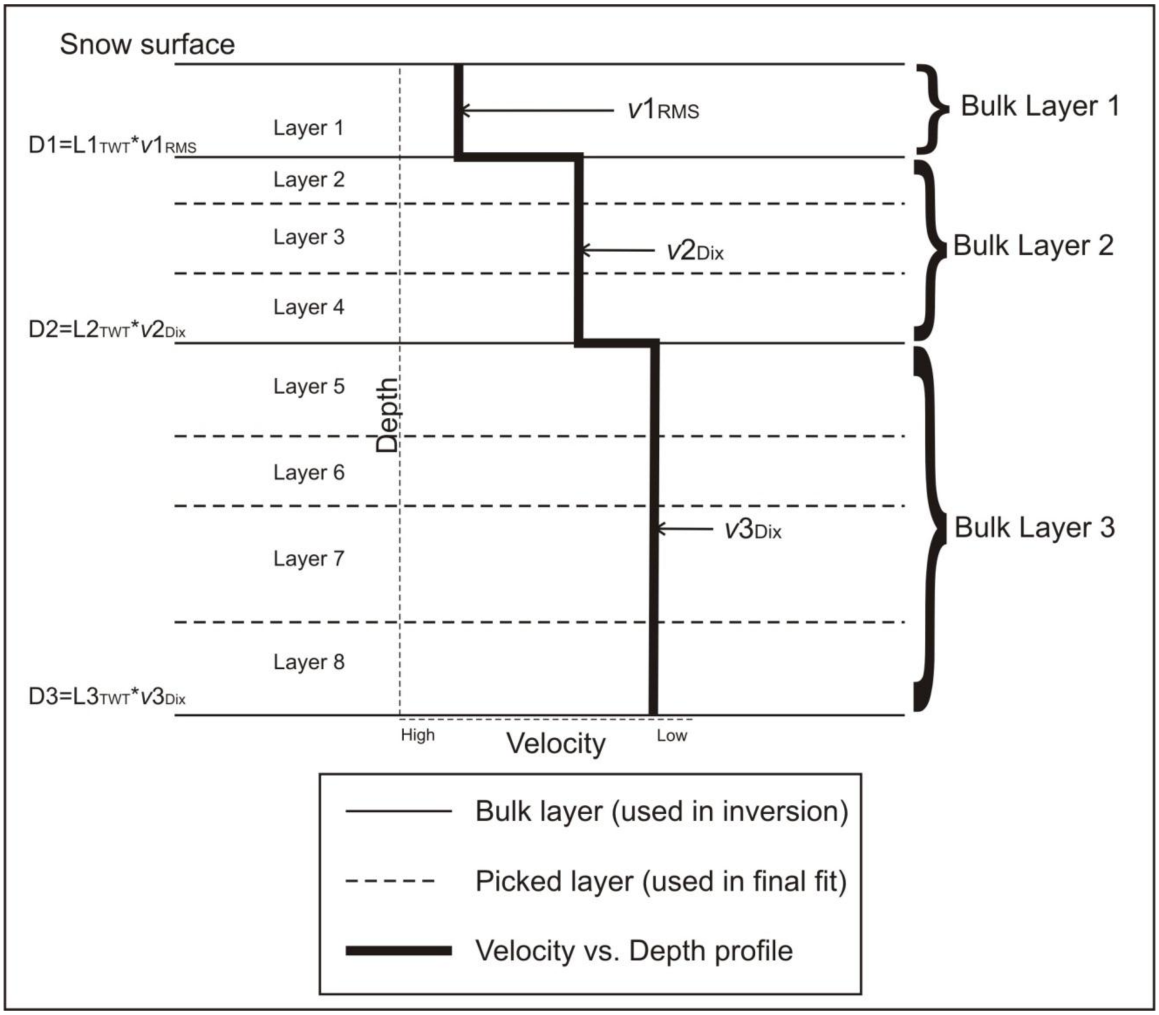

Figure 3.6 Schematic showing the model velocity vs. depth curve for the stepped velocity inversion. The model includes multiple picked layers for each bulk velocity layer. How velocity and depths are determined is described in the appendix.

Each inversion required a starting velocity model that we calculated directly from the CMP traveltime picks. We adjusted the profile of EM propagation velocity with depth systematically until rays traced through the model fit the traveltime picks to within a specified uncertainly threshold. We solved for one bulk layer boundary at a time, and for the velocity-depth profile from top to bottom, sometimes referred to as layer stripping. All shallower bulk layers must meet the fitting criteria before solving for the next bulk layer. This process resulted in a consistent inversion procedure that allowed us to compare depth-density curves between CMP sites. It is important to note that following the rules described in the appendix produces equally good fits to the data for either inversion procedure.

3.2.4 Density from Velocity

Within the ice/air/water/water vapor system that makes up the firn column, only ice, air, and water greatly influence the propagation velocity (v) of the radar pulses. Impurities account for a very small volume percentage and thus can be ignored when calculating propagation velocities in firn. Water, air, and ice have negligible conductivities, and magnetic permeabilities (μ) very close to that of free space (μ_o); they largely differ in relative dielectric permittivity (ε_r). The radar signal velocity is $v = \frac{c}{\sqrt{\varepsilon_r}}$ where c is the speed of light. As stated in the Introduction, we assume that the amount of liquid water at any given time in any given location is negligible. Thus, we assume that the firn is composed entirely of ice and air. This assumption is not always valid in the percolation zone. For example, if there is a large amount of melt before or during the georadar survey (such as occurred for T1, T2, and T3), the near surface layer(s) will have liquid water present. Even small volumetric water contents (less than 0.1) can change propagation velocities by more than 15% compared to dry snow of the same density [*Bradford et al.*, 2009].

When we can neglect effects of liquid water, we are left with a two-phase system where cold ice and air are the only contributors to bulk dielectric properties. The interaction of the radar signal with this mixture is affected both by the volumetric ratio of ice to air, as well as by the shape and orientation of the ice crystals and air voids. However, *Harper and Bradford* [2003] show that, for cold snow, the complex refractive index model (CRIM) equation [*Wharton et al.*, 1980; *Knight et al.*, 2004] can be adapted to closely estimate the bulk density of the mixture based on the velocity of the EM wave propagation. The adapted CRIM equation is:

$$\rho_f = \left(\frac{{v_a}/{v_f} - 1}{{v_a}/{v_i} - 1}\right)\rho_i \tag{1}$$

where ρ_f and ρ_i are the density of firn and ice respectively, and v_f, v_i, and v_a are the EM propagation velocities of firn, ice, and air respectively.

3.2.5 First-Order Density Model

We compared our estimated density profiles to hypothetical density profiles that assume no melt infiltration and refreeze. To do this, we calculated simplified depth vs. density curves using the empirically based model of *Herron and Langway* [1980] (the HL model), a first-order estimate of the density profile in dry conditions. By comparing our georadar derived densities to density profiles calculated with the HL model, we obtained a sense of how melt affects firn density through the entire firn column. The HL density curve depends on the initial snow density, the accumulation rate, and the 10 m firn temperature, which is an estimate of the mean annual temperature. We assumed that the 10 m firn temperature represents the mean annual air temperature at Crawford Point and therefore should be a reasonable average annual firn temperature. Under this assumption, we used the average surface temperature of -16.85 °C measured at Crawford Point

[*Fausto et al.*, 2009] and applied a temperature lapse rate of -7.4 °C per 1000 m [*Hanna et al.*, 2005] rise in elevation to calculate the relative 10 m core temperatures that are expected for the other sites. For the model accumulation rate at all locations, we used the average accumulation rate of 0.46 m of water equivalent measured at Crawford point [*Mosley-Thompson*, unpublished core data], which agrees well with previous measurements of accumulation at Crawford point [e.g., *McConnell et al*., 2000; *Bales et al.*, 2009]. Although the mass balance varies greatly over the length of our transect, the greatest part of this variation is due to summer melt. *Box et al.* [2004] show that over the span of our transect the accumulation varies by approximately 0.04 m water equivalent (~7.8%). For all locations, we assume an initial snow density of 375 kg/m^3 [*Braithwaite et al.*, 1994].

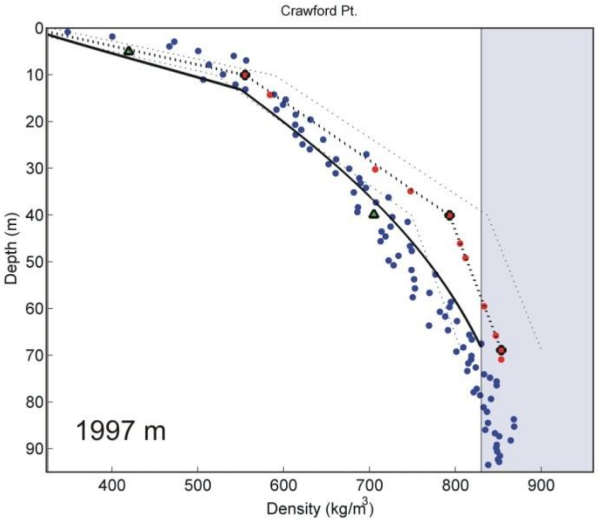

Figure 3.7 Georadar and core derived depth vs. density profiles for Crawford Point. The blue dots are the measured core density vs. depth values. The red dots connected by dashed black line are the linear gradient inversion. The red dots with black outline are the bulk layer solutions. The thin black dashed lines are the error bounds, which are based on a velocity range of ±0.002 m/ns for each modeled layer. The green triangles are the stepped velocity inversion. The solid black curve is the dry-snow density curve calculated with the HL model. The elevation of Crawford point is shown in the lower-left corner. The light blue region is considered ice (density ≥ 830 kg/m3). Georadar and core values were obtained within 1 km Crawford Point but are not from the exact same location.

3.3 Results

3.3.1 Accuracy of the Method

To validate the accuracy of our method, we compared the results of both inversions of georadar data collected at Crawford point to a 120 m core drilled in the same year within 1 km of our CMP (Figure 3.7). We identified 10 continuous reflections within the Crawford point radar data. The linear gradient inversion required three layers to achieve a good fit to all traveltime picks. The stepped velocity inversion required two layers. Because it represents layer average velocity, the stepped velocity inversion is best represented by two depth vs. density points plotted at the mean depth of the corresponding layer. The uncertainty range around both estimates lie within the core measurements acquired at Crawford Point (Figure 3.7).

We estimated the variability within the core data by fitting the core density vs. depth data with a second degree polynomial. The 2σ value of the residuals from the second degree polynomial fit to the data is ~48 kg/m^3. We also estimate the variability within the core data by fitting linear segments to the core density vs. depth data. We divided the data into three theoretical densification regimes: 1) less than 550 kg/m^3; 2) 550 kg/m^3 to 830 kg/m^3; and 3) above 830 kg/m^3. The 2σ value of the residuals from these fits is ~37 kg/m^3. We chose to compare our results to this second fit to the core data because the residuals are less than the second degree polynomial fit. The linear gradient inversion result is best represented by three segments that connect four depth vs. density points. If we assume that our inversion fits the velocity data within 0.002 m/ns (~1%-1.5% of the velocities measured), the associated density variation is between 26 kg/m^3 and 49.6 kg/m^3 for a density of 340 kg/m^3 and 917 kg/m^3, respectively. We assume this error because the associated density values are approximately equivalent to the natural variability in density found in the core. Using this range as error bounds for our inverted data, we find that the core data variability overlaps the error of the radar-derived data (Figure 3.7). Lastly, the HL model falls within the range of measured core densities.

3.3.2 Density vs. Depth Profiles along the EGIG

We determined linear gradient and stepped velocity models for all 13 locations between Crawford Point and H4 (Figures 3.7-3.10), along with the HL modeled density profiles (zero melt assumption). Both inversions show that the density increases with depth at a greater rate as elevation decreases. From Crawford point to H165, the curves generally follow the HL model (Figures 3.7-3.9b). The density vs. depth curves for H1 and H163 appear bimodal (Figure 3.9c,d). At both locations, our results show a low density layer less than 10 m thick overlying an ice layer that we identify at a depth of ~27 m and ~19 m for H1 and H163, respectively. As the transect continues through lower elevations, the density profiles continue to have higher densification rates until, at H4, there is a thin, low-density surface layer directly overlying ice (Figure 3.10).

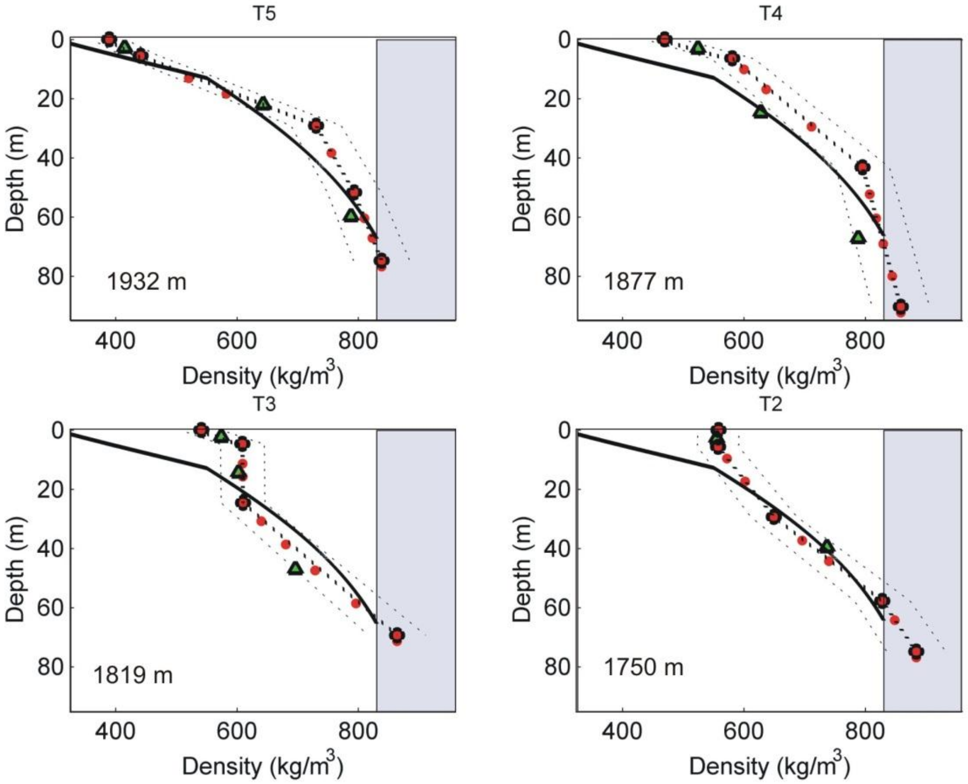

Figure 3.8 Georadar derived depth vs. density profiles for T5, T4, T3, and T2. The red dots connected by dashed black line are the linear gradient inversion. The red dots with black outline are the bulk layer solutions. The thin black dashed lines are the error bounds, which are based on a velocity range of ±0.002 m/ns for each modeled layer. The green triangles are the stepped velocity inversion. The solid black curves are dry-snow density curves for the HL model. The numbers in the lower-left corner are site elevations. The light blue region is considered ice (density ≥ 830 kg/m3). Note that it is likely that the surface layer densities for T3 and T2 are inaccurately high due to the presence of small amounts of liquid water near the surface.

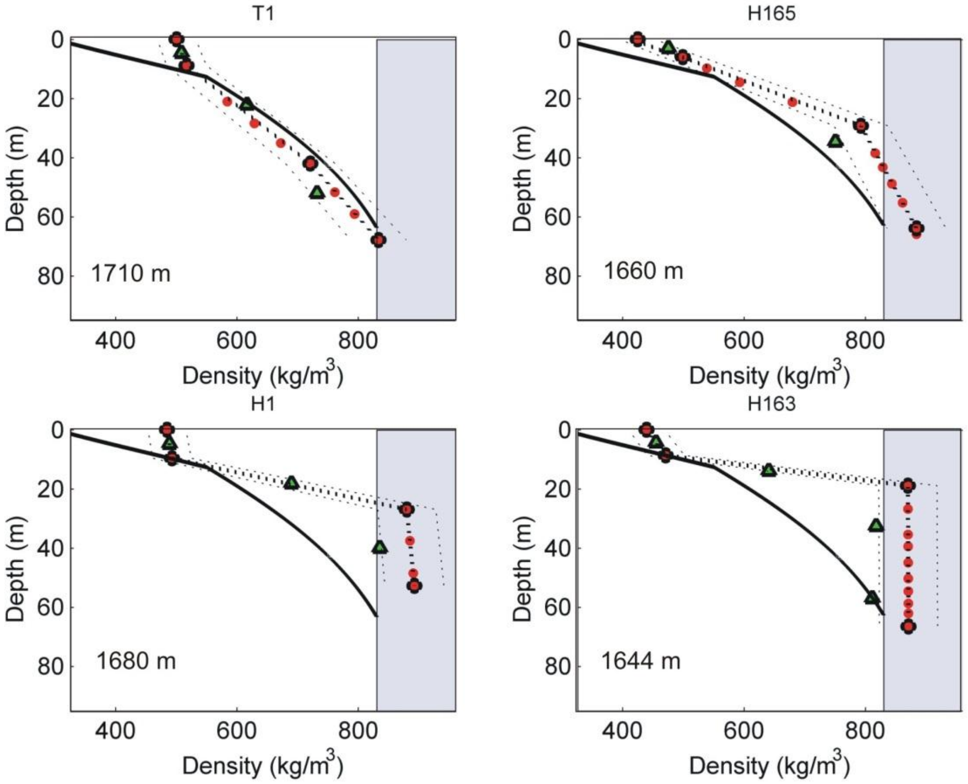

Figure 3.9 Georadar derived depth vs. density profiles for T1, H165, H1, and H163. The red dots connected by dashed black line are the linear gradient inversion. The red dots with black outline are the bulk layer solutions. The thin black dashed lines are the error bounds, which are based on a velocity range of ±0.002 m/ns for each modeled layer. The green triangles are the stepped velocity inversion. The solid black curves are dry-snow density curves for the HL model. The numbers in the lower-left corner are site elevations. The light blue region is considered ice (density ≥ 830 kg/m3). Note that it is likely that the surface layer density for T1 is inaccurately high due to the presence of small amounts of liquid water near the surface.

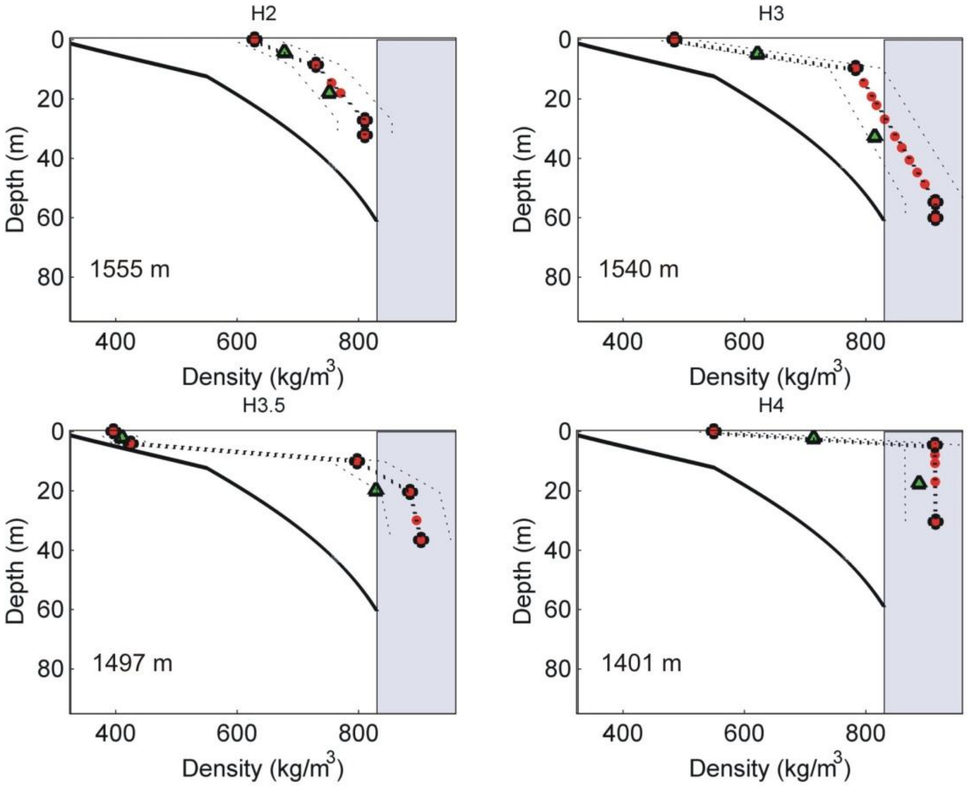

Figure 3.10 Georadar derived depth vs. density profiles for H2, H3, H3.5, and H4. The red dots connected by dashed black line are the linear gradient inversion. The red dots with black outline are the bulk layer solutions. The thin black dashed lines are the error bounds, which are based on a velocity range of ±0.002 m/ns for each modeled layer. The green triangles are the stepped velocity inversion. The solid black curves are dry-snow density curves for the HL model. The numbers in the lower-left corner are site elevations. The light blue region is considered ice (density ≥ 830 kg/m3).

We calculated the depth to the close-off density (830 kg/m^3) for our linear gradient profiles (Figure 3.11, diamonds) and for the HL modeled density curves (Figure 3.11, squares). We assume that the depth to close-off is the effective depth of the firn column. We also calculated the ice equivalent depth of the firn column for each location (Figure 3.11, triangles). The HL model close-off depths and the radar derived close-off depths are within 10 m for Crawford Point through T1. At H165, the close-off depth calculated from the HL model and the close-off depth calculated from our measurements start to diverge significantly; our measurements show close-off at ~43 m, whereas the HL model predicts close-off at 62 m. The sites between H1 and H4 all have close-off depths that are less than half the depth calculated with the dry conditions assumed in the HL model.

3.4 Discussion

3.4.1 Methods

Further justification for our departure from the standard semblance analysis/Dix inversion method of inverting for the velocity structure of the firn column is necessary. In the Introduction, we list two reasons that we chose not to use the common semblance analysis/Dix inversion method. The first is that the Dix inversion is subject to assumptions of NMO, whereas our method is not. The NMO assumptions of small offset to depth ratio and small vertical velocity gradients [*Bradford*, 2002] are violated in our surveys. The assumption of small offset to depth ratio is violated in the upper firn layers at all of our CMP sites. The assumption of small vertical velocity gradients is clearly violated at some of the lowest CMP sites, where densities increase by ~50% in less than 10 m depth (i.e., Figure 3.10 – H3.5). The second reason we chose not to use the common semblance analysis/Dix inversion method is that the Dix inversion is sensitive to small errors in velocity. Systematic errors in velocity measurements can occur by picking the semblance at the wave peak, which is especially true for shallow reflections. True velocity estimates come from the moveout of the first break of the wavelet, which do not produce a semblance response [*Murray et al.*, 2007]. This is because semblance is a measure of multi-offset coherence of wave phase, which is zero at the first break of the wavelet. Further, we do not have a direct physical comparison to determine the accuracy of our results for most of our CMP sites. Thus, we chose our inversion methods because they allow us to systematically solve for change in density with depth by using a consistent set of rules.

Our methods of inverting for radar velocities do not determine specific annual layer densities. Instead we either calculated average densities or density gradients through many annual layers. Within each inversion method, our procedure provided the simplest model that describes the observed traveltimes to within an accuracy threshold justified by the data. The scale of the measurement is much greater than the scale of ice lenses, ice pipes, and sastrugi, so that the average densification rate in depth is determined over a large area and corresponding firn volume. Determining the densification rate over a large area and through multiple annual layers gives a more general picture.

The two inversion methods that we describe in Sections 2.3.1 and 2.3.2 differ in the basic representation of the model subsurface. The stepped velocity model has an average velocity for each layer with a velocity step at each layer boundary. It is best represented by a single density vs. depth point for each layer, the depth of which is the average depth of the layer. Of the 13 sites, we fitted the CMP picks at 6 sites with a two-layer solution, a three-layer solution at 6 sites, and four-layer solution at only one site (Figure 3.9, H165). We show in Figure 3.7 that the inversion fits the core density at Crawford Point, although the two points that define the subsurface model do not show the shape of the densification curve. So, although the stepped velocity inversion is accurate, 12 of the 13 solutions define the density vs. depth curve with only two or three points.

The linear gradient model provides a continuous velocity curve with a velocity gradient change at each bulk layer boundary. Each picked layer within the bulk model layer defines a depth vs. density point along the curve. We fitted the CMP picks at three sites (H2, H3, and H4) with a two-layer solution (Figure 3.10), a three-layer solution at 7 sites, and a four-layer solution at 3 sites. The fit to the core data at Crawford Point is not as good for the linear gradient inversion as it is for the stepped velocity inversion, but the fit is within the estimated error of our inversion. Further, more than 80% of the depth vs. density points calculated with the stepped velocity model fall within the error estimate of the curve calculated with the linear gradient inversion.

The differences in the final velocity models indicate the inherent non-uniqueness in the problem and also indicate the uncertainty in the solution. We can compare the relative density profiles of all sites with no a priori knowledge of the subsurface because our inversions are consistent across all locations. However, the density with depth values calculated with the linear gradient inversion are valid at all of the picked layer depths, whereas the stepped velocity model represents only the mid-depth point of each bulk layer. Thus, although the two methods produce an equally good fit to the data, we used the linear gradient inversion to investigate changes in firn depth and depth vs. density curves across our study area.

As we stated in Section 3.1, the fit between the density profile derived from the linear gradient inversion and the core density profile at Crawford Point is not perfect. Inversion of the georadar data for density is not unique, thus we do not necessarily expect an exact match. In fact, by including more layers in our inversion, we could substantially improve the fit. However, we would risk biasing our inversion (manually adjusting the result to fit a preconceived density vs. depth curve) or over-fitting the data (fitting the noise in the data).

Although we do expect the first order shape of the georadar derived density profile to be similar to the core depth vs. density curve, we do not expect that our results will exactly match the core data for three reasons: 1) the data are not from the same exact location; 2) our method does not solve for exact densities of each layer but instead solves for the large scale densification trend over multiple years of accumulation; and 3) the core lengths for which density was measured and the CMP radar survey measure very different volumes. A nine centimeter diameter core sample ~ 1 m^3 within the upper 80 m of firn, whereas our data represent ~1500 m^3 of firn to 80 m at our maximum offset. This estimate assumes the zone of influence of the radar signal is ~0.5 m wide and that the radar signal travels the shortest distance path to 80 m depth at 80 m offset. In the upper regions of the percolation zone, the relatively large volume of firn measured by our methods resulted in a density profile that more likely represents the surrounding 1 km^2 than do individual cores, which can vary greatly over short distances [*Brown et al.*, 2011]. However, our method cannot resolve the short-scale density variability that is apparent in the core data.

It is important to acknowledge that the calculated densities for layers with liquid water present are inaccurate, which includes the surface layers for T1, T2, and T3. However, measurements of velocity in these upper layers are valid, thus they do not produce a measurement error that could propagate through the rest of the inversion. Instead errors introduced by liquid water content near the surface only influence the calculation of the density in the top layer, all other layer densities are accurate to the same error bounds as regions with no liquid water in the surface layer.

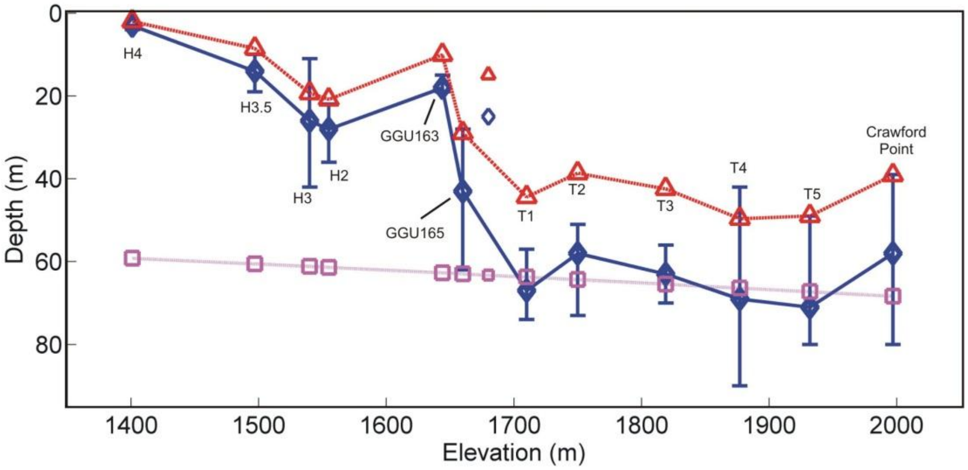

Figure 3.11 Depth to ice density (830 kg/m3) vs. elevation for all locations, as determined with georadar (blue diamonds) and calculated with HL model (pink squares). The ice equivalent depth is shown with red triangles. Error bounds for depth to 830 kg/m3 are the range encompassed by the error estimates shown in Figures 3.7-3.10 (dashed lines).

3.4.2 Density Profiles

Our radar-based calculations of pore close-off depth (830 kg/m^3) (Figure 3.11, diamonds) show a slowly diminishing depth to ice at 830 kg/m^3 as elevation decreases from Crawford point to T1, a sharper decrease in depth to 830 kg/m^3 between T1 and H163, and another region of slowly diminishing depth to 830 kg/m^3 as elevation decreases between H2 and H4. Our sites spanned about 600 m of elevation and encompassed areas with different amounts of melt (Figure 3.12). The density profiles are generated over multiple years by the combination of melt-induced densification and non melt-induced densification (including settling, sintering, and recrystallization). *Herron and Langway* [1980] argue that as firn becomes denser with time and burial, 'the proportional change in airspace is linearly related to change in stress due to the weight of overlying snow.' Although density with depth is influenced by melt at all locations along our transect, it is reasonable to conclude that overburden is the primary driver of densification where densification rates and depth to 830 kg/m^3 closely match the HL model. Conversely, where densification rates and depth to 830 kg/m^3 deviate greatly from the HL model, densification is primarily driven by a surface melt infiltration and subsequent refreeze.

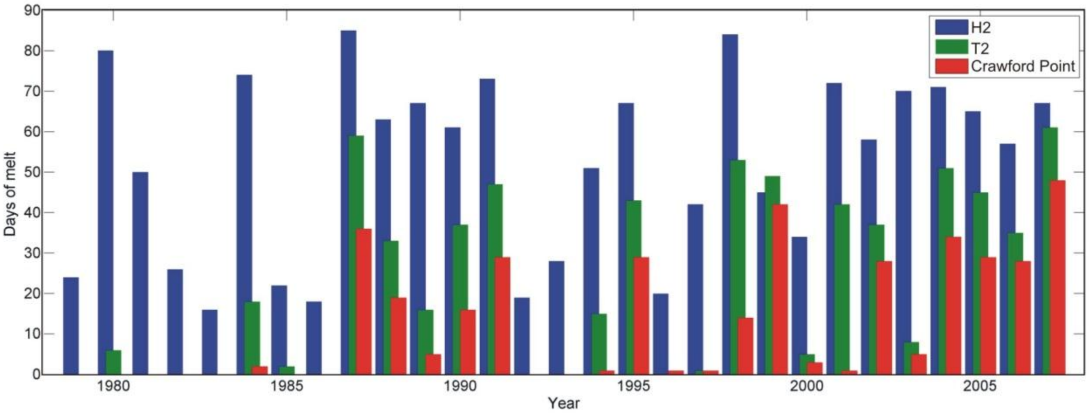

Figure 3.12 Melt days per year from 1979-2007 [Abdalati, 2007] for the areas around Crawford Point, T2, and H2.

Determining the primary driver of densification at each location allows us to assess the relationship between surface melt days, primary driver of densification, and firn density profiles, constrained by the coarse resolution of satellite-based melt day measurements. Near Crawford Point there were an average of 12.8 melt days per year with a range of 0–48 melt days per year between 1979 and 2007 (Figure 3.12) [*Abdalati*, 2007]. Near T2 melt increases to an average of 22.8 melt days per year with a range of 0-61 between 1979 and 2007. However, between Crawford Point and T1, the HL model closely approximates the calculated density vs. depth profile. Thus, in this region, surface melt infiltration/refreeze does not significantly affect firn density. Near H2 there is a consistently larger amount of melt days per year, with an average of 53.0 melt days per year with a range of 16–85 between 1979 and 2007 [*Abdalati*, 2007] (Figure 3.12). From H2 to H4, the density vs. depth profiles deviate greatly from the HL model (Figure 3.10) and depths to 830 kg/m^3 are ~50% of that predicted by the HL model (Figure 3.11). In this region surface melt, infiltration, and refreezing dominate the densification process. The sharp decrease in depth to 830 kg/m^3 between T1 and H163 reveals a relatively small transition zone between areas where firn densification is dominated by overburden and areas where firn densification is dominated by melt processes. The short distance (and corresponding elevation range) between areas may indicate that the system is sensitive to small changes in surface melt rates, and therefore small changes in temperature.

3.5 Conclusions

Our methods of inverting for firn density from georadar data result in density vs. depth curves in firn. Our inversions for density at Crawford Point agree with core data within estimated uncertainty. Further, because there is little user bias to our inversions, it is possible to compare the resultant density vs. depth profiles from multiple sites to each other. Where even small amounts of liquid water are present in the firn column, the density calculation is inaccurate. However, because the velocity inversion is layer-based and gives accurate average velocities for each layer, inaccuracies due to liquid water at or near the surface do not propagate through the inversion.

From Crawford Point to T1 (1997 m to 1710 m above sea level), overall densification processes are not greatly affected by surface melt infiltration/refreeze; overburden is the primary driver of densification. From H2 through H4 (1555 m to 1401 m above sea level), surface melt is the primary driver of densification. The boundary between these regions spans ~60 m of elevation and 8 km in distance. This small boundary region suggests that the balance between overburden driven firn densification and melt driven densification may be sensitive to small changes in melt. This could greatly influence changes in surface elevation of the GrIS in a changing climate.

3.6 Appendix

3.6.1 Inversion Setup and Rules

In the following sections, we describe our model setup and inversion rules. Here v is velocity, TWT is two-way traveltime, the subscripts t and b refer to the top and bottom of a layer, respectively, and the letter N refers to the layer number (i.e., N=3 for the third layer). TWT_{RMS} is the RMS error of the fit between the ray trace model moveout curves and the picked moveout curves. The subscripts NMO and DIX are used to distinguish between velocities calculated from NMO measurements and velocities calculated using the Dix equation. We calculated stacking velocities for our starting models by linearly fitting the traveltime vs. offset picks in the time-squared vs. distance-squared domain; thus, the stacking velocities are NMO approximations. We also calculated the standard deviation of the data to the NMO fit, which we used to determine if our inversion was a ‘good’ fit. For each horizon, we limited our fit to offsets where the traveltime vs. offset picks do not merge with the direct subsurface wave.

3.6.2 Linear Gradient Velocity Model Inversion

We used six steps to form the linear gradient starting model:

(1) The velocity at the surface ($v1_t$) is the direct subsurface wave velocity (Figure 3.3b).

(2) Assume v_{NMO} of the surface layer ($v1_{NMO}$) is the average velocity of that layer. The velocity at the base of that layer is then defined as $v1_b = 2v1_{NMO} - v1_t$ (Figure 3.5).

(3) Set the velocity at the top of the second layer ($v2_t$) equal to $v1_b$.

(4) Let the Dix velocity of the second layer ($v2_{DIX}$) represent the average velocity of that layer. The velocity at the bottom of the second layer is then $v2_b = 2v2_{DIX} - v2_t$.

(5) Similarly, define all subsequent layers by setting $vN_t = v(N\text{-}1)_b$ and $vN_b = 2vN_{DIX} - vN_t$ where N is the layer number.

(6) Calculate the depth to each bulk layer boundary using the TWT for the near offset trace and the v_{NMO} for the bulk layer(s).

We used six steps in the linear gradient inversion:

(1) Start with simplest (2 layer) model. The surface picked layer is the top bulk layer (N=1). All other picked layers are combined into one layer (N=2).

(2) Invert for each bulk layer separately from top to bottom, starting with the second bulk layer.

(3) Iteratively solve for depth and velocity of each bulk layer separately, keeping the top velocity equal to the velocity at the base of the previous bulk layer.

(4) Iterate until the residual RMS traveltime between the modeled traveltime vs. offset curve and the picked curves for all bulk layers is within 1 standard deviation of the NMO fit to bulk layers.

(5) If the residual RMS traveltime between the modeled traveltime vs. offset curve and the picked curves for all picked layers is within 2 standard deviations of the NMO fit to the picked layers, then no further changes in the model are justified and inversion is stopped.

(6) If the fit to the picked layers is greater than 2 standard deviations of the NMO fit to the picked layers, then increase the number of bulk layers by one, holding the top bulk layer (N=1) constant, and redo inversion. For example, a model with three bulk layers would consist of the surface picked layer being the top bulk layer (N=1) and all other picked layers combined into two layers (N=2 and N=3). The location of the new layer boundary is where the modeled TWT curves deviate from the picked layers.

3.6.3 Stepped Velocity Model

We used three steps to form the stepped velocity starting model:

(1) Assume v_{NMO} of the surface layer ($v1_{NMO}$) is the average velocity of that layer. Thus, $v1= v1_{NMO}$.

(2) Assume the initial velocity for other bulk layers is v_{DIX} for those bulk layers (Figure 3.6).

(3) Calculate the depth to each bulk layer boundary using the TWT for the near offset trace and the v_{NMO} for the bulk layer(s).

We used six steps in the stepped velocity inversion:

(1) Start with simplest (2 layer) model where the surface picked layer is the top bulk layer (N=1) and all other picked layers are combined into one layer (N=2).

(2) Invert for each bulk layer separately from top to bottom, starting with the second bulk layer.

(3) Solve for depth and velocity of each layer together.

(4) Iterate until the residual RMS traveltime between the modeled traveltime vs. offset curve and the picked curves for all bulk layers is within 1 standard deviation of the NMO fit to bulk layers.

(5) If the residual RMS traveltime between the modeled traveltime vs. offset curve and the picked curves for all picked layers is within 2 standard deviations of the NMO fit to the picked layers, then no further changes in the model are justified and inversion is stopped.

(6) If the fit to the picked layers is greater than 2 standard deviations of the NMO fit to the picked layers, then increase the number of bulk layers by one, holding the top bulk layer (N=1) constant, and redo inversion. For example, a model with

three bulk layers would consist of the surface picked layer being the top bulk layer (N=1) and all other picked layers combined into two layers (N=2 and N=3). The location of the new layer boundary is where the modeled TWT curves deviate from the picked layers.

3.7 Acknowledgements

This work was funded by US National Science Foundation grant OPP-ANS #0612506. We would like to thank Steve Arcone, Huw Horgan, and an anonymous reviewer for their insightful and thorough comments that greatly improved this manuscript. We would also like to thank David Schuler and Daniel Sturgis for helping collect radar data.

Table 3.1 Site locations, depth to 830 kg/m^3, date of data collection, and temperature data for day of data collection[1]

Site Name	Latitude	Longitude	Elevation (m)	Depth to 830 (m)	Date of data collection	Ave temperature on date of data collection (Deg. C)
Crawford Point	69.87650	47.01020	1997	58	26-Jun-07	0
T5	69.84802	47.27358	1932	71	7-Jul-07	-0.3
T4	69.81998	47.45050	1877	69	3-Jul-07	-2.9
T3	69.78360	47.67018	1819	63	3-Jul-07	-2.5
T2	69.75693	47.88028	1750	58	28-Jun-07	0.5
T1	69.73802	48.06097	1710	67	28-Jun-07	0.8
H165	69.72505	48.19020	1660	43	21-May-08	-19.0
H1	69.73908	48.24030	1680	25	16-May-08	-10.9
H163	69.71978	48.26740	1644	18	22-May-08	-14.8
H2	69.70617	48.34497	1555	28	31-May-08	-9.3
H3	69.68743	48.49967	1540	26	18-May-08	-7.6
H3.5	69.67393	48.59112	1497	14	31-May-08	-8.9
H4	69.66018	48.68945	1401	3	22-May-08	-13.0

---

[1] The temperature data are an average of air temperature readings from four instruments at Crawford Point, which are part of the Greenland Climate Network [*Steffen et al.*, 1996]. The average air temperature is the mean value of the readings for the full diurnal cycle during the day of data collection at Crawford Point with a temperature lapse rate of -7.4 °C per 1000 m rise in elevation [*Hanna et al.*, 2005].

CHAPTER FOUR: EM PROPAGATION VELOCITY STRUCTURE OF SEASONAL SNOWPACK FROM DECONVOLUTION OF GPR DATA

EM propagation velocity structure of seasonal snowpack from deconvolution of GPR data

Joel Brown [1]

John Bradford [1]

For Publication in:

Cold regions Science and Technology

November 2011

[1] *Center for Geophysical Investigation of the Shallow Subsurface, Boise State University*

Abstract

Common offset ground penetrating radar surveys are often used to map variations in extent and relative depth of near-surface geologic boundaries. However, without independent measurements of depth or propagation velocity, determining absolute depth to near-surface geologic boundaries is not possible. Here, we use deconvolution of common offset ground penetrating radar surveys to calculate the dielectric permittivity structure of three seasonal snowpacks in the mountains of Western Montana, USA. The permittivity structure is directly related to the velocity structure of snowpacks. Our method employs collecting data with antennas suspended above the ground or snow and deconvolving the data with a wavelet measured from a reflection off of a perfectly reflecting surface. We compare our calculated permittivities to permittivities measured with a Finnish Snow Fork in snow pits dug to the ground along each transect. The calculated permittivities are similar to measured values at all five snow pit locations and differences are less than 13% of the snow fork measured values over the depth of the snowpack at all pit locations. This method of calculating the dielectric permittivity structure of a seasonal snowpack could easily be employed to accurately estimate the snow water equivalent of snowpacks over large areas and would allow density profiles to be measured quickly for constraining microwave remote sensing retrieval algorithms.

4.1 Introduction

Common offset ground penetrating radar (GPR) reflection surveys are commonly used in near-surface geophysics applications. Specifically, common offset GPR is used to identify and track boundaries between subsurface layers that have different bulk electrical properties. Since the measurement is in traveltime, either the depth to a reflecting boundary or the average electromagnetic (EM) propagation velocity (v_{ave}) above a reflecting boundary must be determined to solve for the other parameter. More measurements in addition to common offset georadar surveys are needed to either measure depth or v_{ave} to the target layer boundary. Depth to a reflecting boundary can be measured manually by digging or drilling through the layers, followed by correlating layer boundaries to horizons identified in the common offset radar image. Average EM propagation velocity to a reflection horizon can be measured by a single common midpoint (CMP) gather [*e.g.*, *Gudmandsen*, 1971], cross-borehole measurements [*e.g.*, *Clement and Barrash*, 2006], or vertical radar profiles (VRPs) [*e.g.*, *Clement and Knoll*, 2006]. Physical logging of borehole properties can also reveal the subsurface structure, including electrical properties. All of these measurements are valid for the point at which they are acquired, and with an assumption of lateral homogeneity we can extrapolate away from the point measurement. However, if lateral variation in the EM propagation velocity is present, we need spatially dense measurements of the velocity field to accurately represent the subsurface. It is often not feasible to acquire spatially dense data with conventional measurements such as snow pits or CMPs.

Multi-fold GPR surveys effectively result in a series of CMP measurements across a transect [e.g., *Fisher et al.*, 1992; *Liberty and Pelton*, 1994; *Pipan et al.*, 1996]. Reflection tomography can be used to invert multi-fold GPR data to measure the lateral velocity structure of the subsurface [e.g., *Bradford*, 2006; *Brown et al.*, 2009]. These velocity variations can be linked to variations in propagation material, in porosity, and in water content. Conducting a multi-fold GPR survey requires either a multi-channel GPR system or a multi-pass survey design with a single channel system. It is desirable to be able to measure lateral variations in subsurface velocity structure with common-offset GPR surveys, which are less time-intensive than multi-pass surveys, and multi-channel systems are often cost-prohibitive.

The EM propagation velocity of a snowpack is related to the density and wetness of the snowpack [*e.g.*, *Sihvola and Tiuri*, 1986]. More specifically, the propagation velocity is related to an average complex dielectric permittivity comprised of the constituent permittivities from the mixture of ice, air, liquid water, water vapor, and impurities within the snowpack. Previous studies have used impulse radar systems [*e.g.*, *Lundberg et al.*, 2000] or Frequency Modulated Continuous Wave radar systems [*e.g.*, *Marshall et al.*, 2005] to accurately estimate the snow water equivalent (SWE) of dry snowpacks. These estimates of SWE are derived from measurements of radar two-way traveltime and separate manual measurements of depth or density of the snowpack to calculate the average propagation velocity through the snowpack. Although the relationship between SWE and propagation velocity is complicated by even small amounts of liquid water, recent work using frequency-dependent attenuation analysis of georadar [*Bradford et al.*, 2009] has shown that wetness and density of the snowpack can be solved for simultaneously if accurate propagation velocity estimates for the snowpack are available.

In petrophysical seismic surveys, convolution of an input waveform with a discrete reflectivity series constructed from well log data commonly used to characterize reservoirs [*e.g.*, *Latimer et al.*, 2000]. Similarly, georadar traces can be modeled as a convolution of a source wavelet with a reflectivity series to approximate the subsurface impulse response. For example, *Kohler et al.* [2003] reconstructed a reflectivity series of snow and firn from electrical measurements made on a snow/firn core extracted from Svalbard, Norway. They then convolved a waveform with the reflectivity series and compared their results to georadar data acquired near the core location. They found a reasonable correlation between the modeled and recorded data.

Here we use deconvolution to solve for the short wavelength reflectivity structure of seasonal snowpacks. We then use this reflectivity structure to estimate the dielectric permittivity (ε) profile of the snowpack. We deconvolve georadar traces from three separate locations with varying layer structures. We compare our results to permittivity measurements made with a Finnish snow fork [*Sihvola and Tiuri*, 1986]. Our findings show that in these three cases, the deconvolution method is comparable to the snow fork measurements. With these promising results, we suggest that the method has significant potential to make accurate, laterally continuous measurements of seasonal snowpack properties using existing commercial georadar systems.

4.2 Theory

The convolutional model assumes: 1) that the subsurface is composed of horizontal layers with constant impedance, 2) the GPR signal is a plane wave that propagates through the horizontal layers at normal incidence, and 3) the propagating medium is non-dispersive. In most real-world applications, all of these assumptions are violated to some extent. The degree to which these assumptions are violated will affect the validity of the model. As we explain below and in Sections 4.3 and 4.5, by collecting data in seasonal snowpacks with antennas raised off of the snow surface, we greatly limit the extent to which we violate these three assumptions. The convolutional model also does not address multiples or long wavelength changes in impedance. Herein, we assume that the seasonal snowpacks in which we collected our data had an approximately 1-D structure with density changes separated by discrete boundaries over the area of the Fresnel zone of the GPR signal.

In the convolutional model, each GPR trace in time ($g(t)$) is the convolution of the source waveform ($w(t)$) and a 1-D reflectivity series in time ($r(t)$), plus a noise component ($n(t)$) [e.g., *Russel*, 2009; *Annon*, 2005; *Snieder*, 2001; *Yilmaz*, 2001].

$$g(t) = \big(w(t) * r(t)\big) + n(t) \qquad (2)$$

Equation (2) is indeterminate because w, r, and n are all unknowns. However, if we assume that the noise component is either negligible or that we can filter out all non-negligible components of the noise, then we may take the Fourier transform of Equation (2) giving us an equation in the frequency domain. Convolution becomes multiplication in the frequency domain, therefore deconvolution is simple division in the frequency domain:

$$R(f) = \frac{G(f)}{W(f)} \quad . \tag{3}$$

Here *G(f)*, *W(f)*, and *R(f)* are the Fourier transforms of *g(t)*, *w(t)*, and *r(t)*, respectively. Obviously, this only works where *W(f)* is non-zero within the frequency range of interest. If *W(f)* is zero within the frequency range of interest, we can use an alternative equation [*Claerbout*, 1992]:

$$R(f) = \frac{G(f)\overline{W(f)}}{W(f)\overline{W(f)}+\alpha^2} \tag{3)*}$$

Where $\overline{W(f)}$ is the complex conjugate of *W(f)* and α is a damping factor which is discussed in *Claerbout* [1992]. In this study, *W(f)* is non-zero within our frequency range of interest allowing us to use Equation (3) in our inversion. Thus, if we can accurately estimate *w(t)*, we can easily solve for *R*(*f*).

The reflection coefficient across a boundary between layer 1 and 2 is defined as:

$$R = \frac{Z_2 - Z_1}{Z_2 + Z_1}. \tag{4}$$

Where *Z* is the complex electrical impedance and is defined as:

$$Z = \sqrt{\frac{\mu}{\varepsilon}}\left(1 + \frac{\sigma}{i\omega\varepsilon}\right)^{-1/2} \tag{5}$$

Where μ is the magnetic permeability, ε is the dielectric permittivity, and σ is the conductivity of a propagating medium. Usually seasonal snowpacks have negligible conductivity and magnetic permeability approximately equal to that of free space (μ_0). With these approximations, Equation (4) simplifies to:

$$Z = \sqrt{\frac{\mu}{\varepsilon}}. \tag{6}$$

Substituting (5) into (3) and solving for the dielectric permittivity of the second propagating medium, we get:

$$\varepsilon_2 = \varepsilon_1 \frac{(1-R)^2}{(1+R)^2}. \tag{7}$$

Thus, if we know the permittivity of the first propagating medium as well as the reflectivity series, we can solve for the short wavelength dielectric permittivity structure recursively from top to bottom.

We measure the source waveform of the system by recording the reflection from a metal plate with the GPR antennas suspended above the ground [e.g. *Huisman et al.*, 2003]. If the antennas are suspended far enough from the reflecting body to allow us to neglect near-field effects, it is reasonable to assume that this measured waveform accurately estimates *w*(t) with amplitude loss and noise added. If we also collect our data with the antennas suspended the same height above the ground as our waveform measurement, the measured *w*(t) is the source function needed to deconvolve the data. Further, in this acquisition geometry, we know the dielectric permittivity of the first layer (air), which allows us to use Equation (7) to solve for the permittivity structure of the subsurface at each trace location. We then use a layer stripping approach to solve for all subsequent layers. With this approach, errors are cumulative from the top of the snow pack to the bottom.

4.3 Data Collection

We conducted georadar surveys at three locations in the mountains of western Montana and northern Idaho (Figure 4.1). The snowpacks at the three locations had varying depth, wetness, density, and internal structure. The data include a dry snowpack with no melt, a dry snowpack with evidence of melt induced layering, and a slightly wet snowpack where melt was occurring during data collection. We used a Pulse EKKO Pro GPR system with 1000 MHz shielded antennas recording a sample every 0.1 ns. We suspended the antennae 0.7 m above the snow surface on a PVC framework built onto a sled (Figure 4.2). We suspend the antenna above the snow surface for three reasons: 1) it allows ringing from the airwave to dissipate before the first reflection off of the snow surface is received, 2) it avoids coupling effects so we have a consistent source waveform, and 3) we know the electrical properties of the initial propagating medium (air).

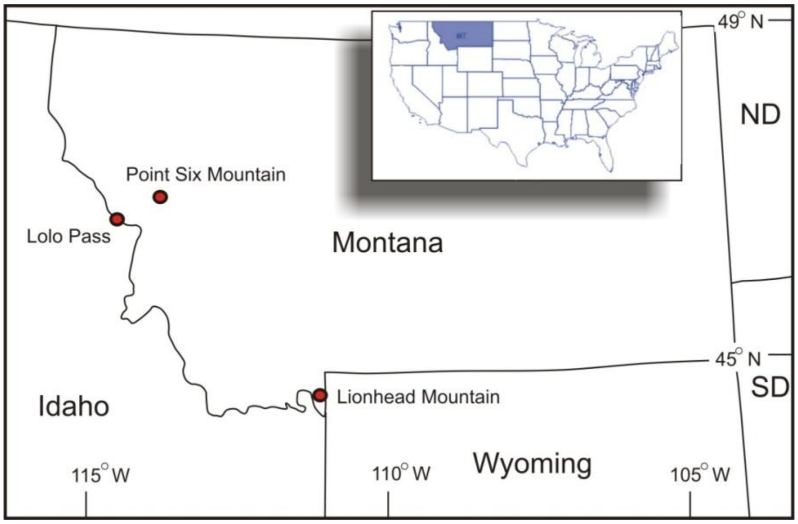

Figure 4.1 Map of Montana showing locations of field sites.

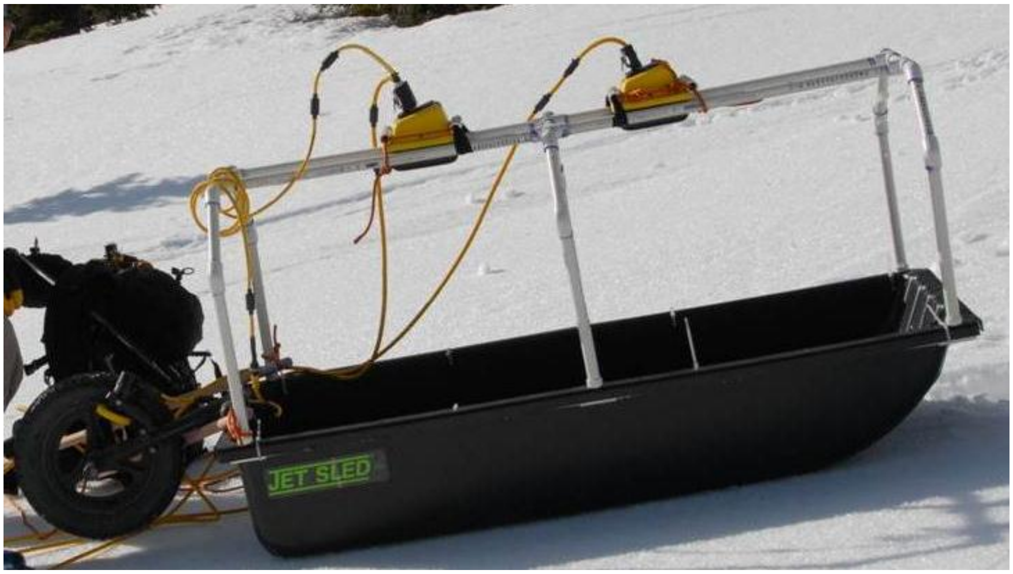

Figure 4.2 Photograph showing sled with radar. GPR antenna are suspended 0.7 m above the snow surface on a PVC framework attached to a sled.

The distance at which dipole radiation patterns measured in water converge to the far-field solution pattern ranges from ~8.1 wavelengths (λ) [*Smith*, 1984] to more than 30 wavelengths [*Wensink et al.*, 1990]. Simulated radiation patterns reveal incomplete convergence to the far-field approximation at 40 λ [*Valle et al.*, 2001] but a reasonable approximation of the far-field occurs at ~10 λ [*Radzevicius et al.*, 2003]. Our antenna height results in a ~2.33 λ separation between the antenna and the snow surface, which is clearly not within the far-field. For larger antennas, loose definitions of the near-field range from 1λ to $r < {}^{L^2}/_{\lambda}$ [*Ulaby et al.*, 1981] and $r < {}^{2L^2}/_{\lambda}$ [*Balanis*, 2008], where r is radial distance and *L* is the antenna length. For our setup, the results in estimates of the near-field are ~0.3 m, ~0.03 m, and 0.06 m calculated with the equations respectively. Thus, our data are likely collected within the transition zone between near-field and far-field. However, our data and source wavelet are both collected without direct coupling to the ground, thus near-field differences in waveform between the data and source wavelet are limited.

4.3.1 Picking the Source Wavelet

As shown in Equation (2), an accurate estimate of the source wavelet is required for deconvolution. To make this estimate, we measured the source wavelet by acquiring traces with the antennae 0.7 m above the center of a reflecting boundary made by connecting six steel plates ~0.61 m x ~0.91 m with conductive tape, creating a conductive boundary ~1.83 m x ~1.83 m. The recorded trace consists of antenna-to-antenna ringing, the recorded wavelet from the conductive boundary, and random and coherent noise. We compensate for the low frequency noise component with a dewow filter, which removes the DC bias and subsequent low frequency noise. We compensate for the 3-D geometrical spreading of the wavelet with a gain correction proportional to $1/vr$, where v is velocity and r is the distance from the antenna reflecting surface. To reduce the random noise component of the waveform, we stack 2081 independent wavelet recordings. The primary reflection from the plate is apparent in Figure 4.3a (shaded region). Picking the correct wavelet from the reflected waveform is important to the accuracy of the deconvolution solution. In order to use the recorded wavelet in deconvolution, we create a waveform with the component of the trace that is the reflection of the source wavelet added to the beginning of a null vector that is the length of the recorded trace (Figure 4.3b). In order to isolate the component of the recorded wavelet that is due to the reflection off of the metal plate, we limit our source waveform to the portion of the recorded wavelet with amplitudes greater than 5 times the amplitude of the coherent noise of the multiple recorded between 9 ns and 13 ns in the waveform (Figure 4.3a). This cutoff is empirically derived through trial and error. We used identical filtering processes for our field data as we used to determine the source waveform.

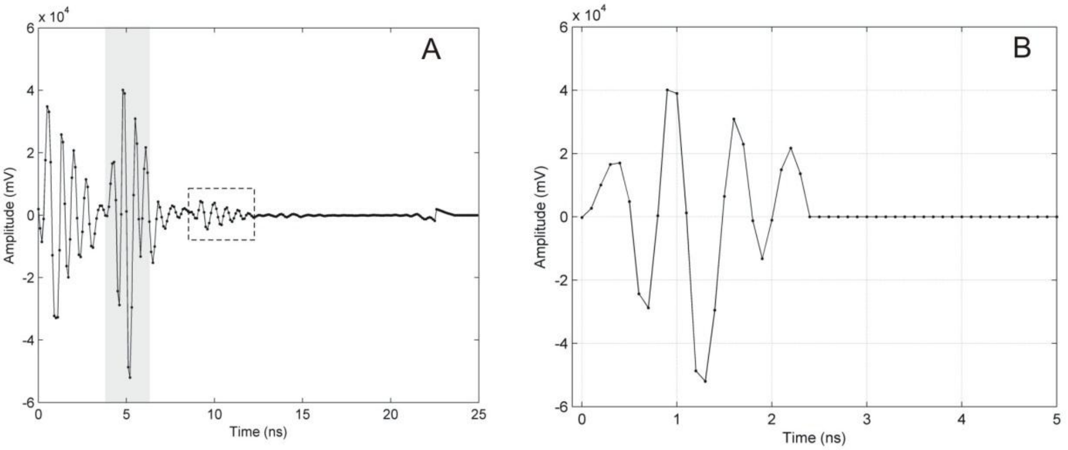

Figure 4.3 (A) Waveform showing reflected signal off of a perfectly reflecting surface. The waveform is the mean of 2081 individual traces with a dewow filter to reduce low frequency coherent noise and a spherical spreading gain function to account for amplitude loss. The shaded region is the wavelet picked to construct the waveform used in deconvolution (B). The region boxed by the dotted line is a coherent multiple.

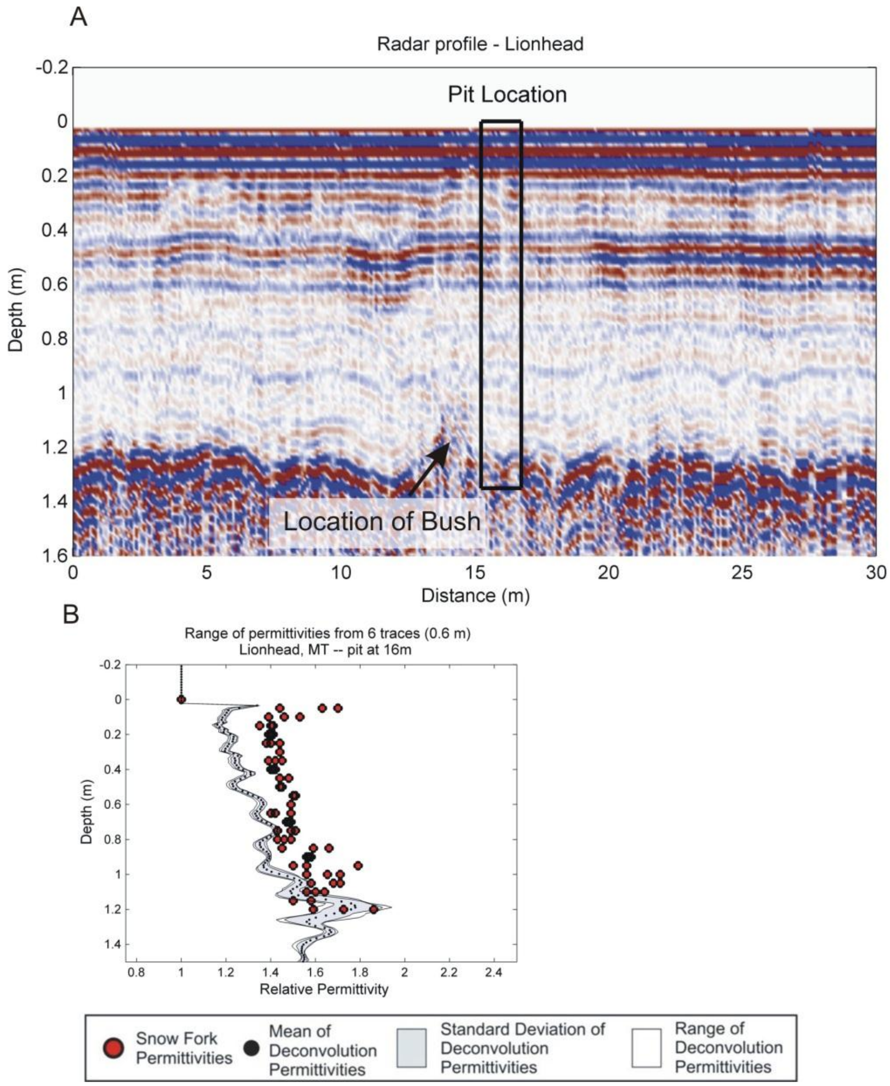

Figure 4.4 (A) Common offset radar image from the Lionhead Mountain snow survey site. The location if the pit is shown with a black box. The location of a bush uncovered during excavation of the pit is shown. (B) Relative permittivity structure of the snowpack at the Lionhead Mountain snow survey site. The deconvolution solution is denoted by small black dots connected by a solid line. The mean real part of the permittivities measured with the Finnish Snow Fork are shown with a red filled dot, the red error bars on these points show the range of measured permittivities across the pit wall.

4.3.2 Lionhead Mountain – Wet Snowpack

In March of 2007, we collected a 30 m GPR profile on undisturbed snow near Lionhead Mountain, about 15 km west of West Yellowstone, Montana (Figure 4.1). The site is located on a 25–30 degree northwest facing slope in an open glade at ~2350 m elevation. We measured the depth of snowpack and the dielectric permittivity vs. depth profile of the snowpack in a snowpit located near the center of the GPR profile (Figure 4.4A). The measured snowpit depth was ~1.2 m with an average wetness of 1.55% wetness by volume as measured with the snow fork. On the South edge of the pit, we uncovered a bush, which can be seen in the radar profile (Figure 4.4A). In the pit, we collected three vertical dielectric permittivity profiles with the Finnish snow fork, two on 0.05 m intervals and one on 0.1 m intervals. We used an odometer wheel to collect a GPR trace approximately every 0.1 m.

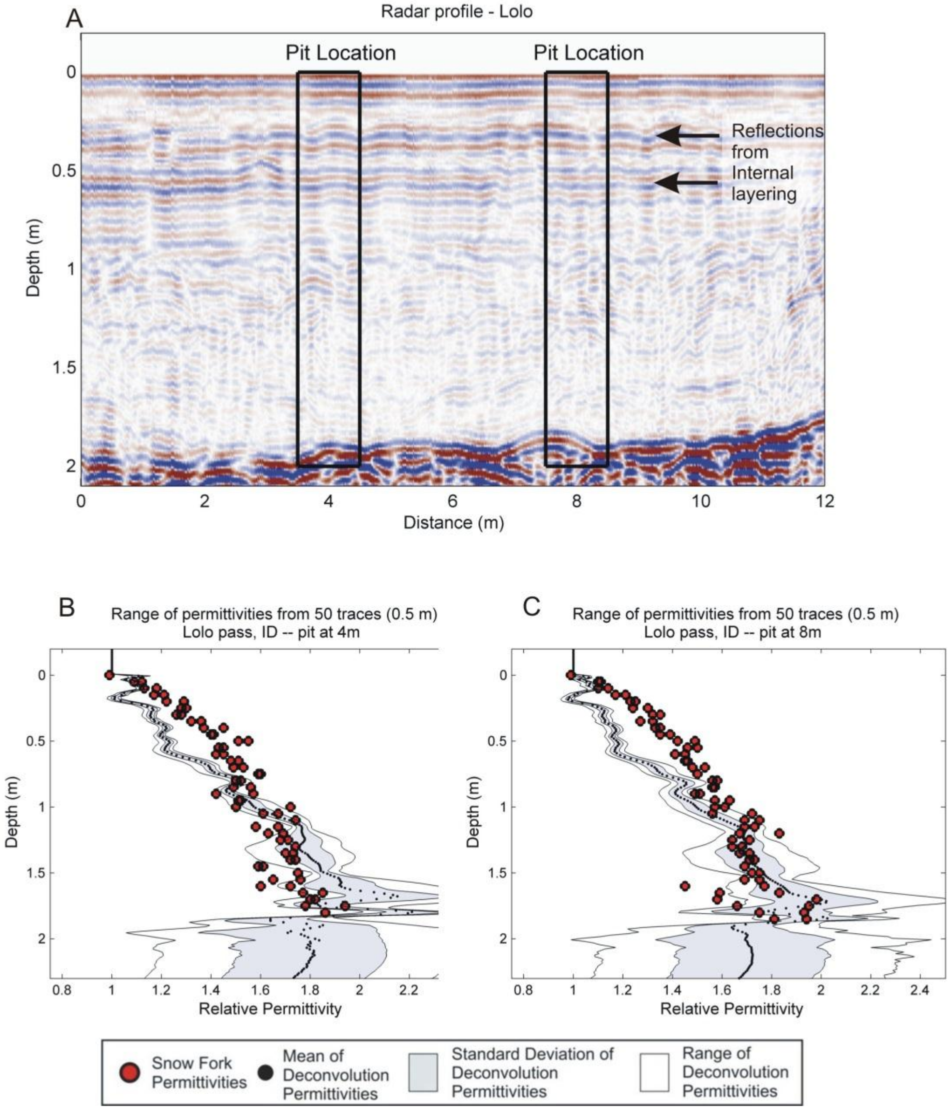

Figure 4.5 (A) Common offset radar image from the Lolo Pass site. The location if the pits are shown with a black box. Strong reflections from high density layers are marked with arrows (B and C). Relative permittivity structure of the snowpack at the pit located at 4 m (B) and 8 m (C) along the transect at the Lolo Pass survey site. The deconvolution solution is denoted by small black dots connected by a solid line. The mean real part of the permittivities measured with the Finnish Snow Fork are shown with a red filled dot, the red error bars on these points show the range of measured permittivities across the pit wall.

4.3.3 Lolo Pass – Snowpack with Melt Induced Layering

In February of 2011, we collected a 12 m GPR profile on an undisturbed snowpack in a small glade on Lolo Pass, near the Montana – Idaho border (Figure 4.1). We collected the profile on a slight slope (less than 5 degrees) with a western aspect at an elevation of ~1597 m. We measured the depth of snowpack, the density vs. depth profile of the snowpack, and the dielectric permittivity vs. depth profile of the snowpack in two snowpits, one located at the 4 m mark of the profile and one located at the 8 m mark profile (Figure 4.5A). The depth of the snowpack was ~1.95 m, rain and large melt events throughout the winter created ice layers and a dense snowpack (Figure 4.5A). Approximately 0.12 m of new snow had accumulated the night before our survey. In each pit, we collected two vertical permittivity profiles on 0.05 m intervals. We used an odometer wheel to collect a GPR trace approximately every 0.01 m. We collected data on a sample time interval of 0.1 ns and stacked each trace 8 times

4.3.4 Point Six – Dry Snowpack with No Evidence of Melt

In February of 2011, we collected a 12 m GPR profile on an undisturbed snowpack in a small glade in the saddle between Point Six Mountain and Big Sky Mountain, near Missoula, MT. The profile was collected over an area with a negligible slope at an elevation of ~2285 m. We measured the depth of snowpack, the density vs. depth profile of the snowpack, and the dielectric permittivity vs. depth profile of the snowpack in two snowpits, one located at the 4 m mark of the profile and one located at the 8 m mark profile (Figure 4.6A). The depth of the snowpack was ~2.45 m. We uncovered a fully buried tree in our snowpit located at the 4 m mark of our survey; the location of the tree can be seen in the radar profile where diffractions are present within the snowpack (Figure 4.6A). The snowpack included a ~0.20 m new snow layer and no evidence of melt. In each pit, we collected two vertical permittivity profiles on 0.05 m intervals. We used an odometer wheel to collect a GPR trace approximately every 0.01 m. A Doppler radar is located on Point Six peak; it is apparent that the signal from this strong radar source increased the background noise of the radar transect.

4.3.5 Preprocessing Data

Prior to deconvolution, we must first correct for amplitude losses and attenuate random and coherent noise. The largest sources of coherent noise were a low frequency noise component and ringing between antennae. The ringing can be neglected here because it dissipates prior to the surface reflection. We compensated for the low frequency noise component of the data with a dewow filter, which removes the DC bias and subsequent low frequency noise. We compensate for amplitude losses through a 3-D geometrical spreading gain function [*Yilmaz*, 2001]. We reduce random noise in our field data by stacking each recorded trace. However, the surface roughness of the field sites as well as small changes in geometry of the sled along the transect results in a random noise term that is inherent in the data but is not filtered out by stacking alone. Thus, we filtered this random noise by applying an eigenvector filter to the field data wherein we only keep the first four eigenvectors of each data set.

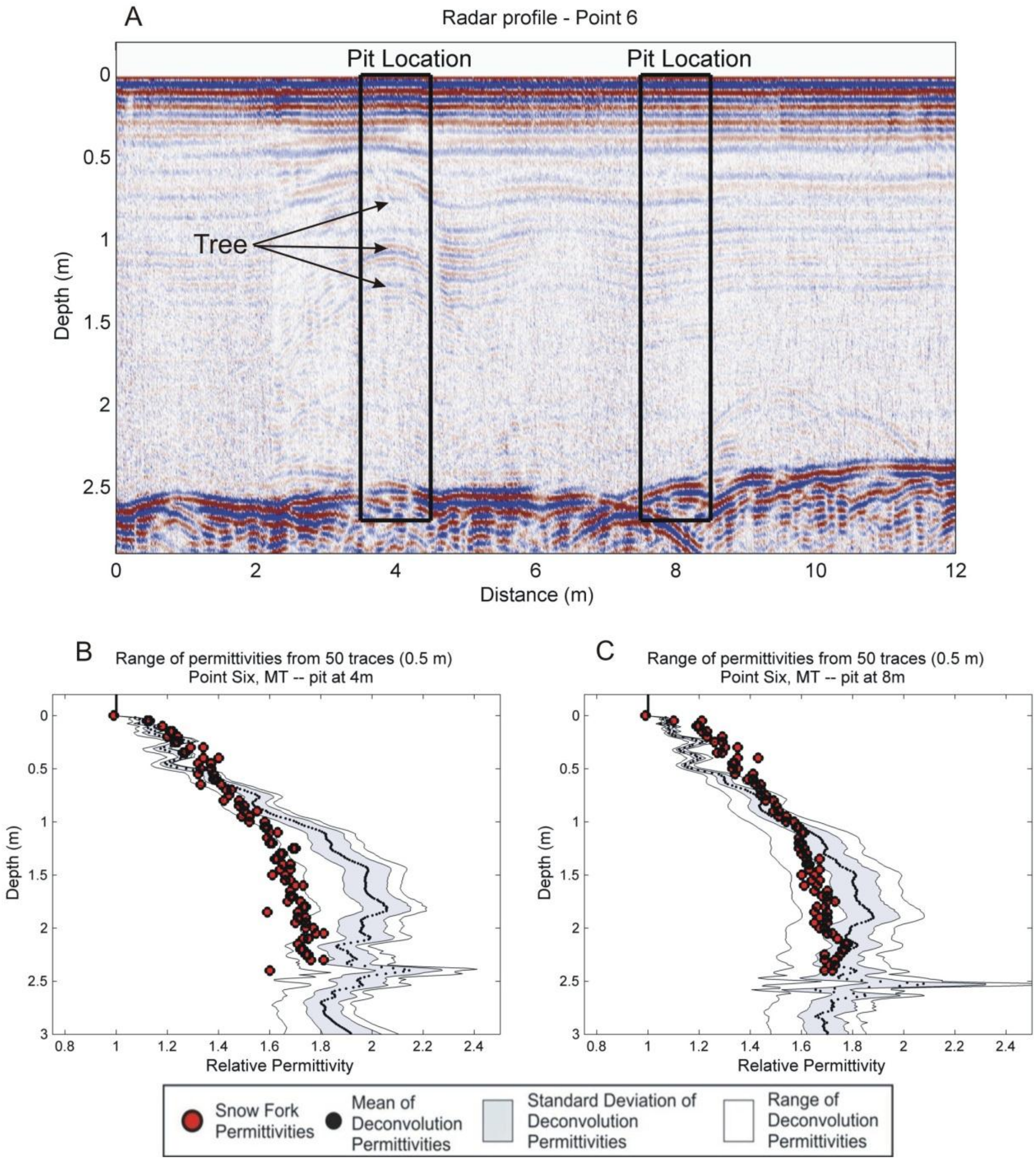

Figure 4.6 Common offset radar image from the Point Six Mountain site. The location if the pits are shown with black boxes. Hyperbolic reflections at pit 4 are due to a buried tree. Note the internal layering apparent in the upper 1.5 m of the transect and the large amount of background noise apparent throughout the image (A). Relative permittivity structure of the snowpack at the pit located at 4 m (B) and 8 m (C) along the transect at the Point Six Mountain survey site. The deconvolution solution is denoted by small black dots connected by a solid line. The mean real part of the permittivities measured with the Finnish Snow Fork are shown with a red filled dot, the red error bars on these points show the range of measured permittivities across the pit wall.

We use the same source wavelet for all locations. The velocity layers used to compensate for 3-D geometrical spreading are calculated from the snow fork permittivity measurements at each snowpit site. Where snow fork measurements are not available, a constant velocity could be used for the snowpack and the inversion could be used iteratively where the first iteration velocities could be used to compensate for 3-D geometrical spreading. At any given depth, this spreading function changes the calculated dielectric permittivity by up to 31%; however, the average change in calculated dielectric permittivity throughout the depth of the snowpack is less than 1%. We calculate the number of samples from the flattened time=0 horizon to the surface of the snowpack by calculating the theoretical time interval between transmission and receipt of the signal. This includes the height of the antenna off of the snow surface and the separation at the center of each antenna. To suppress edge effects inherent in the Fourier transform of a finite time signal, we apply a top mute above the surface reflection and a bottom mute to data below the ground reflection.

4.3.6 Measuring ε in Snowpits

We used a Finnish Snow Fork [*Sihvola and Tiuri*, 1986] to measure the depth vs. permittivity profile in snowpits located along the radar transect. The Finnish Snow Fork consists of a 2-pronged parallel-wire transmission-line resonator, a voltage controlled oscillator, and electronics for calculating the 3-dB bandwidth, attenuation, resonant frequency, and the real part of the dielectric permittivity. The Snow Fork measures the voltage vs. resonant frequency curve over a range of frequencies between 500 MHz and 900 MHz. The resonant frequency that results in the highest voltage reading and the frequencies that result in 3-dB lower than the peak voltage are found and used to calculate the resonant frequency (mean of the 3-dB frequencies), the 3-dB bandwidth, and the attenuation (peak voltage of measurement in air and recorded measurement) [*Sihvola and Tiuri*, 1986]. The Snow Fork calculates the real and complex parts of the dielectric permittivity of a small volume (~7.5 x 10^{-5} m^3) of snow surrounding the 2-pronged resonator with an approximate error in measured relative dielectric permittivity of 0.04 [*Vihma et al.*, 2011]. Since the Snow Fork effectively measures the dielectric permittivity of the snow, it is an excellent tool for comparison to GPR measurements. Further, previous studies successfully compared measurements made by the Snow Fork to GPR measurements [*Harper and Bradford*, 2003; *Marshall et al.*, 2005]. Here we are only interested in the real part of the permittivity, which is directly related to the propagation velocity of the EM wave in low loss media [*Annan*, 2005].

4.3.7 Comparing Snow Fork Measurements of ε to Calculated ε

At each of our pit sites, we solve for reflectivity and dielectric permittivity at each time step of the recorded signal. We then use the permittivity values to calculate the depth equivalent of each time sample, which ranges from 0.017 m to 0.027 m depending on permittivity. The spatial sampling of measurements for the snow fork was every 0.05 m to 0.10 m depth. Therefore, to compare the permittivities measured by the snow fork and calculated with the reflectivity analysis, we calculate the percent deviation between the measured snow fork permittivity values and the calculated permittivity values at the calculated time sample depth closest to the depth of snow fork measurements. At each location, we also give the percent variation in snow fork measurements at each depth across the ~1 m face of the snow pit.

4.4 Results

4.4.1 Lionhead Mountain, MT – Wet Snowpack

At Lionhead Mountain, our snow fork pit data show a permittivity of ~1.44 to ~1.7 at 0.05 m depth that decreases rapidly with depth to ~1.35 to ~1.41 at 0.15 m where the permittivity values then increase to ~1.59 to ~1.86 at the base of the snowpack (1.2 m depth) (Figure 4.4B). The permittivity values derived from the deconvolution solution of the radar traces follow the trend of the snow fork measurements from the surface to the base of the snowpack. The variation in measured snow fork permittivity values were less than 20% of the mean of the two or three measurements at all depths and were an average of 6.0% over the entire snow column. The inversion from the radar fits the snow fork data to within 21% of the measured dielectric permittivity at all depths and to an average of 11.6% of the measured dielectric permittivity of the entire snow column.

4.4.2 Lolo Pass, ID – Snowpack with Melt Induced Layering

At Lolo Pass, snow fork measured permittivity values increase with depth from ~1.09 to ~1.12 at 0.05 m to ~1.78 to ~1.94 at the base of the snow column at ~1.7 m in the pit located at 4 m along the transect (Figure 4.5B). At the pit located at 8 m along the transect, snow fork measured permittivity values increases with depth from ~1.1 at 0.05 m depth to ~1.81 to ~1.94 at the base of the snow column at ~1.85 m depth (Figure 4.5C). At both locations, the permittivity values derived from the deconvolution solution of the radar traces follow the trend of the snow fork measurements from the surface to the ground depth where there is a large discontinuity. At the 4 m pit, the inversion fits the data to within 20% of the snow fork measured dielectric permittivity at all depths and to an average of 8.1% of the snow fork measured dielectric permittivity of the entire snow column. The variability of the snow fork measurements were less than 22% of the average measurement at all depths and were an average of 3.3% over the entire snow column.

At the 8m pit, the inversion fits the data to within 21% of the snow fork measured dielectric permittivity at all depths and to an average of 8.8% of the snow fork measured dielectric permittivity of the entire snow column. The variability of the snow fork measurements were less than 22% of the average measurement at all depths and were an average of 4.7% over the entire snow column.

4.4.3 Point Six, MT – Dry Snowpack with No Evidence of Melt

At Point Six, MT snow fork measured permittivity increases with depth from ~1.13 at ~0.05 m depth to ~1.6 at ~1.2 m in the pit located 4 m along the transect, the permittivity increases slightly to ~1.75 between ~1.2 m and 2.3 m depth (Figure 4.6A). Similarly, the permittivity increases from ~1.10 to ~ 1.21 at ~0.05 m depth to ~1.6 at 1.1 m in the pit located 8 m along the transect, the permittivity increases very slowly to ~1.7 at ~2.4 m depth (Figure 4.6B). At both pit locations, the permittivity values derived from the deconvolution solution of the radar traces follow the trend of the snow fork measurements from the surface to ~1 m depth. Below 1 m depth, the calculated permittivity measurements keep increasing to ~2 at ~1.5 m depth where they do not change significantly through the rest of the snow column. Both locations show a spike in relative permittivity at a depth consistent with the ground depth. At the 4 m pit, the radar solution fits the snow fork data to within 23% of the snow fork measured dielectric permittivity at all depths and to an average of 10% of the snow fork measured dielectric permittivity of the entire snow column. The variability of the snow fork measurements were less than 12% of the average measurement at all depths and were an average of 2.0% over the entire snow column.

At the 8m pit, the inversion fits the data to within 14% of the snow fork measured dielectric permittivity at all depths and to an average of 6% of the snow fork measured dielectric permittivity of the entire snow column. The variability of the snow fork measurements were less than 11% of the average measurement at all depths and were an average of 2.0% over the entire snow column.

Our calculated permittivity profiles at all five snowpit locations show good agreement with permittivities measured with the snow fork. This includes an average deviation between snow fork and calculated permittivities of less than 10% at all locations as well as matching general trend of permittivity with depth values at each location. However, our solutions do not perfectly match the snow fork data at each depth point. Our calculated permittivity profiles from Lionhead Mountain are consistently low from the surface to ~1 m depth. In both snow pits at the Lolo Pass site, the calculated permittivity values for are lower than the permittivity values measured with the snow fork between ~0.10 m through ~1 m depth. The calculated permittivity in both snow pits at the Point Six site show higher permittivity values than the measured snow fork permittivities at depths between ~1 m and the snow/soil interface.

4.5 Discussion

It is apparent that deconvolution of radar data is a promising method for calculating the permittivity profile of a seasonal snowpack from common offset GPR data. The method we use herein works in a variety of snowpacks with depths ranging from 1.2 m to 2.5 m depth. It is also apparent that deconvolving field data is not totally straight forward and problem free. Indeed, it is likely that the calculated permittivity values deviate from the snow fork measurements at the Point Six site is in part due to the noise from a Doppler antenna located near the study site (frequency ~3 GHz – 10 GHz). This would be an example of the cumulative error effect of using a layer stripping to solve for the dielectric permittivity of the entire snow column. However, this does not preclude that the deviation may be due to long wavelength changes in snow density in the bottom 1.5 m of the snowpack or due to the presence of buried vegetation like the tree found in the snow pit at 4 m along the transect. It is also likely that, at the Lolo Pass site, the low permittivity values calculated near the surface are not accurate and may be due to the low density surface snow layer or could be artifacts from edge effects from the forward and inverse Fourier transform.

Sources of error that are inherent in deconvolution of real data include fitting noise, incorrect source wavelet estimation, and frequency bandlimiting, which creates both ‘smearing’ of the reflectivity series and a loss of the long wavelength changes in electrical properties in the subsurface [*Russell*, 2009]. The assumptions of convolution that we list in the Section 4.2 must be close to valid for this method to work. For example, large amounts of liquid water in the snowpack would result in wavelet dispersion, which would violate Assumption 3. By recovering the shape and amplitude of the source wavelet and assuming that the noise term is negligible, we reduce the unknowns in Equation (3) to one that allows us to solve for the vertical reflectivity series, which is defined by the dielectric permittivity contrasts within the snowpack. The data we use herein were collected in seasonal snowpack composed almost entirely of ice, air, and liquid water. The snowpacks were stratified in nearly parallel horizons that are defined mainly by density and wetness differences. The horizon boundaries within the snowpacks are due to 1) changes in snowpack properties between depositional storm events including vertical heat exchange and surface melt, 2) separate depositional storm events, and 3) differences in deposition rate during a single storm event. The density and wetness of a snowpack directly affects the snowpack dielectric permittivity. Since the density variations within the snowpack are discrete and are smaller scale than the wavelength of the radar signal, this is an ideal medium for calculating dielectric permittivity through deconvolution.

In Section 4.2 we show that this method works only when the noise term in the data is negligible. In order to give an idea of the sensitivity of this method to noise, we ran our inversion with varying levels of noise filter for the Point Six data at the 8 m pit. We ran identical inversions with varying levels of noise attenuation from the eigenvector filter. As stated in Section 4.3.5, we use only the first four eigenvectors in our inversions. This is 1% of the eigenvectors for the Point Six data; for this analysis, we also use 10%, 25%, and 50% of the eigenvectors for the Point Six data (Figure 4.7). The large variation in range of solutions (Figure 4.8) indicates that the inversion is highly sensitive to small lateral changes in the data. There also appears to be a bias introduced to the solution, which increases as the random noise increases.

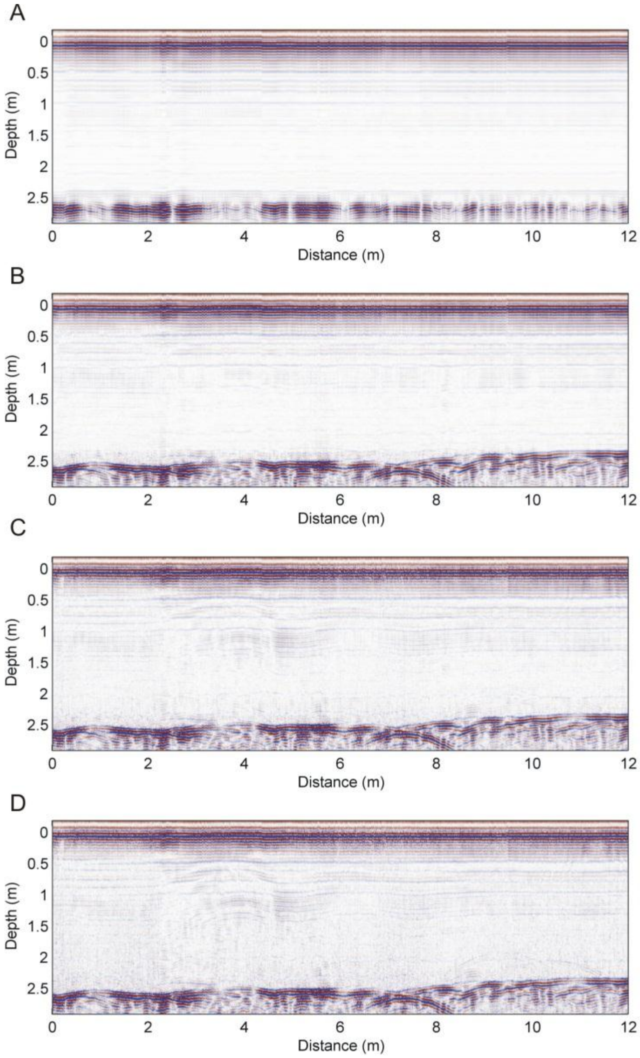

Figure 4.7- Images of georadar data collected at Point Six showing the first A) 1%, B) 10%, C) 25%, and D) 50% of the eigenvectors within the data.

This method of calculating the dielectric permittivity structure of seasonal snowpack with common offset GPR surveys has the potential to map variations of snow properties over large areas. Because dielectric permittivity is related to density in dry snow [e.g., *Sihvola and Tiuri*, 1986; *Harper and Bradford*, 2003], this method can also be used to accurately estimate snow water equivalent (SWE) over large areas of dry snow. Further, if the wetness of a snowpack is in the pendular regime, deconvolution could be used in conjunction with measuring the frequency dependent GPR signal [*Bradford et al.*, 2009] to determine SWE in snowpacks with small amounts of liquid water.

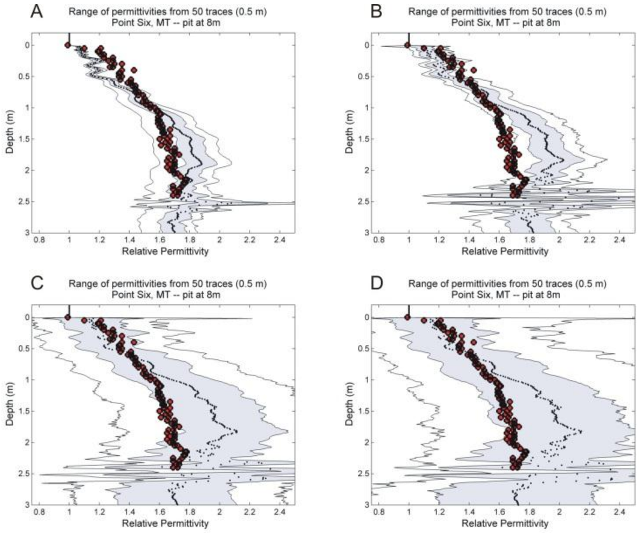

Figure 4.8 Relative permittivity structure of the snowpack at the pit located at 8 m along the transect at the Point Six Mountain survey site. The permittivities were calculated with the first (A) 1%, (B) 10%, (C) 25%, and (D) 50% of the eigenvectors within the data. The deconvolution solution is denoted by small black dots connected by a solid line. The mean real part of the permittivities measured with the Finnish Snow Fork are shown with a red filled dot, the red error bars on these points show the range of measured permittivities across the pit wall.

4.6 Conclusions

We show that deconvolution of common offset GPR data can be used to calculate the dielectric permittivity structure of seasonal snowpacks under a variety of conditions from dry and deep to layered snowpacks with melt-induced high density layers to a snowpack that is currently undergoing melt. Deconvolution of common offset georadar data is a promising method of determining the permittivity structure of snowpack and could be used to map depths of snowpacks over large areas with relatively high precision. Density of dry snowpacks could also be mapped, resulting in accurate measurements of snow water equivalent over large areas. This technique could also be used to constrain retrievals of SWE from airborne and space-borne microwave radar.

REFERENCES

Abdalati, W. (2007), Greenland Ice Sheet Melt Characteristics Derived from Passive Microwave Data, 02 April 1979 - 31 October 2007. Boulder, Colorado USA: National Snow and Ice Data Center. Digital media.

Annan, A.P. (2005), *Ground-penetrating radar*, In: Butler, D.K. (Ed.), Near-Surface Geophysics. Society of Exploration Geophysicists, Tulsa, OK, 357-438.

Annan, A. P., and S. Cosway (1992), Ground penetrating radar survey design, *Proceedings of the Symposium on the Applications of Geophysics to Engineering and Environmental Problems (SAGEEP),* Environ. and Eng. Geophys. Soc., Englewood, Colorado.

Arcone, S.A., V.B. Spikes, G.S. Hamilton, and P.A. Mayewski (2004), Stratigraphic continuity in 400MHz short-pulse radar profiles of firn in West Antarctica, *Annals of Glaciology, 39*, 195-200.

Bahr, D.B., Dyurgerov, M. and Meier, M.F. (2009), Sea-level rise from glaciers and ice caps: A lower bound, *Geophysical Research Letters, 36*, L03501. doi:10.1029/2008GL036309.

Balanis, C. (2008), *Modern Antenna Handbook*, John Wiley & Sons, Hoboken, N.J.

Bales, R. C., Q. Guo, D. Shen, J. R. McConnell, G. Du, J. F. Burkhart, V. B. Spikes, E. Hanna, and J. Cappelen (2009), Annual accumulation for Greenland updated using ice core data developed during 2000–2006 and analysis of daily coastal meteorological data, *J. Geophys. Res.*, *114*, D06116, doi:10.1029/2008JD011208.

Bamber, J.L., R.L. Layberry, S.P. Gogenini (2001), A new ice thickness and bed data set for the Greenland Ice Sheet 1: Measurement, data reduction, and errors, *J. Geophys. Res.*, *106*, D24, 33773-33780.

Benson, C.S. (1960), Stratigraphic studies in the snow and firn of the Greenland Ice Sheet, (Ph.D. thesis, California Institute of Technology).

Bøggild, C. E. (2000), Preferential flow and melt water retention in cold snow packs in West-Greenland, *Nordic Hydrology*, *31*(4/5), 287-300.

Bolch, T., Menounos, B., and Wheate, R. (2010), Landsat-based inventory of glaciers in western Canada, 1985 - 2005, *Remote Sensing of Environment 114*, 127-137.

Box, J. E., D. H. Bromwich, and L.-S. Bai (2004), Greenland Ice Sheet surface mass balance 1991–2000: Application of Polar MM5 musicale model and in situ data, *J. Geophys. Res.*, *109*, D16105, doi:10.1029/2003JD004451.

Bradford, J. H. (2006), Applying reflection tomography in the postmigration domain to multi-fold GPR data, *Geophysics*, *71*(1), K1– K8.

Bradford, J.H. (2002), Depth characterization of shallow aquifers with seismic reflection, part I—The failure of NMO velocity analysis and quantitative error prediction, *Geophysics*, *67*, 89–97, doi:10.1190/1.1451362.

Bradford, J. H. (2007), Frequency dependent attenuation analysis of ground-penetrating radar data, *Geophysics*, *72*, J7 –J16.

Bradford, J. H., J. T. Harper, and J. Brown (2009), Complex dielectric permittivity measurements from ground-penetrating radar data to estimate snow liquid water content in the pendular regime, *Water Resour. Res.*, *45*, W08403, doi:10.1029/2008WR007341.

Braithwaite R.J., M. Laternser, and W.T. Pfeffer, (1994), Variations of near-surface firn density in the lower accumulation area of the Greenland Ice Sheet, Pikitsoq, West Greenland, *J. Glaciol.*, *40*(136).

Brown, J., J. Nichols, L. Steinbronn, J. Bradford (2009), Improved GPR interpretation through resolution of lateral velocity heterogeneity: example from an archaeological site investigation, *Journal of Applied Geophysics*, *68*, 3–8.

Brown, J., J. Harper, W.T. Pfeffer, N. Humphrey, and J. Bradford (2011), High resolution study of layering within the percolation and soaked facies of the Greenland Ice Sheet, *Annals of Glaciology*, *52*(59).

Brown, J., J. Bradford, J. Harper, W. T. Pfeffer, N. Humphrey, and E. Mosley-Thompson (2012), Georadar-derived estimates of firn density in the percolation zone, western Greenland Ice Sheet, *Journal of Geophysical Research*, *117*, F01011, doi:10.1029/2011JF002089.

Claerbout, J.F. (1992) *Earth Soundings Analysis: Processing Versus Inversion*, Blackwell, Boston, Mass.

Clement, W., and W. Barrash (2006), Crosshole radar tomography in a fluvial aquifer near Boise, Idaho, *J. Environ. Eng. Geophys.*, *11*, 171–184, doi:10.2113/JEEG11.3.171.

Clement, W., and M.D. Knoll (2006), Traveltime inversion of vertical radar profiles, *Geophysics*, *71*(3), K67-K76.

DeBeer, C.M., and M.J. Sharp (2009), Topographic influences on recent changes of very small glaciers in the Monashee Mountains, British Columbia, Canada, *Journal of Glaciology*, *55*(192), 691-700.

Dix, C. H. (1955), Seismic velocities from surface measurements, *Geophysics*, *20*, 68–86.

Dunse T., O. Eisen, V. Helm, W. Rack, D Steinhage, and V. Parry (2008), Characteristics and small-scale variability of GPR signals and their relation to snow accumulation in Greenland's percolation zone, *J. Glaciol.*, *34*(185).

Dyurgerov, M.B. and Meier, M.F. (2000), Twentieth century climate change: Evidence from small glaciers, *Proceedings of the National Academy of Sciences of the United States of America*, *97*(4), 1406-1411.

Fausto R., A. Ahlstrom, D. Van As, C. Boggild, and S. Johnsen (2009), A new present-day temperature parameterization for Greenland, *J. Glaciol.*, 55(189), 95-105.

Finklin, A.I. (1986), *A Climatic Handbook for Glacier National Park - with Data for Waterton Lakes National Park,* General Technical Report INT-204. U.S. Department of Agriculture, Forest Service, Intermountain Research Station, Ogden, UT.

Fischer, H., D. Wagenbach, M. Laternser, and W. Haeberli (1995), Glacio-meteorological and isotopic studies along the EGIG line, central Greenland, *J. Glaciol.*, *41*(139), 515–527.

Fisher, E., G. McMechan, and A. P. Annan (1992), Acquisition and processing of wide-aperture ground-penetrating radar data, *Geophysics*, *57*(3), 495–504.

Fountain, A.G., Hoffman, M.J., Granshaw, F. and Riedel, J. (2009), The 'benchmark glacier' concept does it work? Lessons from the North Cascade Range, USA, *Annals of Glaciology, 50*, 163-168.

Gillan, B.J., Harper, J.T. and Moore, J.N. (2010), Timing of present and future snowmelt from high elevations in northwest Montana, *Water Resources Research*, *46,* W01507. doi:10.1029/2009WR007861.

Granshaw, F.D. and Fountain, A.G. (2006), Glacier change (1958-1998) in the North Cascades National Park Complex, Washington, USA, *Journal of Glaciology*, *52*(177), 251-256.

Gudmandsen, P. (1971), Electromagnetic probing of ice, in *Electromagnetic Probing in Geophysics*, edited by J. R. Wait, pp. 321-348, The Golem Press, Colo.

Haeberli, W., Hoelzle, M., Paul, F. and Zemp, M. (2007), Integrated monitoring of mountain glaciers as key indicators of global climate change: the European Alps, *Annals of Glaciology*, *46*, 150-160.

Hall, M.H.P. and Fagre, D.B. (2003), Modeled climate-induced glacier change in Glacier National Park, 1850-2100, *Bioscience*, *53*(2), 131-140.

Hanna E., P. Huybrechts, I. Janssens, J. Cappelen, K. Steffen, and A. Stephens (2005), Runoff and mass balance of the Greenland Ice Sheet: 1958-2003, *J. Geophys. Res.*, *110*, D13108, doi:10.1029/2004JD005641.

Hansen, J., Sato, M., Ruedy, R., Lo, K., Lea, D.W. and Medina-Elizade, M. (2006), Global temperature change, *Proceedings of the National Academy of Sciences of the United States of America*, *103*(39), 14288-14293, doi:10.1073/pnas.0606291103.

Harper, J.T. and Humphrey, N.F. (2003), High altitude Himalayan climate inferred from glacial ice flux, *Geophysical Research Letters*, *30*(14), 1764-1767, doi:10.1029/2003GL017329.

Harper, J.T. and J.H. Bradford (2003), Snow stratigraphy over a uniform depositional surface: spatial variability and measurement tools, *Cold Regions Science and Technology, 37*, 289– 298.

Harper, J.T., J.H. Bradford, N.F. Humphrey, and T.W. Meierbachtol (2010), Vertical extension of the subglacial drainage system into basal crevasses, *Nature, 467*, 579-582, doi: 10.1038/nature09398.

Helm, V., W. Rack, R. Cullen, P. Nienow, D. Mair, V. Parry, and D. J. Wingham (2007), Winter accumulation in the percolation zone of Greenland measured by airborne radar altimeter, *Geophys. Res. Lett.*, *34*, L06501, doi:10.1029/2006GL029185.

Helsen, M. M., M. R. van den Broeke, R. S. W. van de Wal, W. J. van de Berg, E. van Meijgaard, C. H. Davis, Y. Li, and I. Goodwin (2008), Elevation changes in Antarctica mainly determined by accumulation variability, *Science, 320*, 1626–1629, doi:10.1126/science.1153894.

Hempel, L., F. Thyssen, N. Gundestrup, H. B. Clausen, and H. Miller (2000), A comparison of radio echo sounding data and electrical conductivity of the GRIP ice core, *J. Glaciol.*, *46*, 369– 374.

Herron, M. M., and C. C. Langway Jr. (1980), Firn densification: An empirical model, *J. Glaciol.*, *25*, 373–385.

Holland, P. R., H. F. J. Corr, H. D. Pritchard, D. G. Vaughan, R. J. Arthern, A. Jenkins, and M. Tedesco (2011), The air content of the Larson Ice Shelf, *Geophys. Res. Lett.*, *38*, L10503, doi:10.1029/2011GL047245.

Hooke, R.L. (1998), *Principles of Glaciers Mechanics*, Prentice-Hall, Englewood Cliffs, N. J., 248 pp.

Hörhold, M. W., S. Kipfstuhl, F. Wilhelms, J. Freitag, and A. Frenzel (2011), The densification of layered polar firn, *J. Geophys. Res.*, *116*, F01001, doi:10.1029/2009JF001630.

Hou, S. and D. Qin (2002), The effect of post depositional process on the chemical profiles of snow pits in the percolation zone, *Cold Reg. Sci. Technol., 34*(2), 111–116.

Huisman, J.A., S.S. Hubbard, J.D. Redman, A.P. Annan (2003), Measuring soil water content with ground penetrating radar: a review, *Vadose Zone, 2*, 476–491.

IPCC (2007), *Climate Change 2007: Synthesis Report. Contribution of Working Groups I, II and III to the Fourth Assessment Report of the Intergovernmental Panel on Climate Change*, IPCC, Geneva, Switzerland.

Jezek K.C., P. Gogineni and M. Shanableh (1994), Radar Measurements of Melt Zones on the Greenland Ice Sheet, *Goephys. Res. Lett., 21*, 33-36.

Kohler, J., J.C. Moore, and E. Isaksson (2003), Comparison of modeled and observed responses of a glacier snowpack to ground-penetrating radar. *Ann. Glaciol., 37*, 293–297.

Knight, R., P. Tercier, and J. Irving (2004), The effect of vertical measurement resolution on the correlation structure of a ground penetrating radar reflection image, *Geophys. Res. Lett., 31*, L21607, doi:10.1029/2004GL021112.

Kuhn, M. (1995), The mass balance of very small glaciers, *Zeitschrift fur Gletscherkunde und Glazialgeologie, 31*(1), 171-179.

Latimer, R., R. Davidson, and P. van Riel (2000), An interpreter's guide to understanding and working with seismic-derived acoustic impedance data, *The Leading Edge*, *19*(3), 242-256.

Legarsky, J. J., and X. Gao (2006), Internal layer tracing and age-depth relationship from the ice divide toward Jacobshavn, Greenland, *IEEE Geoscience and Remote Sensing Letters*, *3*(4), 471-475.

Leiva, J.C., Cabrera, G.A. and Lenzano, L.E. (2007), 20 years of mass balances on the Piloto glacier, Las Cuevas river basin, Mendoza, Argentina, *Global and Planetary Change*, *59*(1-4), 10-16. doi:10.1016/j.gloplacha.2006.11.018

Liberty, L.M., and J.R. Pelton (1994), A comparison of ground-penetrating radar methods: multi-fold data vs. single fold data. In: *Link, P.K. (Ed.), 30th Symposium on Engineering Geology and Geotechnical Engineering: Hydrogeology,Waste Disposal*, *Science and Politics*, Idaho State University, Pocatello, ID, 321–324.

Lundberg, A., H. Thunehed, and J. Bergstrom (2000), Impulse radar snow surveys: Influence of snow density, *Nordic Hydrology*, *31*, 1–14.

Machguth, H., O. Eisen, F. Paul, and M. Hoelzle (2006), Strong spatial variability of snow accumulation observed with helicopter-borne GPR on two adjacent Alpine glaciers, *Geophys. Res. Lett., 33*, L13503, doi:10.1029/2006GL026576.

Maeno N. and T. Ebinuma (1983), Pressure sintering of ice and its implication to the densification of snow at polar glaciers and ice sheets, *Journal of Physical Chemistry, 87*(21), 4103-4 110.

Marshall, H. P., G. Koh, and R. Forster (2005), Estimating alpine snowpack properties using FMCW radar, *Ann. Glaciol.*, *40*(1), 157– 162.

McConnell, J. R., R. J. Arthern, E. Mosley-Thompson, C. H. Davis, R. C. Bales, R. Thomas, J. F. Burkhart, and J. D. Kyne (2000), Changes in Greenland Ice Sheet elevation attributed primarily to snow accumulation variability, *Nature*, *406*, 877–879.

Meier, M.F. and Dyurgerov, M.B. (2002), Sea level changes: How Alaska affects the world, *Science*, *297*(5580), 350-351.

Moore, R.D., Fleming, S.W., Menounos, B., Wheate, R., Fountain, A., Stahl, K., Holm, K. and Jakob, M. (2009), Glacier change in western North America: influences on hydrology, geomorphic hazards and water quality, *Hydrological Processes*, *23*(1), 42-61. doi:10.1002/hyp.7162

Mosley-Thompson, E., J. R. McConnell, R. C. Bales, Z. Li, P.-N. Lin, K. Steffen, L. G. Thompson, R. Edwards, and D. Bathke (2001), Local to regional-scale variability of Greenland accumulation from PARCA cores, *J. Geophys. Res.*, *106*(D24), 33,839–33,851.

Murray, T., A. Booth and D.M. Rippin (2007), Water-content of glacier-ice: limitations on estimates from velocity analysis of surface ground-penetrating radar surveys, *J. Environ. Eng. Geophys., 12*(1), 87–99.

Nesje, A., Bakke, J., Dahl, S.O., Lie, O. and Matthews, J.A. (2008), Norwegian mountain glaciers in the past, present and future, *Global and Planetary Change*, *60*(1-2), 10-27. doi:10.1016/j.gloplacha.2006.08.004.

Nghiem, S. V., K. Steffen, G. Neumann, and R. Huff (2005), Mapping of ice layer extent and snow accumulation in the percolation zone of the Greenland Ice Sheet, *J. Geophys. Res.*, *110*, F02017, doi:10.1029/2004JF000234.

Nye, J.F. (1951), The Flow of Glaciers and Ice-Sheets as a Problem in Plasticity, *Proceedings of the Royal Society of London. Series A, Mathematical and Physical Sciences*, *207*(1091), 554-572.

Nyquist, H. (1928), Certain topics in telegraph transmission theory, *AIEE Trans.*, *47*, 617–644.

Oerlemans, J. (2001), *Glaciers and Climate Change*, A.A. Balkema Publishers, Lisse, 148 pp.

Oerlemans, J. (2005), Extracting a climate signal from 169 glacier records, *Science*, *308*(5722), 675-677. doi:10.1126/science.1107046.

Parry, V., P. Nienow, D. Mair, J. Scott, B. Hubbard, K. Steffen and D. Wingham (2007), Investigations of meltwater refreezing and density variations in the snowpack and firn within the percolation zone of the Greenland Ice Sheet, *Annals of Glaciology*, *46*, 61-68.

Paterson, W.S.B. (2002), *The physics of glaciers, Third edition*, Oxford, etc., Elsevier.

Parry, V., P. Nienow, D. Mair, J. Scott, B. Hubbard, K. Steffen and D. Wingham (2007), Investigations of meltwater refreezing and density variations in the snowpack and firn within the percolation zone of the Greenland Ice Sheet, *Annals of Glaciology*, *46*.

Paul, F., Maisch, M., Rothenbuhler, C., Hoelzle, M. and Haeberli, W. (2007), Calculation and visualisation of future glacier extent in the Swiss Alps by means of hypsographic modelling, *Global and Planetary Change*, *55*(4): 343-357. doi:10.1016/j.gloplacha.2006.08.003.

Pederson, G.T., Gray, S.T., Fagre, D.B. and Graumlich, L.J. (2006), Long-duration drought variability and impacts on ecosystem services: A case study from Glacier National Park, Montana, *Earth Interactions*, *10*(4), 1-28.

Pederson, G.T., Graumlich, L.J., Fagre, D.B., Kipfer, T., & Muhlfeld, C.C. (2010), A century of climate and ecosystem change in western Montana: what do temperature trends portend?, *Climatic Change*, *98*, 133-154. doi:10.1007/ s10584-009-9642-y.

Pfeffer, W.T. and N.F. Humphrey (1998), Formation of ice layers by infiltration and refreezing of meltwater, *Annals of Glaciology*, *26*, 83-91.

Pfeffer, W. T., M. F. Meier, and T. H. Illangasekare (1991), Retention of Greenland runoff by refreezing: Implications for projected future sea-level change, *J. Geophys. Res.*, *96*(C12), 22,117–22,124.

Pipan, M., I. Finetti, and F. Ferigo (1996), Multi-fold GPR techniques with applications to high resolution studies: two case histories, *European Journal of Environmental and Engineering Geophysics*, *1*, 83-103.

Robin, G. De Q., S. Evans and J. T. Bailey (1969), Interpretation of Radio Echo Sounding in Polar Ice Sheets, *Philosophical Transactions of the Royal Society of London. Series A, Mathematical and Physical Sciences*, *265*(1166), 437-505.

Russell, B. (2009), *Introduction to Seismic Inversion Methods, Course Notes Series, No. 2,* S. Domenico (ed.), 172 pp., Soc. of Explor. Geophys., Tulsa, Okla.

Schneeberger, C., Blatter, H., Abe-Ouchi, A. and Wild, M. (2003), Modelling changes in the mass balance of glaciers of the northern hemisphere for a transient 2 x CO2 scenario, *Journal of Hydrology*, *282*(1-4), 145-163. doi:10.1016/s0022-1694(03)00260-9.

Scott, J. B. T., P. Nienow, D. Mair, V. Parry, E. Morris, and D. J. Wingham (2006a), Importance of seasonal and annual layers in controlling backscatter to radar altimeters across the percolation zone of an ice sheet, *Geophys. Res. Lett.*, *33*, L24502, doi:10.1029/2006GL027974.

Scott, J.B.T., D. Mair, P. Nienow, V. Parry, E. Morris and D.J.Wingham (2006b), A ground-based radar backscatter investigation in the percolation zone of the Greenland Ice Sheet, *Remote Sensing of Environment*, *104*, 361–373, doi:10.1016/j.rse.2006.05.009.

Shindell, D. and Faluvegi, G. (2009), Climate response to regional radiative forcing during the twentieth century, *Nature Geoscience*, *2*(4), 294-300. doi:10.1038/ngeo473.

Sihvola, A. H., and M. E. Tiuri (1986), Snow fork for field determination of the density and wetness profiles of a snow pack, *IEEE Trans. Geosci. Remote Sens.*, *GE-24*(5), 717– 721.

Smith, G.S. (1984), Directive properties of antennas for transmission into a material half-space, *IEEE Transactions on Antennas and Propagation*, *AP-32*(3), 232– 246.

Snieder, R. (2001), *A Guided Tour of Mathematical Methods of the Physical Sciences*, 429 pp., Cambridge University Press, Cambridge, United Kingdom.

Spikes, V.B., G.S. Hamilton, S.A. Arcone, S. Kaspari and P.A. Mayewski (2004), Variability in accumulation rates from GPR profiling on the West Antarctic Plateau, *Annals of Glaciology*, *39*, 238-244.

Steffen, K., J. E. Box, and W. Abdalati (1996), Greenland Climate Network: GC-Net, in *Special Report on Glaciers, Ice Sheets and Volcanoes: A Tribute to Mark F. Meier Special Report 96–-27*, pp. 98-103, Cold Regions Research Engineering Laboratory, Hanover, New Hampshire.

Tiuri, M. E., A. Sihvola, E. Nyfors, and M. Hallikainen (1984), The complex dielectric constant of snow at microwave frequencies, *IEEE Journal of Oceanic Engineering*, *OE-9*(5), 377–382.

Ulaby, F.T., R.K. Moore, A.K. Fung (1981), *Microwave Remote Sensing Active and Passive, Vol. 1: Microwave Remote Sensing Fundamentals and Radiometry*, Addison-Wesley.

Valle, S., L. Zanzi, M. Sgheiz, G. Lenzi, J. Friborg (2001), Ground penetrating radar antennas: theoretical and experimental directivity functions, *IEEE Transactions on Geoscience and Remote Sensing*, *39*(4), 749– 758.

Vaughan, D.G., H.F. Corr, C.S.M, Doake and Ed. D. Waddington, ED (1999), Distortion of isochronous layers in ice revealed by ground-penetrating radar, *Nature*, *398*(6725), 323-326.

Vihma, T., O. P. Mattila, R. Pirazzini, and M. M. Johansson (2011), Spatial and temporal vaiability in summer snow pack in Dronning Maud Land, Antarctica, *The Cryosphere*, *5*, 187-201, doi:10.5194/tc-5-187-2011.

Wensink, W.A., G. Greeuw, J. Hofman, J.K. van Deen (1990), Measured underwater near-field E-patterns of a pulsed, horizontal dipole antenna in air: comparison with the theory of the continuous wave, infinitesimal electric dipole, *Geophysical Prospecting*, *38*, 805– 830.

Wharton, R. P., G. A. Hazen, R. N. Rau, and D. L. Best (1980), Electromagnetic propagation logging: Advances in technique and interpretation, *paper presented at 55th Annual Fall Technical Conference and Exhibition*, Soc. of Pet. Eng., Dallas, Tex.

Yilmaz, Ö (2001), *Seismic data analysis*, Society of Exploration Geophysicists, Tulsa, Okla.

Zelt, C. A., and R. B. Smith (1992), Seismic traveltime inversion for 2-D crustal velocity structure, *Geophys. J. Int*., *108*, 16–31.

Zwally, H. J., and J. Li (2002), Seasonal and interannual variations of firn densification and ice-sheet surface elevation at the Greenland summit, *J. Glaciol.*, *48*, 199-207.

Zwally, H. J., M. B. Giovinetto, J. Li, H. G. Cornejo, M. A. Beckley, A. C. Brenner, J. L. Saba, and D. Yi (2005), Mass changes of the Greenland and Antarctic ice sheets and shelves and contributions to sea level rise: 1992–2002, *J. Glaciol.*, *51,* 509–527.

APPENDIX: CIRQUE GLACIER SENSITIVITY TO 21st CENTURY WARMING: SPERRY GLACIER, ROCKY MOUNTAINS, U.S.A.*

This chapter is published by Elsevier in *Global Planetary Change* and should be referenced appropriately.

Reference:

Brown, J.M., Harper, J.T., and Humphrey, N., 2010, Cirque Glacier Sensitivity to 21st Century Warming: Sperry Glacier, Rocky Mountains, U.S.A., *Global Planetary Change*, 74, 91-98, doi:10.1016/j.gloplacha.2010.09.001.

Reproduced/modified by permission of Elsevier.

*This chapter includes modifications from the originally published version.

CIRQUE GLACIER SENSITIVITY TO 21st CENTURY WARMING: SPERRY GLACIER, ROCKY MOUNTAINS, U.S.A.

Joel Brown [a,b]

Joel Harper [a]

Neil Humphrey [c]

[a] *Department of Geosciences, University of Montana, 32 Campus Dr., Missoula, MT 59812, USA*

[b] *Center for Geophysical Investigation of the Shallow Subsurface, Boise State University, 1910 University Dr., Boise, ID 83725, USA*

[c] *Geology and Geophysics Dept. 3006, University of Wyoming, Laramie, Wyoming 82071, USA*

Published in:

Global and Planetary Change 74 (2010) 91–98

Abstract

The interpretation of climate change based on the behavior of small cirque glaciers is not always straightforward or unique. In this study of Sperry Glacier, Glacier National Park, Montana, we model future change of the glacier under 11 different warming scenarios. The scenarios vary from no warming from present conditions to warming at a linear rate of 10 °C/century. We assume constant precipitation and only consider change invoked by warming. Our cellular automata model is based on simple rules that account for mass balance gradient, aspect, avalanching, and the flow of ice to redistribute mass. We constrain the model with glaciological data including georadar-measured ice depth, field-measured surface mass balance, and field-mapped ice surface topography. Under the most probable temperature increase based on downscaled OA-GCM output for the IPCC A1B scenario, we conservatively estimate the glacier persisting through at least 2080. By comparing glacier volume responses to different warming scenarios, we elucidate a relationship between the magnitude of temperature change and the sensitivity of the glacier to small variations in the temperature increase. We find that the greater the magnitude of the temperature increase, the less sensitive the glacier area and volume become to slight differences in the warming rate. If we generalize this relationship to the region, we expect that a small change in climate will produce varying responses for glaciers throughout the region, whereas the glacier response to a large change in climate will likely be very similar over the entire region.

A.1 Introduction

Area and volume adjustments of mountain glaciers have important impacts on society and natural systems. Most notable are the contributions of mountain glaciers to sea level rise [e.g., *Bahr et al.*, 2009; *Meier and Dyurgerov*, 2002], and the influence of mountain glaciers on water resources and geomorphic hazards [e.g., *Leiva et al.*, 2007; *Moore et al.*, 2009]. Since mountain glaciers are considered sensitive indicators of climate, they are used to detect and monitor local climate change in regions not typically monitored by instrumentation [e.g., *Haeberli et al.*, 2007]. Further, observations of glacier change are independent from potential issues related to the location, instrumentation, and processing of weather station data. Consequently, the general global retreat of mountain glaciers [*Dyurgerov and Meier*, 2000] is commonly cited as corroborating evidence for 20th century climate warming of the instrumental temperature record. For example, *Oerlemans* [2005] used the length records of 169 glaciers located around the world to construct a quantitative record of 20th century warming, and found that the glacier record agreed remarkably well with the instrumental record.

With projected increases to the rate of warming in the 21st century [*IPCC*, 2007], a general acceleration of rates of glacier retreat appears likely. For many small mountain glaciers, projecting their recent rate of retreat forward implies they will disappear within the 21st Century [e.g., *Nesje et al.*, 2008]. However, the small glaciers within a region do not always advance or retreat at the same rate as large ones [*Fountain et al.*, 2009; *Granshaw and Fountain*, 2006] and past advances or retreats of a glacier may not indicate how that glacier will change in the future. As mountain glaciers become small, many begin to occupy little more than the area below their cirque headwall. Near the cirque, winter snow accumulation is often enhanced from wind drifting and avalanching from the steep cliffs above, while radiation shading reduces summer ablation [*Kuhn*, 1995]. Consequently, cirque glaciers are sometimes considered products of topography and therefore inappropriate indicators of climate variability and change [*Kuhn*, 1995]. In addition, climate change within a region is not typically spatially uniform [e.g., *Shindell and Faluvegi*, 2009]. Therefore, similar glaciers in different basins within the same region may not experience identical changes in climate and thus may have slightly different volume and area changes.

Some small cirque glaciers may be more (or less) sensitive to climate change than other small cirque glaciers, making the interpretation of climate based on small glaciers difficult. In the Cascade Mountains of Washington State, U.S., larger glaciers lost less fractional area than smaller glaciers during last half of the 20th century [*Granshaw and Fountain*, 2006]. Further north in a western Canadian mountain range, *DeBeer and Sharp* [2009] found that 75 of 86 small glaciers showed no observable size change during a similar time period. The lack of change implies that either this mountain region experienced no late 20th century warming, or that the small glaciers failed to respond to any warming. The authors suggest the lack of glacier change was due to the small size and sheltered locations of glaciers, which allowed them to be roughly in balance with late 20th century climate conditions. In a study covering ~10^6 km^2 of western Canada between 1985 and 2005, *Bolch et al.* [2010] show highly variable reductions in area of glaciers less than 5 km^2, but many showing reductions of several tens of percent. Hence, projecting future change of small glaciers, or interpreting their ongoing changes, requires detailed understanding of the circumstances dictating their climate sensitivity.

Here we examine the climate sensitivity of a small cirque glacier (~0.8 km^2) in the northern Rocky Mountains, USA. Rather than analyze historical variations, we investigate the response of an existing glacier to a wide range of potential future warming scenarios. Our purpose is to use this glacier for which we have detailed field measurements to explore the processes dictating the climate sensitivity of small cirque glaciers. We find that under large-magnitude warming the glacier undergoes rapid area and volume reductions that are insensitive to minor variations to the warming rate. Under small-magnitude warming, however, slight differences in the warming rate yield large volume and area differences in the glacier.

A.2 Study Glacier and Glaciological Setting

Sperry Glacier is a small cirque glacier located in Glacier National Park, Montana. The glacier is ~1 km wide, ~1 km long, has an average slope of ~10 degrees, and sits beneath a cirque wall that extends upward 100-300 m (Figure A.1). Historic photographs reveal that since the start of the 20th century Sperry Glacier has lost approximately 78% of its area [*Pederson et al.*, 2006] and has incurred a corresponding (but unquantified) reduction in volume. The climate conditions at Sperry Glacier during this period are undocumented, but during this time period global mean temperatures rose ~0.8 °C [*Hansen et al.*, 2006] and some western Montana records experienced rises in extreme and seasonal average temperatures [*Pederson et al.*, 2010]. Historical trends of retreat of two other glaciers in Glacier National Park imply that projected 21st Century warming could cause them to disappear in the next few decades if those trends were to continue *[Hall and Fagre*, 2003]. However, we can make a zero-order estimate of Sperry Glacier's minimum longevity by applying the recent ablation rate at the terminus (-2 m/yr) to the entire glacier, which we assume to average 35 m deep (this ablation rate and ice depth are justified below). This yields a time constant of ~18 yrs. Considering that this estimate assumes a very high ablation rate with no mass accumulation, it is apparent that the glacier's lifetime will extend substantially beyond 18 yrs.

A.3 Methods

Future changes to mountain glaciers have been investigated with models of differing complexity and computational expense. For example, *Paul et al.* [2007] used a highly simplified approach that combines hypsographic analysis with an accumulation area ratio and neglects the redistribution of mass by ice flow. This approach requires minimal computational resources, and therefore enables large regions (i.e., the Alps) and a wide variety of future scenarios to be explored [e.g., *Paul et al.*, 2007]. *Schneeberger et al.* [2003] used a much more complex approach by coupling an Atmosphere-Ocean General Circulation Model (OA-GCM), a glacier mass-balance model, and a glaciological flow model, which obviously required significant computational power as well as detailed input data for each modeled glacier.

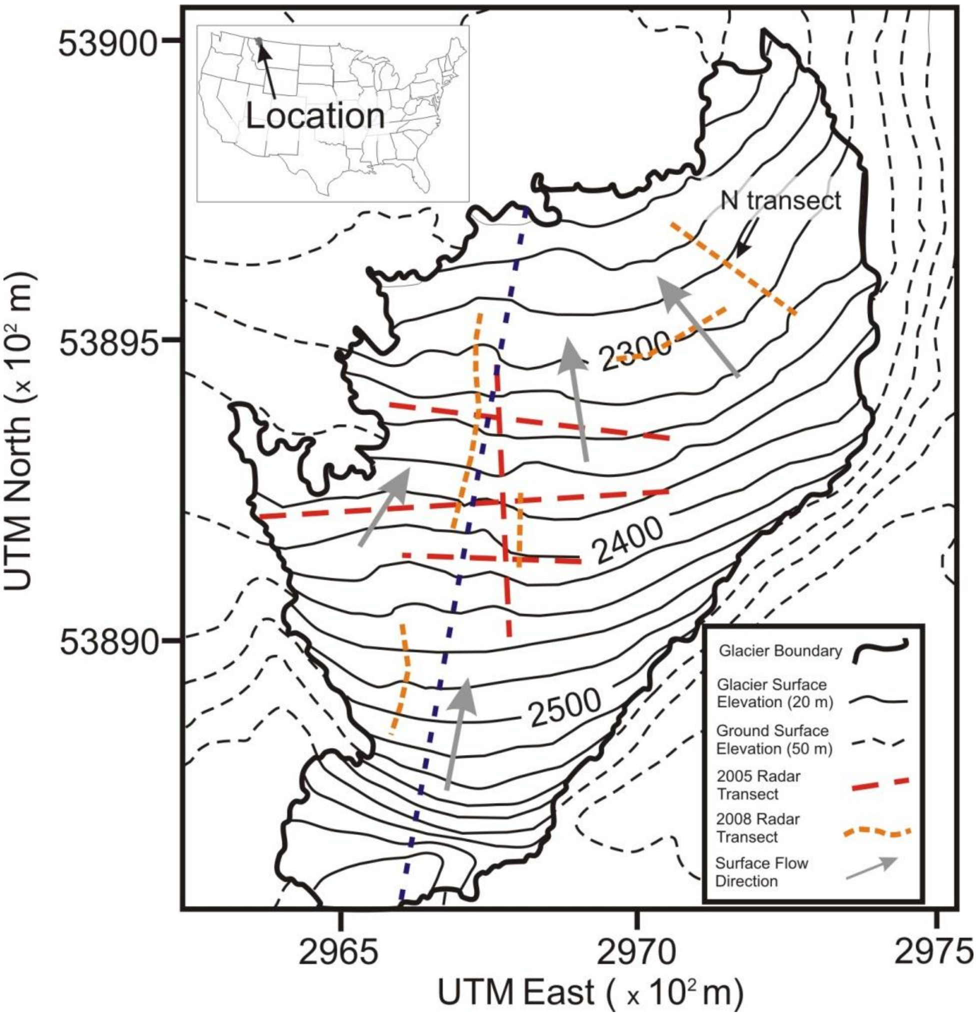

Figure A.1 Topographic map of Sperry Glacier surface derived from GPS measurements. Red dashed lines show location of 5 MHz radar transects collected in 2005, orange dashed curves show location of 5 MHz radar transects collected in 2008. Gray arrows indicate direction of ice flow. The blue dashed line trending roughly North-South is the location of the profiles in Figure 6. The location of radar transect that is shown in Figure A.2 (N transect) is labeled.

Here we use an intermediate level of model complexity to investigate the response of Sperry Glacier to various warming scenarios. We model current and future glacier-climate conditions with a model constrained by field measurements of the glacier's surface mass balance and ice thickness. Our approach addresses 3-dimenstional topography and incorporates vertically integrated ice flow dynamics, but our model is highly simplified and computationally inexpensive. The advantage of this approach is that it allows us to explore many different warming scenarios without neglecting mass transfer. A high degree of uncertainty surrounds future climate change and our aim is not to forecast the future of Sperry Glacier specifically. Rather, our goal is to investigate the range of responses of this small cirque glacier to different degrees of warming and to examine the glacier's sensitivity to different magnitude temperature variations.

A.3.1 Model Construct and Input

To simulate the mass balance and motion of Sperry Glacier, we use a cellular automata (CA) model adapted from *Harper and Humphrey* [2003]. The CA model uses a set of rules to accumulate, ablate, and move units of water equivalent over topographic cells of a landscape. The CA model requires as inputs Digital Elevation Models (DEMs) of the glacier surface and bed, and the annual net mass balance (B_n) defined according to elevation, slope, and aspect. The origin of the mass balance inputs are described in more detail in Section A.3.1.2 (below). An annual time step in the modeling sequence consists of adding the water equivalent of the B_n (positive or negative) to each cell of the DEM. Mass is then transferred between cells via "avalanching" and "ice flow" (described below in Section A.3.1.3). Iterations of mass transfer occur until no cells satisfy flow or avalanche criteria. In other words, the model converges each year when the glacier geometry fully adjusts by mass transfer to the mass gains and losses for that year. After the CA model converges, the surface DEM is updated to account for the small changes in glacier thickness and areal extent. This updated DEM is then used as the initial condition for the next annual time step and the process is repeated.

The model converts surface and bed DEMs from orthogonal to hexagonal cells. This allows for six degrees of freedom for particle motion between adjacent cells. Both avalanching and ice flow criteria are dependent on surface slope, thus each cell has six slope values with associated directions. We compute the slope from the difference in elevation between cells divided by the distance between the centers of the cells. After the surface DEM is updated in surface slopes are recalculated for the subsequent time step.

A.3.1.1 Ice Surface and Bed Topography

We used field measurements to determine the elevation of the current glacier surface, the current glacier volume, and the elevation of the bed surface. We measured the current elevation of the glacier surface in 2008 with GPS data collected with Trimble GeoXH and Trimble R7 receivers. The error of the GPS measurements is less than 1 m in the x and y directions and ~1 m in the vertical direction. We used a Kriging algorithm to generate a 10 m ice surface DEM and combined it with a 10 m terrain DEM (available from the U.S. Geological Survey) to include adjacent bedrock topography.

To measure the glacier thickness, we used a 10 MHz Narod Geophysics type georadar transmitter and oscilloscope receiver. Our data were collected on 5 m spacing along transects and were georeferenced using a hand-held GPS receiver (accurate to 1 – 3 m). In total, we collected nine transects, four in 2005 and five in 2008 (Figure A.1). We identified the two-way traveltime (TWT) of the first reflection of the bed for each trace and converted the TWT to depth assuming a constant radar velocity of 0.168 m/ns (Figure A.2). Based on this propagation velocity, the ¼ wavelength resolution [*Annan*, 2005, p. 380] of the radar is ~4.2 m. We assume that all reflections come from directly below the acquisition point and we used a Kriging gridding algorithm to interpolate the ice depths over the area covered by Sperry Glacier using the edge of the ice surface as zero depth points. The final bed surface topography was generated by subtracting the interpolated ice thickness from the surface DEM. The surface and bed DEMs serve as initial condition inputs for our model runs.

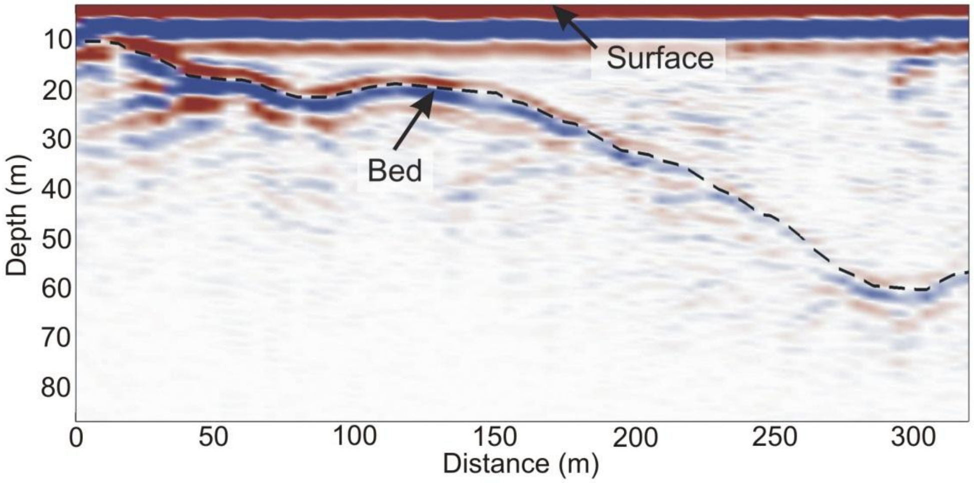

Figure A.2 Radar transect from Sperry Glacier. The bed reflection is clear across the profile. Depths are calculated with an assumed constant velocity of 1.68x108 m/s. The location of the transect (N transect) is shown on Figure A.1.

A.3.1.2 Mass Balance

Our model requires a prescribed function for mass balance versus elevation. Our function is based on two years of field measured surface mass balance and other meteorological and glaciological measurements in the basin [*Reardon and Harper*, unpublished USGS report]. The function consists of two different linear gradients, one for above the ELA and one for below the ELA (Figure A.3). We generated the lower mass balance gradient by linearly fitting field observations of net annual mass balance vs. elevation. The data used to determine the lower elevation mass balance gradient were primarily acquired in the ablation area of the glacier and were spatially averaged across the width of the glacier. We found the mass balance gradient in the lower elevations to be $+7.5\times10^{-3}$ m of water equivalent per 1 m rise in elevation (0.0075 m m^{-1}). A net ice loss of ~2 m water equivalent occurred at the terminus (~2300 m elevation contour) all four years that we measured mass balance. Based on the mass balance gradient upward from the terminus, the ELA should be located at ~2570 m. However, field measurements and late summer photographs (Figure A.4) indicate that the ELA is actually lower, ranging between about ~2420-2550 m (depending on aspect). We attribute this lowered ELA and calculated climatic ELA to avalanching, wind drifting, and lower melt rates due to shading on the upper reaches of the glacier, which are represented by a higher mass balance gradient in the accumulation zone. After avalanching and flow are accounted for, the modeled ELA matches recent observations of the position of the observed ELA.

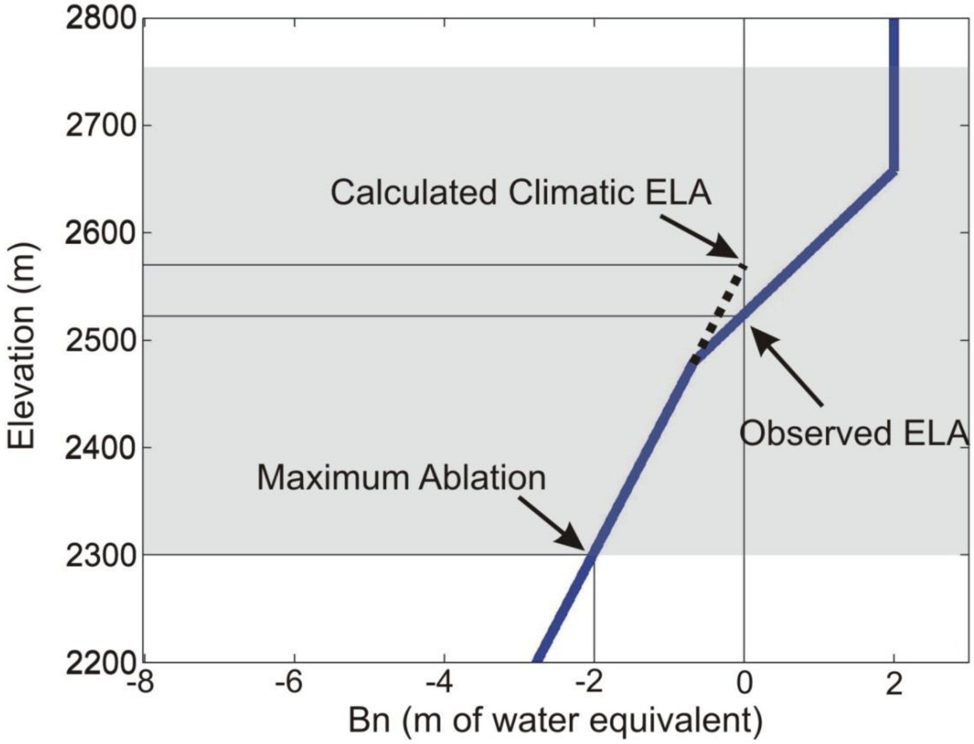

Figure A.3 Mass balance curve used as input for modeling. Elevation range spanned by Sperry Glacier is delineated by the gray shaded area. Locations of the calculated climatic ELA, observed ELA, and maximum ablation elevation are marked

Sperry Glacier occupies a north-facing basin, but the surrounding topography with more southerly aspect and similar elevation range does not support perennial ice. To account for aspect-dependent mass balance, we defined six aspect directions based on the direction of the steepest slope for each cell and allowed positive mass balance only on the three north-most facing aspects. This matches present and historical observations, with ice existing at Sperry Glacier but not on adjacent southerly aspects.

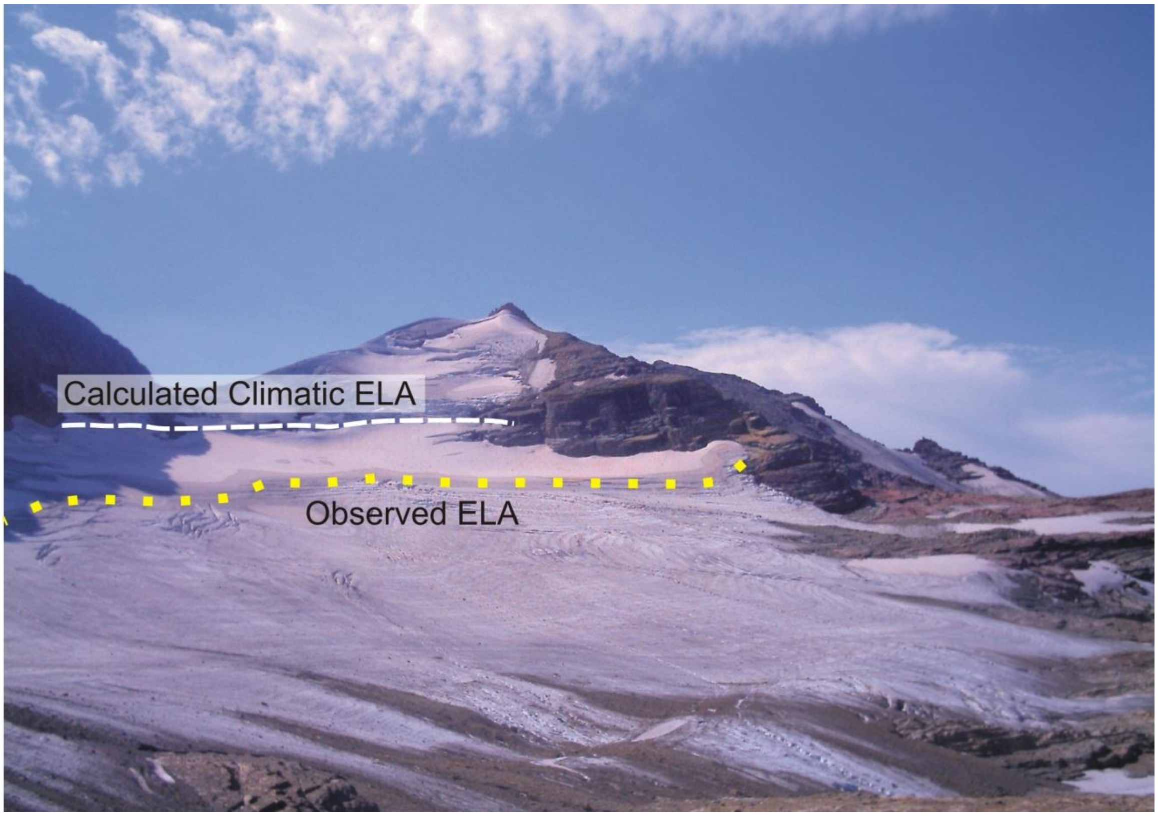

Figure A.4 Photograph of Sperry Glacier taken on 8-31-2007 as part of a time-lapse photo study. The Approximate location of the calculated climatic ELA is marked with a white dashed curve; the observed ELA is marked with a yellow dotted curve. The location of the observed ELA in 2007 was higher than in all other observed years. The region of the glacier that is in view in this photograph is approximately 1 km.

A.3.1.3 Mass Transfer

Ice movement is modeled by assuming that flow will occur when basal shear stress (τ_b) exceeds a critical value of 10^5 Pa [*Nye*, 1951]. Hence, the model utilizes the common simplification that ice deforms as a pure plastic [*Hooke*, 1998; *Paterson*, 2002] and both ice deformation and basal sliding act to keep τ_b just below a yield stress. When τ_b exceeds 10^5 Pa in a cell, enough mass is transferred out of that cell to bring τ_b to just below the yield stress. Basal shear stress is calculated as:

$$\tau_b = \rho_i g h \sin(\theta), \qquad (8)$$

where ρ_i is the density of ice (900 kg m^{-3}), g is the acceleration due to gravity (~9.8 m/s), h is depth of ice, and θ is defined as $tan^{-1}(\Delta Z/\Delta d)$ where ΔZ is the difference between adjacent cell surface elevations and Δd is the distance between the center point of two adjacent cells. After τ_b stabilizes below 10^5 Pa on all cells of the glacier, another year of annual mass balance (negative or positive values) is applied to the surface, slopes and basal shear stresses are recalculated, and mass is again moved by avalanching and ice flow.

The upper portion of Sperry Glacier receives enhanced accumulation due to avalanching from the adjacent cirque wall. This is evident from large avalanche debris piles in this area witnessed every spring. To simulate this avalanching, cells with slopes greater than 30° and ice thickness less than 10 m pass their mass accumulation down-slope with each annual time step. The 10 m ice thickness cutoff is used, allow potential ice falls to form on steep slopes.

A.3.2 Warming Scenarios

We modeled two different climate warming scenarios: 1) No temperature change. The initial mass balance curve (which produces an overall negative mass balance of the glacier) is constant during the 21st century; and 2) Linear warming rates. The temperature increases each year by a constant amount so that a target temperature is achieved 100 years after 2008. This scenario was run for 1-10 °C/century warming rates at 1 °C intervals thereby producing 10 sub-scenarios. The IPCC Fourth Assessment Report projections show global surface temperature likely increasing 1.1–5.4 °C by the year 2100 for future emission scenarios A1B, A2, and B1 with the best estimate for temperature increase of 2.8 °C, 3.4 °C, and 1.8 °C respectively for the three scenarios. Locally, an analysis of downscaled OA-GCM output (Coupled Model Intercomparison Project phase 3) for high elevations in northwest Montana found that under scenario A1B the probability distribution function peaks at 0.28 for an end of century mean temperature increase of 3 °C [*Gillan et al.*, 2010]. The span of the 0.20 probabilities for end of century temperature increases is 0.5 °C to 6.4 °C warming, and the 0.10 probabilities have a range of a -0.5 °C cooling to a 7.1 °C warming. Our suite of scenarios therefore spans a wide range of projections and includes the tails of the probability distribution for most projections. Specifically, the A1B projection of 3 °C by 2100 is bracketed by our 3 °C/century and 4 °C/century warming rate scenarios, which reach +2.76 °C and +3.68 °C in the year 2100, respectively.

Oerlemans [2001] shows that ELA change can be related to change in the mean free-air temperature by:

$$\Delta ELA = -\frac{1}{\gamma}\Delta T_{fa}, \tag{9}$$

where γ is the local temperature lapse rate. We use the theoretical average lapse rate value of γ=0.007 K/m [*Oerlemans*, 2001] because reported local lapse rates [*Finklin*, 1986] are variable and overlap with the theoretical. Using this average value of 0.007 K/m implies that for every degree K increase in T_{fa}, the ELA rises 143 m. We use this relationship to estimate how various changes in T_{fa} will affect the future volume and area of Sperry Glacier. We note that 21st Century climate change in northwest Montana may also involve change in precipitation. Climate models project precipitation change of roughly +/- 5% for northwest Montana, but projections have low confidence and high variance. We therefore do not address precipitation changes in this paper and our results reflect temperature change only in the absence of substantial precipitation change.

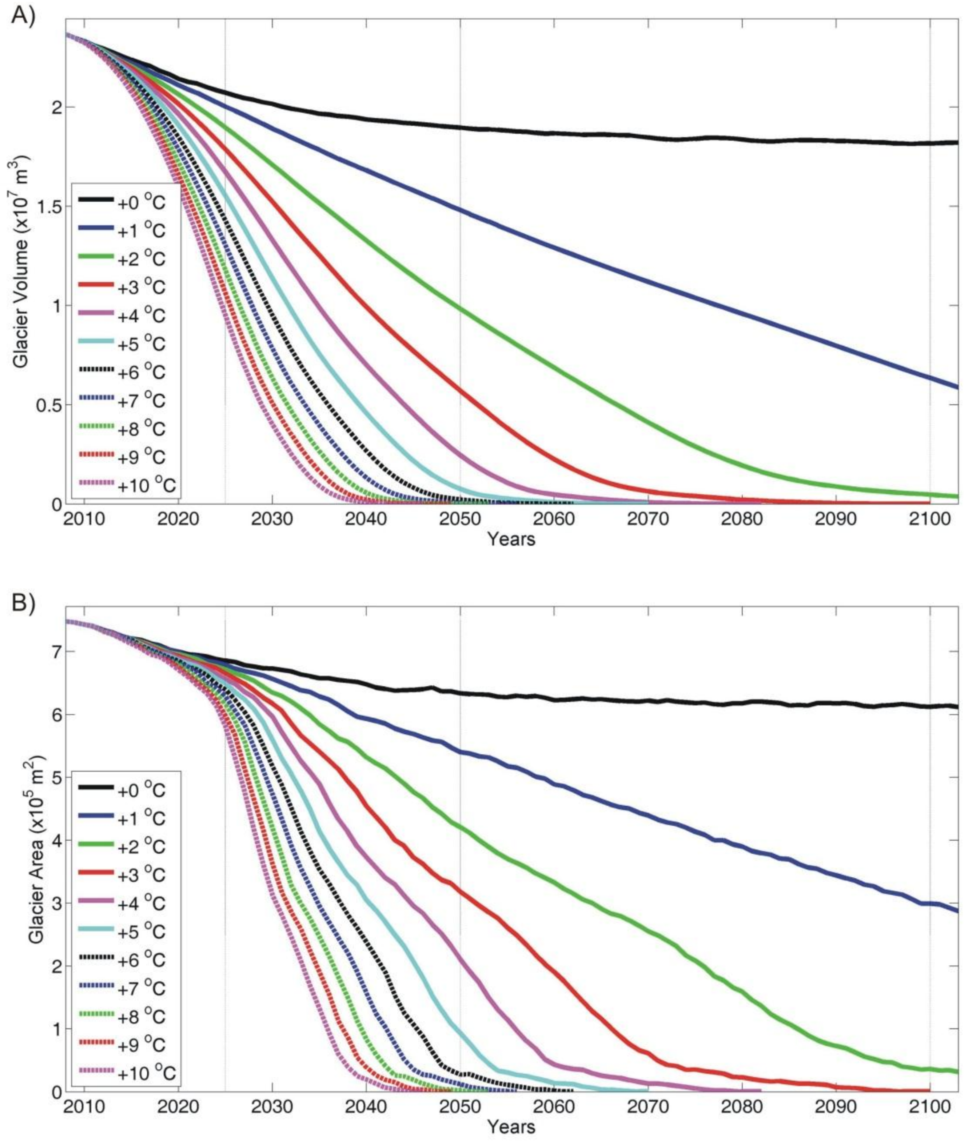

Figure A.5 (A) Total volume vs. time and (B) total area vs. time curves for all model scenarios used in this study. Legend numbers are total degree per century temperature increases. Since modeled temperature increase is simulated by ELA increase (text equation (8)) the baseline 'current' temperature is 0.

Each modeled climate scenario uses the 2008 glacier geometry, ice volume, and mass balance distribution (described in Section 3.1.2) as initial conditions. All model scenarios were run for a 100 yr time period, allowing 2 yrs. for model ramp-up time. We output the geometry, volume, and area of the modeled glacier after each year.

A.4 Results

The ‘no change’ scenario offers perspective on future changes if the recent average annual mass balance distribution, which has been negative, were to continue indefinitely. Our radar and GPS measurements show the current ice volume to be ~2.59 x 10^7 m^3 and the maximum depth to be ~80 m. With no increase in T_{fa}, the modeled glacier shows a decrease in volume of about 26% and a decrease in area of 19% by ~2030, implying that the glacier is not in equilibrium with current climate. The glacier then remains stable to the end of the century (Figure A.5 A & B). A cross-sectional view (Figure A.6A) shows that under these conditions, the Sperry Glacier will retreat ~200 m by 2030. Although the lower elevation portions of the glacier thins and retreats, the upper elevations (above ~2525 m) remain relatively unchanged from the 2008 glacier. The majority of the ice area lost by 2100 is from the lowest elevations where influence from avalanching is minimal or non-existent (Figure A.7B).

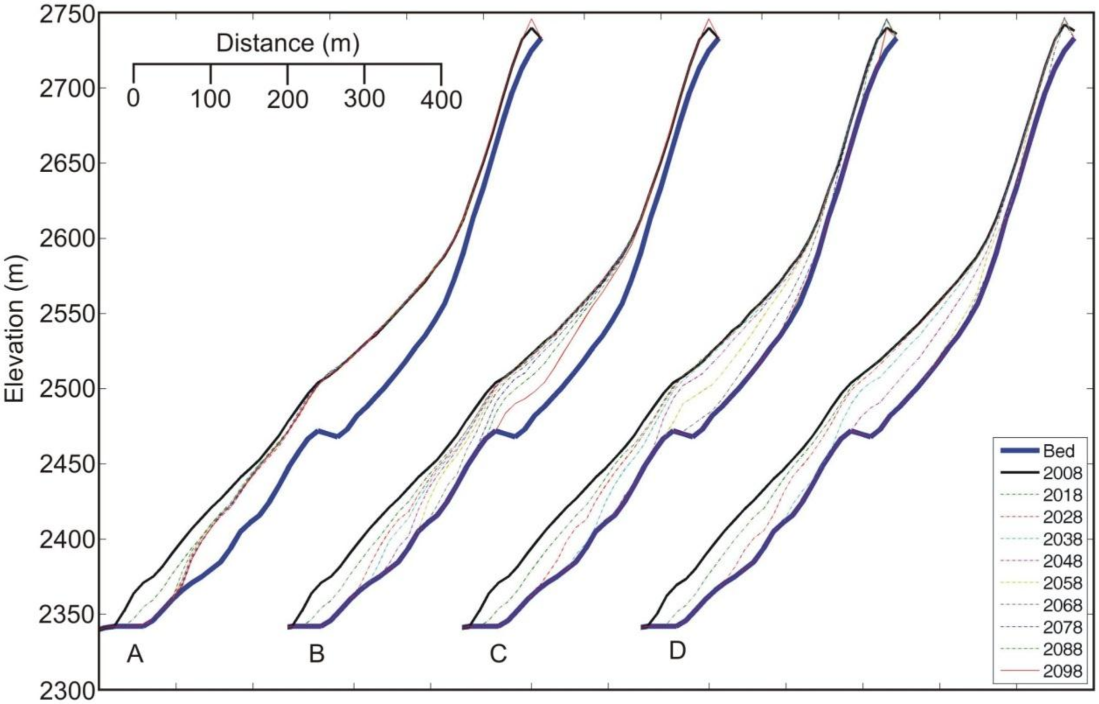

Figure A.6 Elevation profiles for four different modeled scenarios: (A) current Bn, (B) linear increase in temperature of 1 °C per century, (C) linear increase in temperature of 2 °C per century, and (D) linear increase in temperature of 3 °C per century. Each plot shows the bed elevation profile (blue line), the initial (2008) ice surface elevation profile (black line), the ice surface elevation profile in 2098 (red line), and the ice surface elevation profile for every ten years between 2008 and 2098 (dotted lines). The location of the elevation profile on Sperry Glacier is marked on Figure A.1 (blue dotted line). The profiles are vertically exaggerated by 2.

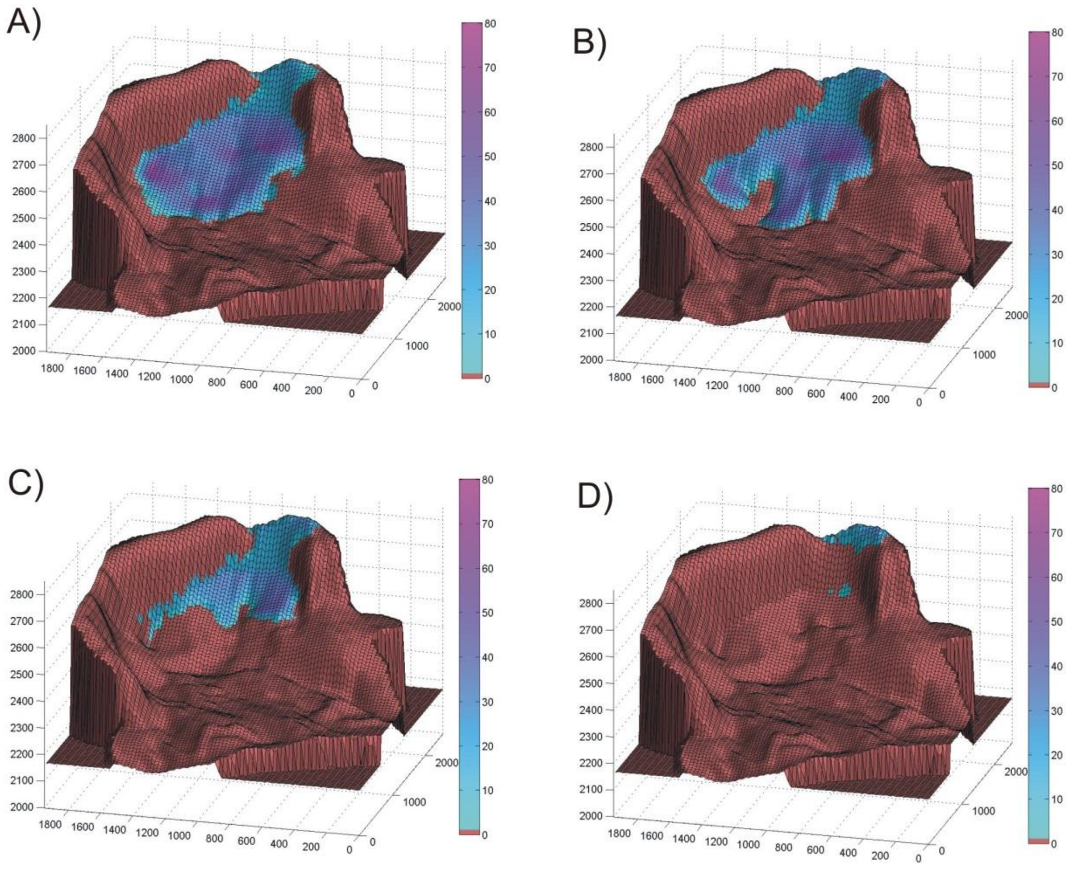

Figure A.7 Model DEM outputs of Sperry Glacier extent and depth including: (A) the interpolated glacier that is the initial condition for all model runs, (B) modeled glacier in the year 2100 under the current Bn scenario, (C) modeled glacier in the year 2100 under the 1 °C per century increase scenario, and (D) modeled glacier in the year 2100 under the 2 °C per century increase scenario. Brown is the current glacier bed (where ablation has occurred) and the surrounding topography, blue to purple is ice depth from 0 m - 80 m, respectively.

With a 1 °C/century warming, the glacier persists in 2100 (Figure A.5A&B) but the area and volume decrease from current values by ~60% and ~75%, respectively. The rate of volume and area reductions are close to linear over the entire modeled time period for the +1 °C/century scenario. Notably, the glacier's rate of area and volume loss tracks the linearly increasing temperature for the entire time span modeled in this scenario, whereas the rate of area and volume loss under warmer scenarios takes 5-10 yr to become linear. With a warming of 2 °C/century, the area decreases 95% and the volume is reduced 97% by 2100. Despite dramatic reductions in glacier area (Figure A.6D), the remaining ice is up to 30 m deep. With a warming rate of 3 °C/century, the area and volume both decrease by 99.9% by 2100 effectively eliminating the glacier. Hence, the 1 °C/century and 2 °C/century warming rate scenarios do not cause the glacier to disappear, while the 3 °C/century warming rate scenario has it disappearing at about 2100. Since the downscaled AO-GCM prediction of the A1B scenario of 3 °C temperature increase by 2100 is bracketed by our 3 °C/century and 4 °C/century warming rate scenarios, our model results conservatively estimate the glacier existing past the year 2080 under the A1B scenario.

All warming rate scenarios above 3 °C/century result in the glacier disappearing prior to 2100. Under these scenarios, volume quickly decreases, while area changes take ~10 years to decrease substantially (Figure A.5). As the glacier nears zero volume and area, rates of change slow again, as the only remaining ice occupies the highest, most sheltered part of the cirque wall. Our model shows that Sperry Glacier disappears by 2050 under a warming rate of 9 °C/century or greater (Table A.1).

A.5 Discussion: Sensitivity to Warming Rate

To quantitatively explore the sensitivity of Sperry Glacier to different warming scenarios, we computed the ice volume difference between consecutive warming scenarios (i.e., +1 °C/century versus +2 °C/century) over time. At any time *t*, the volume difference between two consecutive warming scenarios ($\Lambda(t)$), is calculated as:

$$\Lambda(t)\big|_i = V(t)\big|_{T=i} - V(t)\big|_{T=i+1}, \qquad (10)$$

where $V(t)\big|_{T=i}$ is the volume of Sperry Glacier with a warming rate of *i* °C/century above present temperature (note that *i* represents a temperature rise at a rate of *i*/century so actual temperatures at any time *t* < 100 will be less than i). Hence, Λ(t) depicts how records of ice volume for warming scenarios, which differ by 1 °C/century diverge from each other over time. A peak Λ value (*max* Λ), representing the biggest difference in volume between each 1 °C/century different warming rate, is reached 20 to 100 years in the future (Figure A.8a). The Λ values approach zero as scenario differences either reflect similar glaciers consisting of ice in only the highest elevations of the cirque, or total ablation of the glacier. We did analogous calculations with glacier area.

As expected, larger magnitude increases in warming rate result in larger and earlier reductions in glacier volume and area than do smaller magnitude warming rates. However, our analysis reveals the glacier has variable sensitivity to 1 °C/century differences in warming rate, which dependents on the total magnitude of the warming rate, values of *max* Λ decay exponentially as the total magnitude of the warming rate increases (Figures 8b and 8c). For example, *max* Λ_{volume} at T=1-2 is ~5.8 times greater than the *max* Λ_{volume} at T=8-9 and ~2.75 times greater than *max* Λ_{volume} at T=4-8 . In other words, scenarios differing by 1 °C/century under low-magnitude warming produce very different ice volumes, but scenarios differing by 1 °C/century under high-magnitude warming result in a similar ice volume at any given time. The decay of *max* Λ is proportional to the inverse of the total magnitude of the temperature increase. Empirically, we find that:

$$max\,\Lambda_{Volume}\big|_{(T_i - T_0)} \propto \frac{1}{(T_i - T_0)^{\beta}}, \tag{11}$$

where T_0 is the initial (pre-retreat) free air temperature, T_i is the free-air temperature *i* degrees above T_0, and β is an empirically derived constant that likely represents glacier geometry (i.e., ice depth and hypsometry) and mass balance gradient; for Sperry Glacier β≈1.22 (Figure A.8b, dashed line). The β value is therefore simply a scaling factor used to fit the curvature of the decay function.

Although a decay of *max* Λ with increasing T stems from the fact that a one degree increase in temperature is a smaller percentage increase of higher temperatures, the *max* Λ curve (Figure A.8) requires a scaling factor (β) for direct proportionality to $\frac{1}{(T_i - T_0)}$. Two competing processes dictate the growth of Λ over time and therefore the value of *max* Λ. First, the temperature difference between the two scenarios causes the melt rate of the higher temperature scenario to increase faster than the melt rate of the lower temperature scenario, thus causing Λ to increase over time. The growth rate is not linear, however, because the area of the glacier diminishes over time and there becomes less and less area for melt-rate differences to act on. Second, high elevation accumulation and the resultant mass transfer vary greatly over time between small warming rate scenarios. For example, an area of net accumulation and down-valley ice flow will persist for 73 years longer for a +1 °C/century warming rate than for a +2 °C/century warming rate, and the +2 °C/century warming rate scenario maintains an accumulation area for 25 years longer than a +3 °C/century warming rate scenario. For larger warming rates, however, accumulation and mass transfer processes do not vary significantly between scenarios because the ELA rises above the basin in a short time window (16 years between +6 °C/century and +10 °C/century warming rate scenarios). Thus, since there is very little variation in total accumulation under high-magnitude warming scenarios, these scenarios quickly converge to a similar condition where a nearly stagnate block of ice melts away. In contrast, because there is a large difference in total accumulation between different low magnitude warming scenarios, these scenarios have greater divergence of glacier area and volume adjustments over time.

Because future climate warming will likely have some degree of spatial variability [*Shindell and Faluvegi*, 2009], the glacier response throughout Glacier National Park could reflect this variability, depending upon the magnitude of warming. If warming is severe, we could see little to no regional variability of glacier response with all glaciers undergoing similar reductions in area and volume. However, if warming is slight, then the minor temperature variations between basins could lead to large regional variations in glacier area and volume changes. For Sperry Glacier, the threshold between the two modes of behavior is a warming rate on the order of 4-5 °C/century.

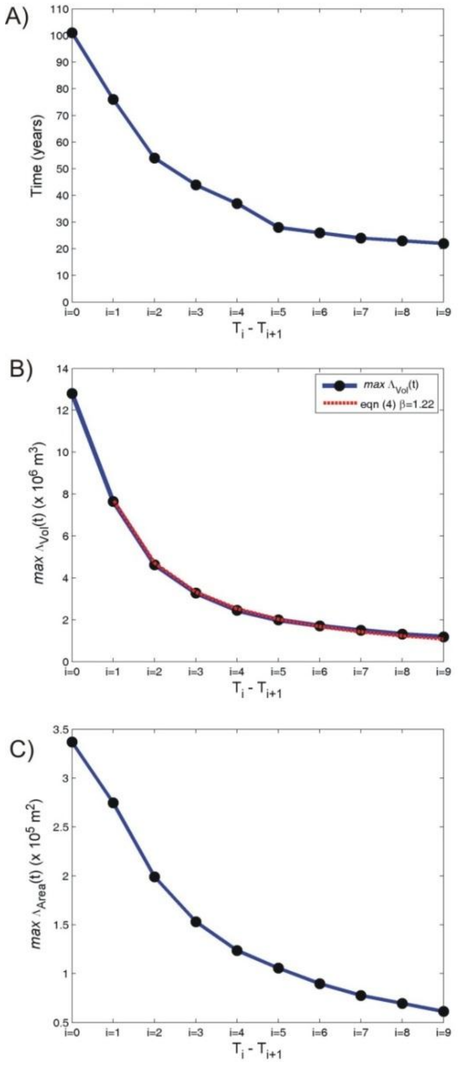

Figure A.8 Maximum value of the difference in ice volume (B) and area (C) between modeled scenarios differing by 1 °C and the time that the maximum volume difference occurs (A). The values of i represent the magnitude of the lower of the two temperature change scenarios being compared. For example, i=1 is the difference between the volume of the 1 °C per century linear temperature increase minus the volume of the 2 °C per century linear temperature increase at time t. Note that the i=0 point is maximum volume difference between a constant temperature model and a linearly increasing model, all other max Λ points show the relationship between 2 increasing temperature scenarios. Values on the x-axis are denoted by the i values (described in the text). The red dotted line in B is the empirical fit to the max ΛVolume values (Equation 11 in the text). Notice that the fit does not relate to the i=0 point because Λ is still increasing at 100 years thus the max Λ value is not representative of the value of the models were run for a much longer period.

A.6 Conclusions

Unless the ELA rises above the highest elevation in the Sperry Glacier basin (~2800 m), there will be net annual accumulation at high elevations and the glacier will never totally disappear. Based on Equation 9, a 2 °C increase in temperature is required to move the ELA to 2856 m elevation. The most probable projection based on downscaled OA-GCM output using the *IPCC* [2007] A1B scenario is ~3 °C warming in Northwest Montana by 2100. Our modeling work suggests that under these conditions the glacier will persist through at least 2080. Even for an extreme warming trajectory of 10 °C/century, the modeled glacier exists for another four decades. These results demonstrate the shortcomings of future projections of glacier change based on extrapolation of historical retreat rates.

Under scenarios of a warming climate, larger summer heat input causes greater ablation rates of cirque glaciers. If this greater ablation rate is not balanced by increased accumulation and mass transfer, cirque glaciers will lose mass. Global mean temperature rise has not been spatially homogenous nor is it expected to be in the future, particularly in mountain regions. Our modeling has shown that area and volume changes of Sperry Glacier are more sensitive to minor variations in temperature under low magnitude warming than high-magnitude warming. This has relevance for interpreting ongoing change and anticipating future change to small glaciers in a spatially heterogeneously warming climate.

Table A.1 Model calculated volume and area of the 11 scenarios included in this study. Each value is given for the years 2025, 2050, and 2100. All model runs assume a starting year of 2008.

		2025		2050		2100	
Scenario	ΔT_{fa} (°C)	Volume (x 10^7 m^3)	Area (x 10^5 m^2)	Volume (x 10^7 m^3)	Area (x 10^5 m^2)	Volume (x 10^7 m^3)	Area (x 10^5 m^2)
Current B_n	0	2.0714	6.854	1.8954	6.335	1.8166	6.121
Linear rise over 100 years	1	2.0009	6.789	1.4799	5.399	0.6352	2.992
	2	1.8961	6.718	0.9832	4.207	0.0474	0.361
	3	1.7863	6.652	0.5700	3.178	0.0000	0.006
	4	1.6718	6.559	0.2453	2.106	0.0000	0.000
	5	1.5528	6.493	0.0754	0.930	0.0000	0.000
	6	1.4254	6.395	0.0224	0.274	0.0000	0.000
	7	1.3012	6.285	0.0051	0.1203	0.0000	0.000
	8	1.1786	6.160	0.0007	0.0219	0.0000	0.000
	9	1.0615	5.979	0.0000	0.000	0.0000	0.000
	10	0.3997	3.129	0.0000	0.000	0.0000	0.000